Effect of Restitution Coefficient on Inertial Particle Separator's Efficiency

A Thesis Presented By

Mehdi Abedi

To

The Department of Mechanical and Industrial Engineering

In partial fulfillment of the requirements

For the degree of

Master of Science

In

Mechanical Engineering

In the field of

Thermofluids Engineering

Northeastern University

Boston, Massachusetts

May 2009

ABSTRACT

Deficiencies of Inertial Particle Separators (IPS) at the inlet of turboshaft engines, operating in harsh environments, have caused significant maintenance costs for the US government and endangered the safety of Operating personnel. In this research, an investigation was conducted to study the sand particle rebound characteristics which are widely used in the design of the Inertial Particle Separators. Experimental and numerical approaches are applied to measure the restitution coefficients. Three different particle accelerator setups were designed to eject high speed small particles and to measure the restitution parameters upon their impact with target surfaces at various conditions. In addition, numerical modeling of fully elastoplastic collision was performed using a commercial finite element software to study the rebound characteristics in detail. Results revealed a strong dependency of normal restitution coefficients on the impact velocity. Also it was found that the tangential restitution coefficients vary vastly with particle size while the impact velocity has no significant effect on tangential restitution coefficients. The results were in complete agreement with previous studies, on functional behavior of restitution coefficients with respect to the incident collision angle. These developed restitution coefficients were integrated into a commercially available computational fluid dynamic software to predict the particle trajectories in a typical IPS model operating in particle-laden environments in accordance with the government standards. The results of IPS efficiency are surprisingly in good agreement with experimental data reported in open literature. Our study further showed that to improve the IPS efficiency, a drastic reduction in normal restitution coefficients is necessary by modifying the IPS' outer shell surface materials. Numerical modeling with reduced normal restitution coefficients demonstrated improvements in the order of 10% in IPS efficiency.

ACKNOWLEDGEMENTS

I wish to express my deep gratitude to my thesis advisor, Professor Mohammad E. Taslim, for his guidance during my research and study at Northeastern University. His understanding, encouraging and personal guidance have provided a good basis for the present thesis. But more than that, it is his personal warmth that has made working with him such a valuable experience for me.

I wish to thank my friends and colleagues, especially Jonathan Doughty and Kevin McCue in Northeastern University. Without their help and support, I wont' be able to make this happen.

This acknowledgement would be incomplete, without thinking of my family, on whose constant encouragement and ever lasting love I have relied throughout my life.

TABLE OF CONTENTS

LIST OF FIGURES

NOMENCLATURE

$F_{Buoyancy}$	Particle Buoyancy Force
d_p	Particle Diameter
g	Acceleration due to Gravity
F_{Drag}	Particle Drag Force
C_{wind}	Wind Speed
C_s	Settling Velocity
f	Friction Coefficient due to viscosity
X, Y	REDLAKE Software's Coordinate System
X', Y''	Computational Coordinates
m_s, m_I, m_R	Slope Direction of Target Plane, Approaching and Rebound Particle
V_{IN}, V_{IT}	Approaching Particle Velocity Vector Components
V_{RN}, V_{RT}	Rebounding Particle Velocity Vector Components
U	Local Flow Field Magnitude Velocity
$u_P\big\|_{rel.}$	Relative Particle Velocity
u_P	Absolute Particle Velocity
P	Compressed Gas Pressure
V	Piston-Cylinder Volume
m	Compressed Gas Mass
R	Gas Constant
T	Gas Temperature
x	One Dimensional Coordinate System
D	Cylinder Diameter
M	Molecular Weight
E	Total Energy
M_p	Piston Mass
$\tilde{M}$	Compressed Gas Mass as a Function of Time
I	Impulse
F	Contact Force
m_p	Particle Mass
U_P	Tangential Component of Particle Velocity
V_P	Normal Component of Particle Velocity
p_t	Tangential Component of Contact Force
p_n	Normal Component of Contact Force
k	Radius of Gyration

Greek

ρ_a	Air Density
ρ_p	Particle Density
μ	Dynamic Viscosity of Air
β	Angle
$\Delta\alpha_I, \Delta\alpha_R$	Distances, Particles Pass Between Two Successive Frames
Δt	Time Interval Between two Consecutive Frames
τ	Impulse Time
ω	Particle Rotational Velocity
μ_s, μ_k	Static and Dynamic Friction Coefficients

CHAPTER 1 INTRODUCTION

1.1 Overview

Turbine engine has found its place as a primary power plant for military aircrafts and ground vehicles. Today's military actions require helicopters and ground vehicles which can operate in severe sand/dust environments. Deserts of Afghanistan and Iraq are good examples of such severe conditions (Figure 1-1).

Figure 1-1: Turbine Engines in Sand/Dust Environment
(Courtesy of RTOAVT Task Group-094 [1])

In early 1960s, when applications of turbine engines in defense systems became common for manufacturers, engine erosion from ingested sand and dust was considered to be insignificant. As a matter of fact, lack of practical ideas in what is "abnormally severe deserts' environment" let designers test the turbine engines in an underestimated condition without catastrophic failure. These test results led to a false sense of security with regard to erosion, and a corresponding lack of interest in providing engine erosion protection. Experiencing severe engine-erosion started in mid-1960s, when the average operating time of the aircrafts' engines operating with the US Army at Fort Benning, Georgia, was reported below 300 hours due to erosion [1]. Tabakoff reported even worse scenario of 50-250 hours for the operating life of helicopter engines operating in sandy areas [2]. Later on, several serious accidents have been reported due to engine failure in these severe conditions. British Airways 747 Boeing powered by four Roll Royce RB211 engines on June24, 1982 is one if these incidents. This flight that also referred to as the Jakarta incident faced a cloud of volcanic ash which blocked the engines and led to flameout of all four engines. Fortunately nobody injured in that flight. A nearly identical incident occurred on December 15, 1989 when KLM Royal Dutch Airlines Flight 867, a B747-400 flight from Amsterdam to Anchorage, Alaska, flew into the plume of the erupting Mount Redoubt, causing all four engines to fail due to compressor stall. Once the flight cleared the ash cloud, the crew was able to restart each engine and then made a safe landing at Anchorage. However, the aircraft was damaged. Meanwhile, substantial damage to helicopter and ground vehicle engines due to erosion was experienced in Vietnam, which again emphasized the concern for engine sand and dust protection [1].

Sands/dust particles in all these cases were the main cause of blades erosion, performance failure, clogging turbine cooling passages and blade attachments by depositing a "glass" coating

on turbine and combustor components, spot corrosions by overheating, blockage of oil system passages, oil seal erosion, filter blockage and failure of pumping elements that can cause internal sump fires (See Figure 1-2).

Figure 1-2: Volcanic ash deposition on turbine vanes
(Courtesy of A. Hamed et al. [3])

Each of these malfunctions can cause a fatal accident for the aircraft's or vehicle's passengers. The general solution to avoid any of these cases to happen is to filter the contaminants of the ingested air and meanwhile improve the erosion resistance of gas turbine engine components. The proposed system should have a continuous low pressure drop in the engine inlet and also have minimum weight and maintenance. The integral separator is also known as an inertial separator or Inlet Particle Separator (IPS) was one of the top listed ideas for this system as particulate air enters the inlet and makes a sharp turn. Due to the inertia of the dust particles, they tend to go into a scavenge duct while the clean air goes into the compressor.

During 1965-1978, several different designs of integral separator were conducted by designers to incorporate the inlet protection system as an integral part of a turboshaft engine. Figure 1-3 shows some of these designs in chorological order. Results of these studies were gathered in

design of T700 engine, manufactured by General Electric (GE). The T700, in response to US Army interest in a next-generation utility helicopter, was initially bench-tested in 1973, passed military qualification in 1976, and went into production in 1978. The T700 became the first engine to be military qualified with a particle separator as an integral part. Both the UH-60 Blackhawk and AH-64 Apache model aircraft are now equipped with the self-protected T700 engine.

The integral swirl type separator installed on T700 engines was taken under 50-hour sand and dust environment test. Results showed the efficiency of 91.7% for coarse sands and 64% for fine sands [1]. With minimal additions to the engine envelope, which is one of the bottlenecks in design of IPS systems, the T700 "inlet particle separator" is so completely integrated with the engine, that it cannot be removed. Furthermore in design of IPS there is no more rotating pump in scavenge section and instead a static system is foreseen to pump the required scavenge flow, in order to minimize the erosions of rotary parts. Also due to lack of complexity and lightness there is no need to remove the IPS for better efficiency of the engine when operating in environments that do not require the extra protection offered by the IPS. Since the design of the T700, the US Army has adopted a policy that all engines must have some type of protection system and it must be removable.

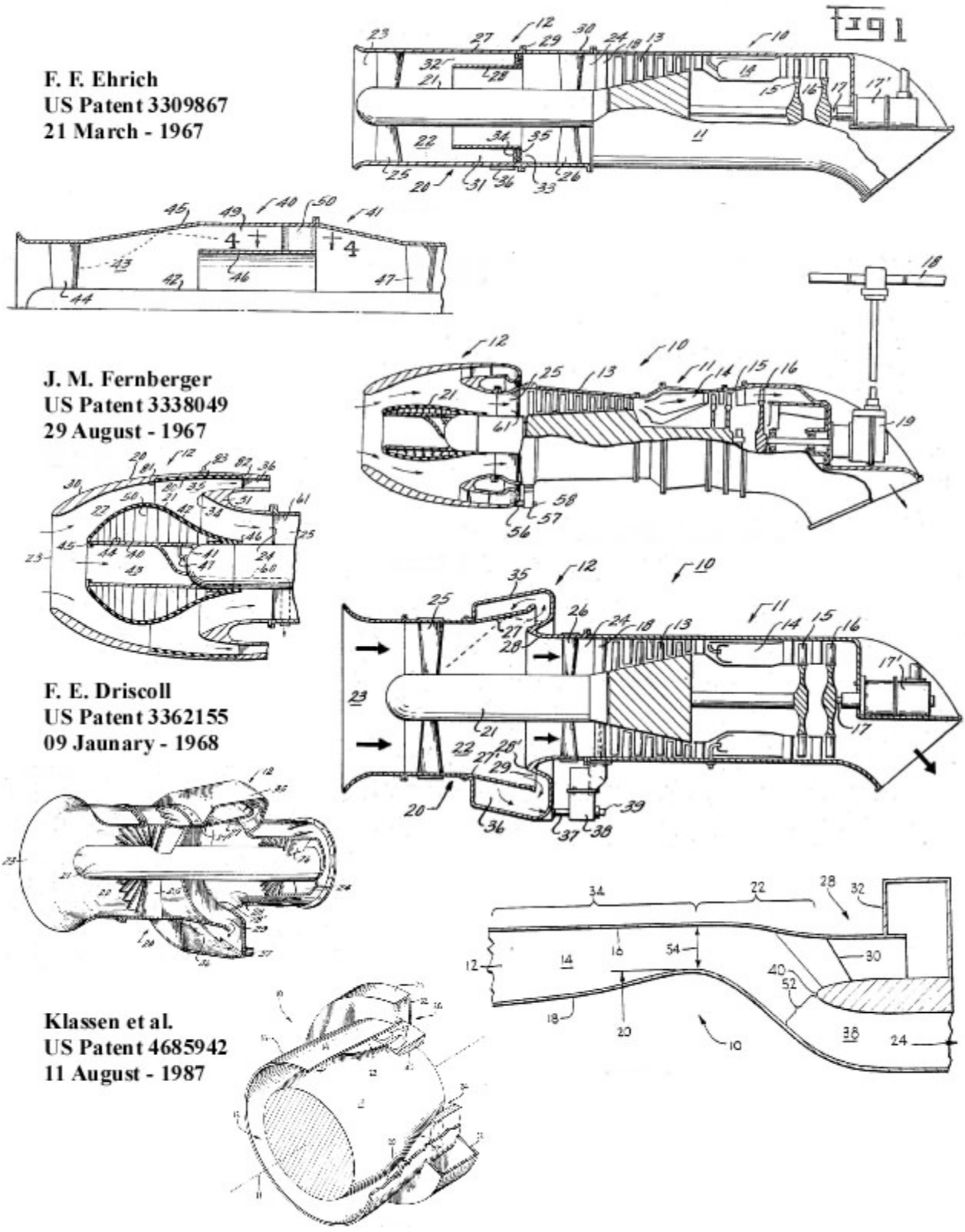

Figure 1-3: History of IPS Development
(Courtesy of United State Patent Office)

Satisfactory of the Inlet Particle Separators operating in normal environment only lasted for an about two decades. With the dawn of new waves of wars in the Middle East which started with the Persian Gulf War (2 August 1990) and extended to Kuwait, Iraq, Saudi Arabia and Afghanistan, Military aircrafts and ground vehicles which use Turbine engines, have been exposed to an excessive/severe amounts of sand-laden air for a long period of time. It is worth to note here that engine exposure time to extreme particulate conditions does not have to be too long to sustain damages. Data analysis of recent military operations in the Middle East states that Sand and Dust can cause severe damages to a gas turbine compressor's blades even in as little as 20-100 hours [3]. Although the filtration of these contaminants are foreseen by using the inlet particle separation systems, but due to different nature of soils in the Middle East and prevalent sand/dust storms in these areas, the fine particles can pass the IPS systems without being captured in the scavenge ducts and cause severe erosions and significant decay of efficiency. In result, unusual amorphous deposits have been observed usually on the leading edges of the first stage turbine vanes [3]. Deposits were quite thick and covered a portion of the airfoil. These depositions accompanying with erosion can change the blades profile and eventually decrease the performance of the engines.

As an example, in Operation Desert Storm, blade erosion was recognized as a major problem, especially on the CH-53E fleet which caused adversely the engine performance decaying. The Naval Air Systems Command Reported a reduction in the time on wing of the T64 from roughly 450 hours to 100 hours*.

Also during the British Saif Sareea II exercise in Oman in 2001, as a test of Britain's rapid reaction capability, with 44 helicopters and 49 fixed-wing aircrafts deploying 22,500 personnel,

* Naval Air System Command News, June, 2006 by Stephanie Vendrasco, "Marines Echo Praise for TiN"

the British National Audit Office (NAO) reported that British helicopters were badly affected by the climate with an average availability rate of 55 percent during the exercise*.

Recently in 2008, the Rolls Royce AE1107C jet engines used in the U.S. Marine Corps new tilt rotor V-22 aircrafts are reported to have less than 400 hours as an average lifetime in Iraq. Overall, V-22 engines should last nearly 500 hours as designed by Rolls Royce†.

These conspicuous lifetime hour decrements, increases engine down time, decreases flight safety and requires significant operating and maintenance costs both for government and manufacturer, specially if their maintenance services contracts are "Power by the Hour" which means, the user pays manufacturer a variable amount for repairs and replacement of the engines, depending on how many hours the engine is used.

Inlet Particle Separator in general can not filter all ranges of particle sizes. A disadvantage of the integral separator systems is the problem with very small particles, (less than 10 μm in diameter) and wall-bounce of larger particles (500 μm in diameter and above). For very small particles, the viscous effects are dominant and the inertia effects can be neglected. In this case particles will follow the stream lines of air flow, which means the separation ratio will be the ratio of the scavenge area to the core area in the splitter lip. Meanwhile, in particle-wall collisions for larger particles, viscous effects are not dominant any more and particle trajectories are mostly determined by rebound characteristics of wall-particle collisions and internal envelope of IPS. In consequence, the efficiency of sand/dust separation is reduced because particles follow the stream lines in the flow.

As an alternative solution, permanent or in-flight movable intake protection screens can also be used to protect the engine intake for the particle-size ranges that can not be covered by IPS

* BNET, Dec, 2002 by Tim Ripley, "Fighting in sand land: operating in the harsh climate of desert regions poses many challenges for military forces. Extreme desert climates and terrain can test both man and machine to the limit"
† Strategy Page, Sep, 2008," Power By The Hour"

systems. The most major disadvantage associated with the use of permanent or in-flight movable intake screens is the danger of ice formation on the mesh and reducing the trust of engines because of pressure losses. To prevent ice formation, a de-icing system can be mounted on the screen, as on the F-117 aircraft, but the latter problem can be a fatal disadvantage for helicopters and their pilots in extreme maneuvers. For this reason, screens are not a favorite choice among the flight crew.

In order to extend the safety of flights, and meanwhile reduction of maintenance costs, lifetime hour of military turbine engines in extreme operational environment especially with high sand/dust concentration should be taken into the account. The rapid incorporation of new and innovative inlet protection system concepts and erosion-resistant coating technologies for engines' components must be pursued simultaneously.

1.2 Research Outline

Several studies have been done for, at least, the last half century to develop a relation between the velocity components of inbounds and rebounds vectors. The commonly used parameters in practice collision phenomena are Restitution Coefficients which relates the inbound to the rebound velocity components.

As mentioned previously, when the number of the wall-particle collisions increase, the IPS systems can not separate the larger contaminants efficiently. Having a realistic design requires knowledge of the exact behavior of collision process in order to predict the correct rebound velocity vectors.

Different methods for the analysis and design of an Inertial Particle Separators, encountering the collision effects, have been used in aircraft industries. Some methods assume the constant restitution coefficient for all different incident velocity vectors of particle [4]. This assumption

has been proved to be wrong as the experiments present a functional behavior of restitution coefficients with respect to the incident collision angle. One of the very prevalent and popular models for the Restitution Coefficients as a function of incident angle is proposed by Tabakoff et al. [5-15] for different particle and target plate materials. Most of the Inertial Particle Separators' designs, in the past two decades, are based on the Tabakoff's empirical relation for Restitution Coefficients [16-21]. This empirical relation is independent of inbound velocity magnitude and particle diameter. However, recent experimental studies present a strong dependency of Restitution Coefficients on these parameters. Taslim et al. [22, 23] showed the over-prediction of IPS efficiency by using the Tabakoff's empirical relation. This research is in continuation of Restitution –Coefficients-effects studies on Inertial Particle Separators efficiency, under the supervision of Prof. M. E. Taslim in Northeastern University.

In order to have a clear view about the Restitution Coefficients, three objectives were defined for this research: (1) to investigate the wall-particle collision characteristics by setting up a new experimental apparatus and compare the results with the other experimental data; (2) to analyze the finite element model of dynamic wall-particle collisions, including the elastic-plastic and frictional effects for different particle sizes, incident velocity vectors and different particle/target plate materials using ABAQUS® software and calibrate the results with the experimental data in order to represent a more accurate restitution coefficient function; (3) to simulate flow field of a typical IPS system by FLUENT® Software and investigate the particle trajectories for different sand grain-size spectra and restitution coefficients.

1.3 Literature Survey

Particle impact with surfaces is one of the major challenges in the field of Mechanical Engineering and has been studied for at least the past half century. The complexity of the

problem arises from different physical phenomena which contribute to this process. Elasticity, plasticity, elastic wave propagation and dissipation, erosion, and surface microstructure dissipations are samples of these items. Semi chaotic nature of the collision due to the surface roughness is adding more difficulty to the problem. medium in which the collision happen is also has a major role in determining the physical parameters of collision [24].

Most of the earliest discussions on wall-particle collision were concentrated in effects of particles on the surfaces, which fall in two categories of erosion and indentation. Almost, in all of these reports kinematics properties of particle after collision have been ignored or discussed only briefly. One of the pioneer studies that mainly focused on kinematics of collision before and after of impact was given by Tabor [25]. He studied the particle restitution ratio as a main parameter in hardness of metals for low velocities impact (up to 20 ft/sec) and concluded that contact pressure of the material can be assumed to be normal to the contact area at any given time of collision. Tabor found that the restitution ratio is not a linearly function of velocity and as the velocity increased the restitution ratio decreased.

Later on, several models have been suggested for wall-particle collision. Most of these models can only predict few aspects of collision. Yet, no comprehensive model is reported that covers all types of collision. Assumptions which are made for simplifying the equations actually eliminate some important material behavior in impact. Normally two different approaches can be found in the reports for modeling the collision.

One approach is, modeling the wall-particle impact by using the algebraic equations, based on rigid body impact theory and impulse equations. Additionally, the energy conservation usually is applied to include the dissipation effects happened in the materials. This approach eliminates requirement of detailed knowledge of the contact forces to analyze the energy loss but, instead,

requires the coefficient ratios to relate the incident and rebound properties. Simplicity of the model makes this approach ideal for analyzing, displaying and interpreting experimental data. Early studies of impulse equations for describing the collision was presented by Matsumoto et al. [26, 27]. They demonstrated a simple model including the wall roughness and local frictional effects by using the rigid body impact theory for both spherical and irregular-shape particles. For low velocities, an adhesive characteristic of microparticles adjacent to the wall is one of the difficulties of theoretical models to predict the restitution ratio. In Particle Dynamics Laboratory of Notre Dame University, Dunn et al. [28-30] presented a new model by introducing the kinetic coefficients of impulse ratio in impact process. The adhesion term was also added to their model and a quadratic relation between restitution ratio and adhesion term found. Sommerfeld et al. [31, 32] extended the Matsumoto's result by adding the surface roughness terms in the equations. They simulated the wall roughness by assuming that the particle collides with a virtual wall which has a randomly-Gaussian distributed inclination with respect to the wall. In the latter report they observed that the restitution ratio is the function of dynamic coefficient of friction. Using the experimental data Sommerfeld et al. observed that the dynamic coefficient of friction took values of greater than unity in the oblique impacts and by increasing the incident angle toward normal impact the dynamic coefficient of friction decreased to the values of around 0.2. With the assumption of neglecting the deformations of either surface in collision process, the classical theory of rigid bodies can be applied to the impacts in very low velocities. Kharaz et al. [33, 34] performed series of experiments of almost elastic materials. They observed that the results closely agreed with the rigid bodies' theory.

The other approach in modeling the wall-particle collision is using the differential equations of planar motion of a sphere in contact with a flat barrier. In this approach, the contact forces are

taken into account and deformation of materials are also considered. Complexity of the model and solving several nonlinear differential equations only for one particle is the rigorousness of this approach. On the other hand, more accurate physical prediction can be performed as more realistic conditions are contributed in the model. Early attempts of these types dates back to the report of Hutchings et al. [35]. To find the depth of crater, they developed a simple numerical model of the oblique impact of a rigid sphere against a plastically-deformable surface. Contact forces in this model were limited to the normal contact force and friction force tangent to the contact area. Later, he reported that under normal incidence angle of impact and at very early stages of contact, the contact elastic wave pressure can be somewhat higher than the plastic indentation pressure [36]. This high pressure is only applied in a very small fraction of contact time. He concluded that this pressure has no significant effects on the dynamics of the impacting particle. A conspicuous discrepancy observed between the Hutchings et al. theoretical results and experimental data. Later, Rickerby et al. and Hutchings et al. [37, 38] enhanced the model with more accurate method of contact area measurements. The results were in good agreement with experiments except for the very low velocity and normal impaction where elastic forces became important. Sriram et al. [39] suggested that incorporating the elastic energy stored in the material and the rotational energy stored in the particle can improve the data agreement with experimental results. On the other hand, when the particle is softer than the target plate, the material behavior is reported to be different. Timothy et al. [40, 41] observed that the mean dynamic contact pressure was up to 50% higher than the quasi-static pressure. They conclude that elastic-plastic waves had a major role in dynamics of collision. Tsai et al. [42] argued that adhesion effects as breaking of contact surfaces, bulk plastic deformation and plastically-deformed asperities are also important. Their model was in good agreement with experimental data in low velocities

(less than 20m/s) but at very high velocities the discrepancies are more than 10%. For impaction with particles softer than the target surface, the main contact stresses are compressive, tensile and shear stress. Dunn et al. [29, 43] used the rigid body assumption of target surface to develop the differential equations of motion during the collision process for very low velocities. Recently Kim et al. [44] reported a new model for elastoplastic impact with the contribution of the adhesion forces. They assumed that the particle had a rigid behavior, so the shape of the particle would not change during the collision. Their results agreed closely with the experimental data in low velocities (less than ~20m/s) but by increasing the approach velocity results deviated from the experiments as the rigidity assumption of particle were not valid anymore.

As for the geometrical aspects, almost in all of the theoretical models, one of the collision elements is assumed to retain its original shape during the impact. Yet, no report has been presented the simulation of elastoplastic deformation of particle and surfaces in wall-particle collision. Recently with the advent of powerful computational hardware and software, numerical modeling of wall-particle collision using the finite element approach becomes prevalent [45, 46]. This research which is the subject of CHAPTER 5, deals with the numerical on the numerical simulation of the elastoplastic collision to develop a general relation between the restitution ratios and particle/surface materials, approach velocities and incidence angle of approach for each of particle-size categories.

For a reliable model to predict the kinematics of collision, experimental data are also required. Quite a number of experimental studies have been performed in order to demonstrate the wall-particle impact model for different materials and particle sizes. Several different experimental apparatus were reported to accelerate the particles and different types of methods demonstrated for measuring the kinematics of particle before and after the collision. Partridge et al. [47]

studied the crater depth as a function of shooting particle speed. The particles were accelerated to a speed of ~0.5 km/sec, by firing them with a special 0.220-caliber smooth-bore gun. Hussein et al. [48] were the first to investigate the rebounding characteristics of particles using high-speed photography. Later, Grant et al. [5] enhanced the method of Hussein et al. to accelerate the particles by controlled vertical duct air flow (Wind tunnel). High speed photography was used to trace the quartz-sand particles (200 μm diameter) path during the collision. They reported the mean particle velocity of 450m/sec in the wind tunnel. For smaller particles of less than ~50 μm in diameter, high speed photography is not useful any more. Tabakoff et al. changed the measurement rig to laser-doppler velocimeter (LDV) system. The optical components of the LDV were arranged to measure two simultaneous components of a single fly ash particle (~15 μm diameter). For particles of larger than ~ 2mm in diameter and with very low approach velocities, viscous driven method naturally replaced by free fall setups [49, 50]. Kharaz et al. [33, 34] used the free fall setup to measure the restitution ratios of aluminum oxide spheres (5 mm diameter) impacting a thick soda-lime glass plate at 3.9 m/sec. High speed photography with stroboscope light is reported as the measurement setup. The results were considerably better in precision than the previously published works and were taken in several reports as a benchmark for validating the theoretical models. Pendulum machine is reported to present precise data for studying glancing impacts [51]. This system includes a rotating or stationary target surfaces which a pendulum hitting it at different velocities. A number of experimental studies reported to use this method for measuring the restitution coefficient of wall-particles in liquids [52, 53]. Sommerfeld et al. [31, 32] performed a series of particle tracking velocimetry in particle-laden horizontal channel flow with low approach velocities (~ 10 m/sec). For the visualization, a pulsed laser light sheet was produced to capture the location of particles by image analysis

method. For very fine microparticles (less than 50 μm diameter) and low velocities, thermofrosis, buoyancy and Brownian forces on a microparticle are almost inevitable. To avoid affects of these forces on restitution ratio, Dunn et al. [29, 30, 43] developed an experimental setup in vacuumed conditions (~10^{-4} torr). Depending on the electrostatic characteristics of the particles, microspheres were dispensed using either an electrostatic particle dispenser or a neutral particle dispenser. In either case the particle accelerated by gravity and at very low approach velocities. For higher velocities (above ~40 m/sec) one of the methods to accelerate the particles is using the compressed-gas gun, equipped with a sabot as a particle carrier during acceleration and muzzle to capture the sabot and release the particle or particles. Oka et al. [54] studied the effects of sand blasting particles on the target surfaces by using this method. The compressed-gas gun setup accompanying with high speed image capturing setup have been used in this study too. Some slight changes and enhancement were done to eliminate particle deviation from straight path and initial rotation. More details will be discussed in CHAPTER 5. Recently, Leconte et al. [55] presented a new setup to measure the restitution ratios more accurately using a vibrating and a stationary wall at both ends of a cylinder. It can be proved that bouncing of a single ball at the limit is a periodic one dimensional problem. The approach and rebound velocities can be accurately described by measuring the time intervals between two periodic impacts. The observed results in very low velocities, closely matched with Hertz theory of impact.

Quite a number of experimental studies on restitution coefficient have been performed for different particle materials, size, approach-velocity vector and target materials. Tabor [25] probably was the first one who did some experiments on measuring the hardness of materials, using the wall-particle collision in low velocities. He concluded that restitution coefficient is a function of approach velocity. Later, Dahneke [56-58] presented some of the earliest normal-

impact experimental results. He measured the polystyrene latex (PSL) particles velocities, before and after collision, by particle beam technique. The theoretical results had a noticeable deviation from experimental data. He described this discrepancy to the elastically deformed contact area which increased the contact surface energy. In contrast with Tabor's results [25], Hussein et al. [48] reported that approach particle velocity is an invariant parameter in prediction of restitution ratio. In all these efforts, the erosion of materials was the goal in the studies, and restitution ratios were the side product of those studies. The first report to thoroughly investigate the kinematics of impacted particles was presented by Grant et al. [5] for study of quartz-sand particle (200 μm diameter) impact with 2024 Aluminum alloy as target plate at University of Cincinnati. A number of experimental studies were reported under the supervision of Prof. Tabakoff for measuring the restitution ratios of quartz-sand particles (165~200 μm diameter) and fly ashes (~15 μm diameter) impacted on different target materials with different approach velocities. Consistently, before the 80's, they reported the same restitution ratios [6-8]. In contrast with Hussein et al.'s conclusion, they pointed out that the restitution ratio is not invariant to the magnitude of approach velocities, as had been assumed by previous investigators. Some observations were reported on linear dependency of tangential restitution ratio with normal component of the impact velocities [8]. Wakeman et al. [10] reported different empirical relations for restitution coefficients of quartz-sand particle (200 μm diameter) impact with 2024 Aluminum alloy as target plate, with approach velocities varying from 215 ft/sec to 539 ft/sec. They concluded that particle rebound characteristics are not affected significantly by target material or temperature for the materials tested. Later, Tabakoff et al. [15] confirmed this conclusion. But, the restitution ratios presented in the new report were absolutely different in behavior from the previous empirical equations. The experiments were performed at a constant

impinging particle velocity of 300 ft/sec rather than in a velocity interval. On the other hand, for very fine microparticles of fly ashes (~15 μm diameter), Tabakoff et al. [11-14] observed that restitution coefficients were highly dependent of the target materials.

Wall-particle impact applications are not limited to the turbomachinery systems. Space and clean environments, pneumatic conveying, fluidized beds, particle separation in cyclones, classification of particles and mixing systems are examples of these applications. Quite a number of studies have been done to measure the restitution ratios in these fields. Several measurements of individual normal and oblique impacts of steel particles (~50 μm diameter) and Ag-coated glass particles (~8.6 μm diameter) on different target surfaces reported by Dunn et al. [29, 30, 43, 44]. For low velocity collisions, they observed that the effects of adhesive forces played a major role in kinematics of impact. Surprisingly, for velocities less than ~5 m/sec, the restitution curves diverged to the zero value instead of unity. Summerfeld et al. [32] presented a series of experimental data, for glass particles (100&500 μm diameter) and non-spherical quartz particles (~100 μm diameter) for velocities larger than adhesive critical velocity to attribute the effect of wall roughness on restitution ratios. This report presents a finite element model of wall-particle impact, calibrated with experimental data to measure the restitution coefficients of quartz-sand particles on aluminum alloy surface.

CHAPTER 2 SAND PARTICLES

2.1 Overview

Designing the Inlet Particle Systems requires the knowledge of particles, commonly sand particles, which are ingested by the inlet of turbine engines. Sand in nature is the composition of finely divided rock and mineral particles, which generally can be found in areas where erosion and corrosion of rocks and soils are in the highest level. Additionally, sand particles can be found in the rivers bed and in coastal areas, where the water stream is the main factor of rock erosion and corrosion. Each area in which the turbine engine is supposed to operate has very unique type of soil. Soil in geological term means, the naturally occurring, unconsolidated or loose covering on the Earth's surface. Soil is made up of broken rock particles that have been altered by chemical and environmental conditions, affected by processes such as weathering or erosion, and organic constituents. As a mixture, soil particles pack loosely, forming a soil structure filled with pore spaces that can contain liquids and gases. During the recent wars in the Middle East, the problem of ingested sand/dust particles by vehicles and aircrafts was prevalent. With all diversity in soil and sand constituent, there are some common constituents which usually can be found in all samples.

In the common belief, sand is a tiny and shiny grain of quartz. As a term in geology, sand is in the category of soil grains, which fall in the predefined particle size range. In this classification, type of grain materials in not concluded. Table 2-1 presents different grain size distribution standards in geology and engineering.

ASTM	Boulders	Cobbles	Gravel	Sand			Silt	Clay	Colloids
				Coarse	Medium	Fine			
Grain size (mm)	300	75	4.75	2.0	0.425	0.075	0.005	0.001	

ASSHTO	Boulders	Gravel	Sand		Silt	Clay	Colloids
			Coarse	Fine			
Grain size (mm)	75	2.0	0.425	0.075	0.005	0.001	

USCS	Boulders	Cobbles	Gravel		Sand			Fines (Silt, Clay)
			Coarse	Fine	Coarse	Medium	Fine	
Grain size (mm)	300	75	4.75	2.0	0.425	0.075		

M.I.T.	Boulders	Cobbles	Gravel			Sand			Silt			Clay
			Coarse	Medium	Fine	Coarse	Medium	Fine	Coarse	Medium	Fine	
Grain size (mm)	200	60	20	6	2.0	0.6	0.2	0.06	0.02	0.006	0.002	

Table 2-1: Grain size ranges according to different soil classification systems.

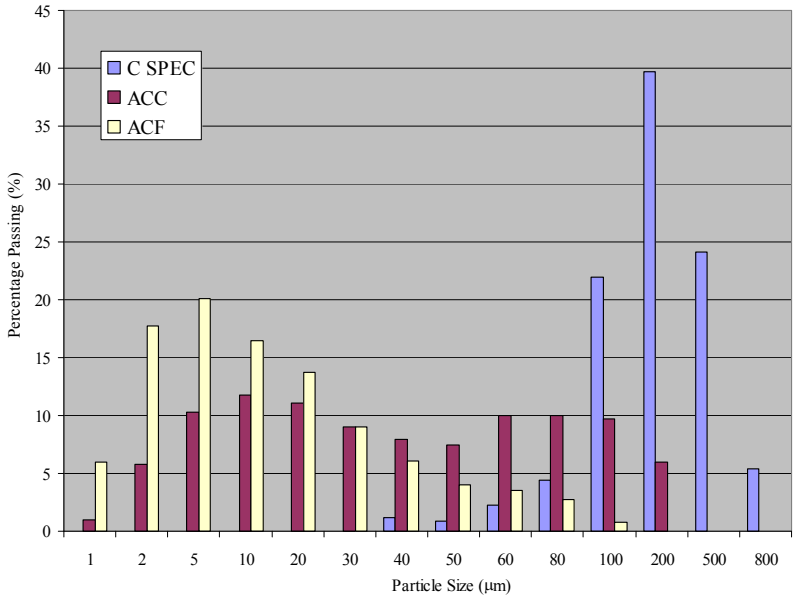

Figure 2-1: Size-Particle Distribution according to Different Standards

An individual particle which falls in this category is termed a sand grain. The next smaller size class (less than ~0.075 mm diameter) in geology is silt, which by comparison feels like flour. For designing the IPS systems other classifications of size-particle are required by military (Figure 2-1).

Depending on the location of sand formation, the constituent may be different. Silica (SiO2) is the most abundant mineral on the continental crust. As a late-stage crystallization product in mature magmas, α-quartz is common in granites, granodiorites, rhyolites, pegmatite, phyllites, mica schist, migmatites and quartzite [59]. quartz is the common name for stable silica polymorphs which can be α-quartz or β-quartz. Usually β -quartz forms in the layer with higher pressure and temperature. It can be concluded that, the most common constituent of sand in inland continental and non-tropical onshore areas, is α-quartz. The bright white sands found in tropical and subtropical coastal settings are eroded limestone and may contain coral and shell fragments in addition. Eastes [60] reported the presence of calcite and gypsum in samples of San Bernardino Co. in California and Las Cruces in New Mexico.

2.2 Mechanisms of Sand/Dust Rising in the Air

As mentioned before, soil particles pack loosely and with large enough applied forces they will follow three different mechanisms of motion (Figure 2-2). Wind flow near the soil surface applied shear stress on the surface. With appropriate wind speed this shear stress can overcome the frictional forces between particles and the soil pavement, which causes the particle to roll and slide on the ground. Usually this applied to all sizes of particles and called “Creep” mechanism.

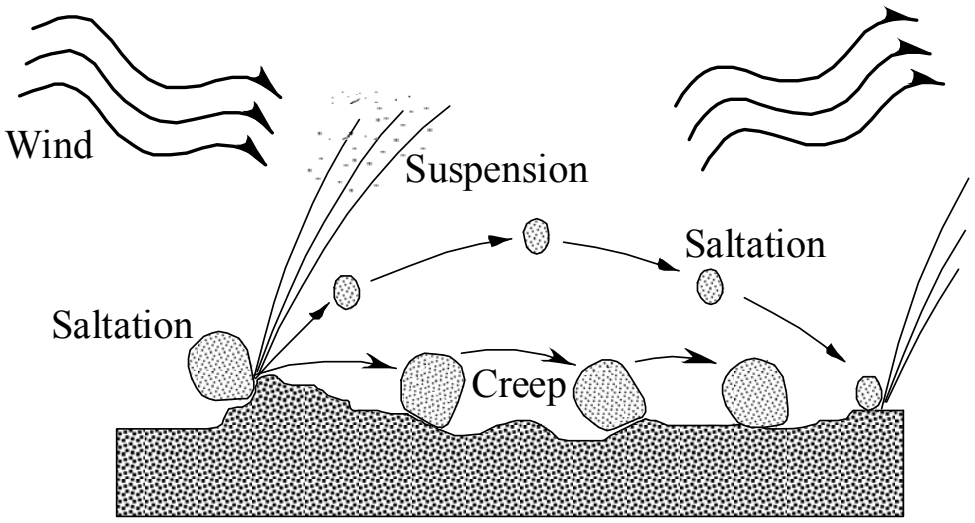

Figure 2-2: Movement Mechanism of Sediments

When Creeping happens, depending on wind speed particles slide or role till hit other particles or an obstacle. During these collisions, smaller particles bounce into the air, drifted approximately four times farther downwind than the height they attain above ground and because of not having enough speed they return back to the ground and repeat these bounces till they settle down. In geology, this mechanism called "Saltation". During the creeping and saltation process, finer particles bounce to the air, and with enough wind speed (Settling Velocity) they can be floated in the wind, which called "Suspension". The suspended particles can be drifted thousands of miles away downwind or by turbulent eddies and updraft they can be lifted thousands of meters upward. When ever the wind stops or near the obstacles which wind speed locally drops, these suspended particles settle down. With stronger winds and storms even the larger particles which usually creep can be suspended and drifted into the air.

One criterion is required to determine the ability of bouncing particle to suspend in the air. Physically, suspension means the equilibrium of applied forces on the particle. For suspended

sand particles, these forces are gravitational and drag forces. The gravitational forces (also called: “Buoyancy” Forces) can be derived from Archimedes' principle:

$$F_{Buoyancy} = \frac{\pi d_p^3}{6}(\rho_p - \rho_a)g \tag{2-1}$$

For microparticles in the air, the Reynolds number $\mathrm{Re} = \frac{d_p U}{\nu}$ is much less than unity. In this case the stokes flow assumption will be valid and drag force can be derived from the Stokes law,

$$F_{Drag} = fC_{wind} = (3\pi\mu d_p)C_{wind} \tag{2-2}$$

In suspension, these two forces are equal so we can combine the two equations (2-1) and (2-2) to calculate the settling velocity.

$$C_s = \frac{\rho_p g d_p^2}{18\mu}\left[1 - \frac{\rho_a}{\rho_p}\right] \tag{2-3}$$

Figure 2-3 shows the settling velocities of sand particles versus different particle sizes (Equation 2-3).

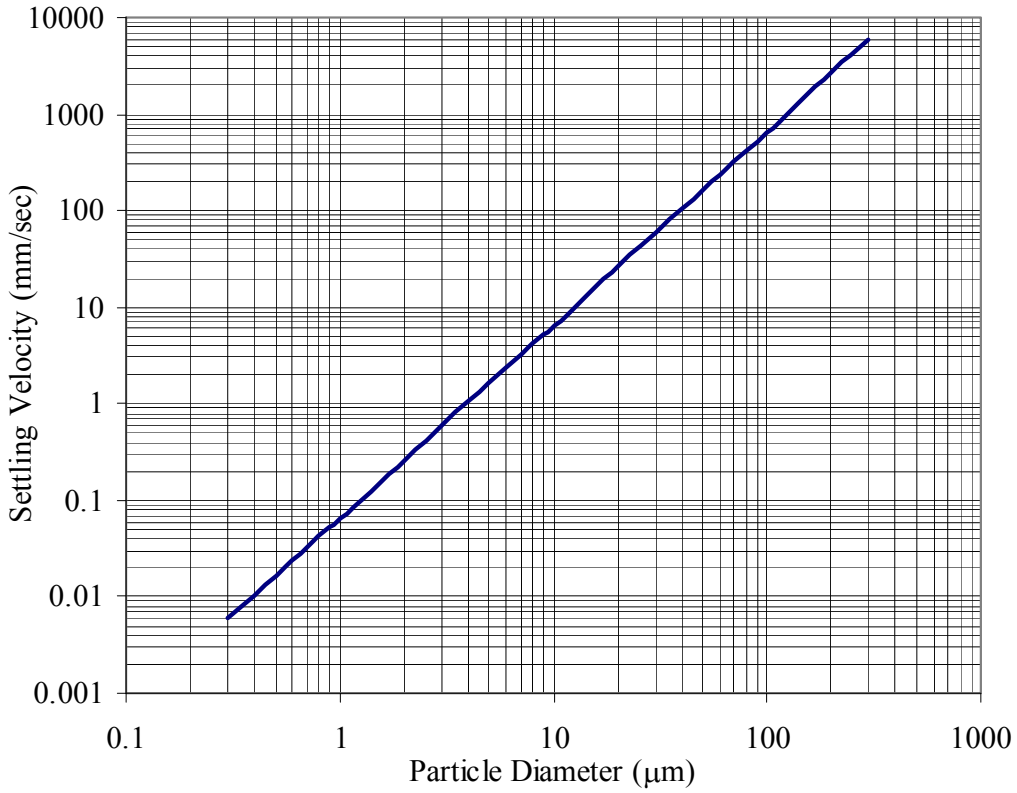

Figure 2-3: Sand Particle Settling Velocities in Air

According to Figure 2-3 and Table 2-1, clay and silt particles with diameter less than 50 μm only require having the velocity about 100 mm/sec (0.36 km/hr) to travel. Comparing with Beaufort Scales (Table A.1) even with a very small air movement they can continue their suspension and settle very slowly. Fine clay particles (~2 μm diameters and less) settle so slowly that they may be transported across oceans without settling. For sand-size particles (~75-1000 μm diameters) the settling velocity is about 5 m/sec (54 km/hr). In scale of Beaufort this wind speed can shake the whole tree and walking will be inconvenience. It can be concluded that in regions rich in clay and silt, probability of dust storm is more than probability of occurring the sand storm. For helicopters and military vehicles, two extreme mission cases of dust storm and sandy soils should be taken into the account. For the latter case, the air speed near the helicopter during landing is so high that raises all types of sands and sometimes even gravels. Also for ground

vehicles, moving in sandy soils, soil particles bounce from ground because of wheels and tracks and shape a dusty cloud around the vehicle. In either case these suspended particles will be ingested by the turbine engines and will damage the internal rotary part of the systems in contact with particles.

2.3 Grain-Size Analysis of the Middle East

Recent military operations in the Middle East which concentrated in Kuwait, Afghanistan, Iraq and Saudi Arabia Kingdom, raised the problem of inefficiency of Inlet Particle Separators. As can be concluded from Figure 2-4, the sand/dust storm is almost prevalent all over the year.

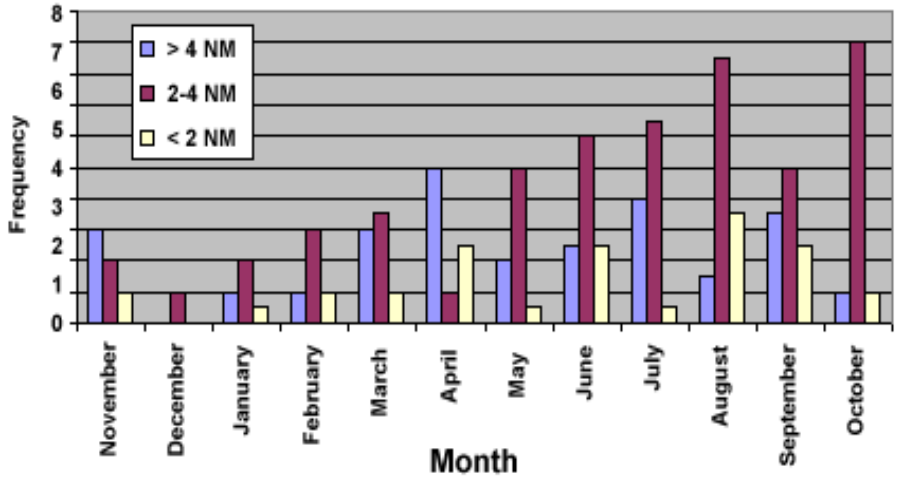

Figure 2-4: Monthly Frequency of Dust Storm in Iraq and Kuwait
(NM: Nautical Miles)
(Courtesy of National Center for Atmospheric Research (NCAR))

The IPS systems that supposed to operate in such conditions are normally designed to separate a range of particle size according to MIL E-5007C (C Spec.) military standards (Figure 2-1). As can be seen in Figure 2-1, the C Spec. only covers the particle size varying between 40 μm to 800 μm in diameters. A number of studies have been performed to present the particle size

spectra in different areas of the Middle East. Abolkhair [61] reported the fine sand grains (0.20-0.3 mm diameter) in the Oasis of al-Hasa, Eastern Province of Saudi Arabia. In Saudi Arabia also Eases [60] reported the fine and medium sand (~0.075-0.25 μm diameter)in their samplings.

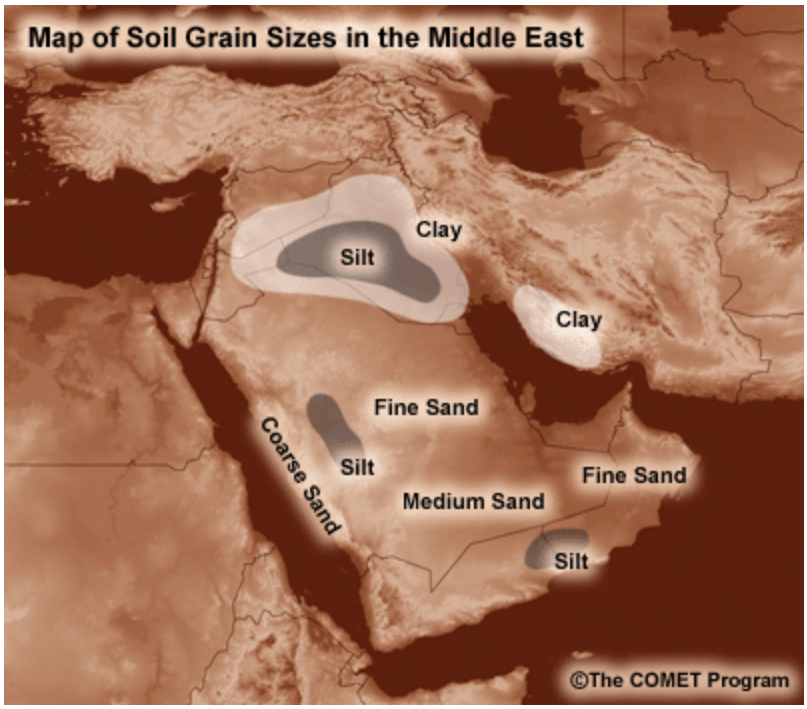

Figure 2-5: Map of Soil Grain Sizes in the Middle East
(Courtesy of National Center for Atmospheric Research (NCAR))

Alsharhan et al. [62]reported the diameters of ~180-800 μm as the grain-size analysis of coastal area in United Arab Emirates. The report was consistent with other measurements as the sea water acts as a detergent agent in the coastal area and washes all fine particles. The remainder is the composition of larger particles on shores. Figure 2-5 demonstrates a map of soil grain sizes in the Middle East. Most of Iraqi's soil is covered with silt and clays (~50 μm diameter and less) with tendency to suspension. More accurate sources of dust are marked in Figure 2-6. The dominant wind direction in Iraq is from north-west to south-east which covers all these areas and is the reason of prevalent sand/dust storm in the area. Abdulla et al. [63] presented a measurement studies on particle-size distribution of Iraqi's sand and dust storms during high

peak of storms in the months of April, August and October. Surprisingly the whole samples were finer than 100 μm (silt category) in diameter and about 50% of the samples were finer than 10 μm (clay category).

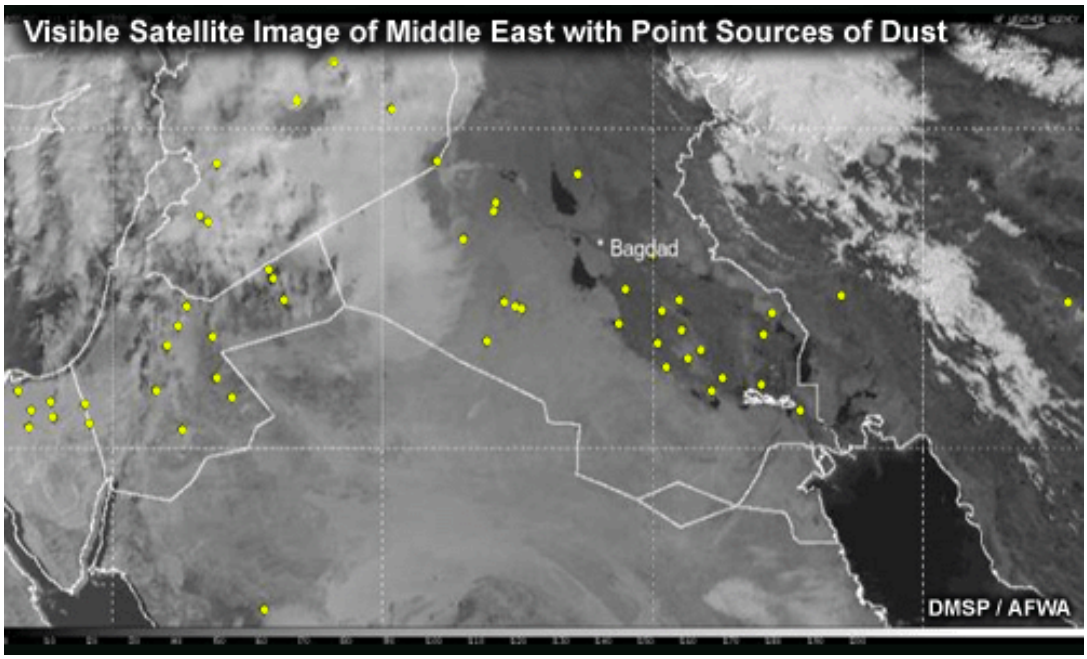

Figure 2-6: Map of Point Sources of Dust in Middle East
(Courtesy of National Center for Atmospheric Research (NCAR))

These data, provided that the particle-size distributions required by MIL E-5007C (C Spec.) can not cover all the particle-size ranges of the real-operative cases. For more realistic design, the AFC distribution which covers sand and silt categories together would be more practical.

CHAPTER 3 THE WALL-PARTICLE IMPACT EVENT

3.1 Overview

Study of wall-particle impact, requires knowledge of surfaces behavior in contact action and geometrical effects on local elastic or inelastic deformation properties. While *Classical Mechanics* deals only with bulk material properties and deformation, *Contact Mechanics* deals with bulk properties that take the surface and geometrical constraints in to the account. The complexity of contact phenomena is stemmed from these nonlinear parameters. There are many approaches that, for the sake of simplicity, have eliminated the detailed interaction of surfaces and variation of forces in collision. From Newton's law, the total momentum of all colliding particles follows the law of conservation of momentum. As was mentioned before, for simplicity, one can deal with impulse instead of individual interacting forces. Dealing with impulses does not require a detailed knowledge of the forces to analyze the energy loss in impact as the total momentum transfer from one object to another is equal to the impulse value. The simplest theory of impact, known as Stereomechanics, uses the impulse-momentum law for prediction of the rebound velocity and kinetic energy loss in impact between particles. It is noteworthy here to explain that, the particle-wall impact is the extension of particle-particle collision with the assumption of highly large enough radius for one of the particles. Using coefficients such as the coefficient of restitution and the impulse ratio offers a rigor and simplicity that makes the model ideal for analyzing, displaying and interpreting experimental data. Yet, reaching these coefficients required the modeling of transient stresses, collisional forces, impact duration and collisional deformation of colliding objects. Geometrical effects on local elastic deformation

properties have been extensively considered by "Hertzian Theory of Elastic Deformation"[64] for perfectly elastic collision. Numerous studies have been reported on modeling of plastic collision of particles with surfaces but in all cases the particle or the wall assumed to be rigid [28, 35, 37, 40-42, 65].

3.2 Macrodynamics of Collision

Based on Newton's law, the inbound and rebound directional vectors of wall-particle collision lay on the plane normal to the wall surface. Planarity of collision mechanics is only valid if the rotation velocity of the particle has no component on the plane of collision. Figure 3-1 is a schematic body diagram of a wall-particle impact.

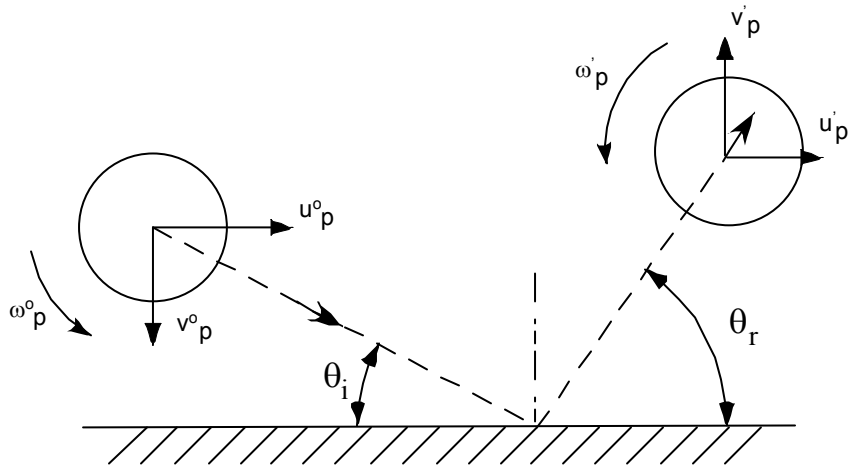

Figure 3-1 Free body diagram of a sphere collides with the surface of a flat immovable barrier

Matsumoto et al. [26, 27] reported an extensive solution for the rigid body spherical particle bouncing on rough walls based on impulse-momentum concept. Later, several studies were reported on extension of this model for fully elasto-plastic impact [28, 31].

In what follows, for the rigid body impact mechanics, the impulse of forces are being used instead of direct study of the contact forces.

$$I(\tau) = \int_0^{\tau} F(\tau) d\tau \qquad (3\text{-}1)$$

For system of Figure 3-1, the only external forces are gravity and contact forces. Neglecting the gravitational force, the Newton's second law for this system can be written as

$$m_p V_p(\tau) - m_p V_p^o = p_n(\tau) \quad \text{(Normal)} \qquad (3\text{-}2)$$

$$m_p U_p(\tau) - m_p U_p^o = p_t(\tau) \quad \text{(Tangential)} \qquad (3\text{-}3)$$

$$mk^2\omega(\tau) - mk^2\omega_p^o = -rp_t(\tau) \quad \text{(Rotational)} \qquad (3\text{-}4)$$

Taking the integral over time, the time average of momentum equations (Impulse) will have the shape of,

$$m_p(\overline{V}_p - V_p^o) = \overline{p}_n \quad \text{(Normal)} \qquad (3\text{-}5)$$

$$m_p(\overline{U}_p - U_p^o) = \overline{p}_t \quad \text{(Tangential)} \qquad (3\text{-}6)$$

$$m_p k^2(\overline{\omega} - \omega_p^0) = r\overline{p}_t \quad \text{(Rotational)} \qquad (3\text{-}7)$$

where, bar indicates a time-averaged variable.

For a sphere, the gyration radius $k = \frac{1}{10} d_p{}^2$ so, Equation3-7, can be rewritten as:

$$m_p(\frac{1}{10} d_p{}^2)(\overline{\omega} - \omega_p^0) = \frac{1}{2} d_p \overline{p}_t \quad \text{(Rotational)} \qquad (3\text{-}8)$$

During the collision, the particle may or may not slide on the wall surface. The sliding depends on the value of tangential velocity at the contact point. The relative velocity of contact point with respect to the particle centroid can be calculated by rigid body motion mechanics as

$$V_r = -\overline{V}_p \qquad (3\text{-}9)$$

$$U_r = \overline{U}_p + \frac{1}{2} d_p \overline{\omega}_p \qquad (3\text{-}10)$$

Then using the Equations 3-5 through 3-8,

$$V_r = V_r^o - \frac{R}{m_p} \tag{3-11}$$

$$U_r = U_r^o + \frac{7}{2}\frac{F}{m_p} \tag{3-12}$$

Assuming that the x-component of the impulsive force is exerted only because of friction, then two possibilities may be considered for the colliding particle

Slip Condition ($U_r \neq 0$):
$$\frac{dF}{dR} = -\varepsilon_o \mu \tag{3-13}$$

Nonslip Condition ($U_r = 0$):
$$\left|\frac{dF}{dR}\right| \leq \mu_s \tag{3-14}$$

Where, $\varepsilon_o = SIGN(U_r) = \pm 1$.

The general solution of the above equations for final particle kinematic properties after collision were given by Matsumoto et al. [26, 27]:

Slip Condition ($U_r \neq 0$):
$$U_p^{'} = U_p^o + \varepsilon_o \mu_k (1 + e_n) V_p^o \tag{3-15}$$

If:
$$\left|\frac{V_p^o}{U_p^o + \frac{1}{2} d_p \omega_p^o}\right| < \frac{2}{7(1+e_n)\mu_k}$$

$$V_p^{'} = -e_n V_p^o \tag{3-16}$$

$$\omega_p^{'} = \omega_p^o + \frac{5}{d_p} \varepsilon_o \mu_k (1 + e_n) V_p^o \tag{3-17}$$

And,

No-Slip Condition ($U_r = 0$):
$$U_p^{'} = \frac{5}{7} U_p^o - \frac{1}{7} d_p \omega_p^o \tag{3-18}$$

If:
$$\left|\frac{V_p^o}{U_p^o + \frac{1}{2} d_p \omega_p^o}\right| \geq \frac{2}{7(1+e_n)\mu_k}$$

$$V_p^{'} = -e_n V_p^o \tag{3-19}$$

$$\omega_p^{'} = \frac{2}{7}\omega_p^o + \frac{10}{7}\frac{U_p^o}{d_p} \tag{3-20}$$

According to Equations 3-17 through 3-20, particle rotational velocity in rebound always get the nonzero values except for the normal impact cases with the initial zero rotation velocities. Brach

et al. [28] extended this model by study of the impulse ratio μ_o as the criteria to change the mode of motion from sliding to rolling.

$$\mu_o = \frac{2}{7}\frac{U_p^o - r\omega_p^o}{V_p^o(1+e_n)} \tag{3-21}$$

3.3 Contact Surface Effects

In general, the contact forces are not limited to the frictional and bulk elasto-plastic deformation discussed in previous section. Molecular force potential (London-Van der Waals forces), electrical forces and surface roughness (asperity) forces, are also the major source of energy loss during the impact. For small particles, the "London-Van der Waals" adhesion forces between molecules of particle and the wall become dominant and below some critical velocities the colliding particle would be trapped by the wall surface. For example 70μm particle has the critical velocity of ~0.5 m/sec [44] below which the normal restitution coefficient drop drastically to zero.

The Van der Waals forces fall in the category of nonreactive-weak intermolecular forces. On the other hand, the electrical forces are more effective even in distances far from the source. Even if particles are not forcefully charged before impact, according to Derjaguin et al. [66] the contact electrification can also happen in collision interval in which particles obtain some electrical charges. The contact electrification not only absorbs a share of particle kinetic energy for separation of electrical charges, but also demands extra kinetic energy to overcome the electrical adhesion forces.

In many reports, the wall surfaces are assumed to be perfectly smooth. However, from a submicroscopic point of view, the surfaces are usually rough enough for micro-particles and

smaller sizes that the local normal vector is deviated from the macroscopic normal vector of wall surface. These deviations are a source of error in prediction of restitution coefficients. Sommerfeld et al. [32] reported an extensive study on behavior of restitution coefficients due to the surface finish. These surface roughness asperities can be visualized as sacrificed supports for colliding particles which can be easily deformed plastically because of stress concentration in their sharp tips. Experiments [67] suggested that surface roughness is very important in determining the restitution coefficient especially before bulk yielding occurs. Tsi et al. [42] suggested to model these asperities with uniformly distributed hemispheres.

CHAPTER 4 EXPERIMENTAL APPARATUS

4.1 Overview

Methodology and apparatus used to measure the parameters of wall-particle impact are described in this chapter. The precise measurement of collision's kinematic parameters before and after impact including velocities and incident/rebound angles were the impetus of apparatus design in this research. Four different setups have been designed and used for the oblique collision studies in the following chronical order: Direct Compressed Air Shooting (Capstone Project), Viscouse Driven Accelerator and Indirect Compressed Air Shooting system (Preliminary and Final Design). Operational problems and lack of accuracy in measurements using an existing setup demanded the next new design. The most noticeable deviations and enhancements from the first apparatus were in particle ejection methods. In general, a setup for the study of particle impact parameters can be divided into two subsets of wall-particle impact setup and measurement apparatus. The former is a particle accelerator which accelerates the particle to a predefined speed and a structure to hold the target plate as the anvil. The latter is the measuring system which measures particle incident and rebound angles as well as velocity vectors before and after collision. The whole system can be housed in a safe shell at atmospheric pressure or in a vacuum chamber to avoid any experimental error due to the air flow and other disturbances. Quite a number of measurement techniques have been reported by the investigators. The most common methods are high speed photography and laser doppler anemometry. In this report, the experiments have been done in a confined see-through chamber in lieu of vacuum and the high speed photography technique used for particle-trajectory tracking.

During the ejection of the high speed particle from the accelerator muzzle, different infrared (IR) photogates track the particle trajectory at certain locations. when the particle crosses the IR beam a trigger signal is sent to the oscilloscope to capture the triggering signal and send the save command signal to the camera to save the images on a computer (See Figure 4-1).

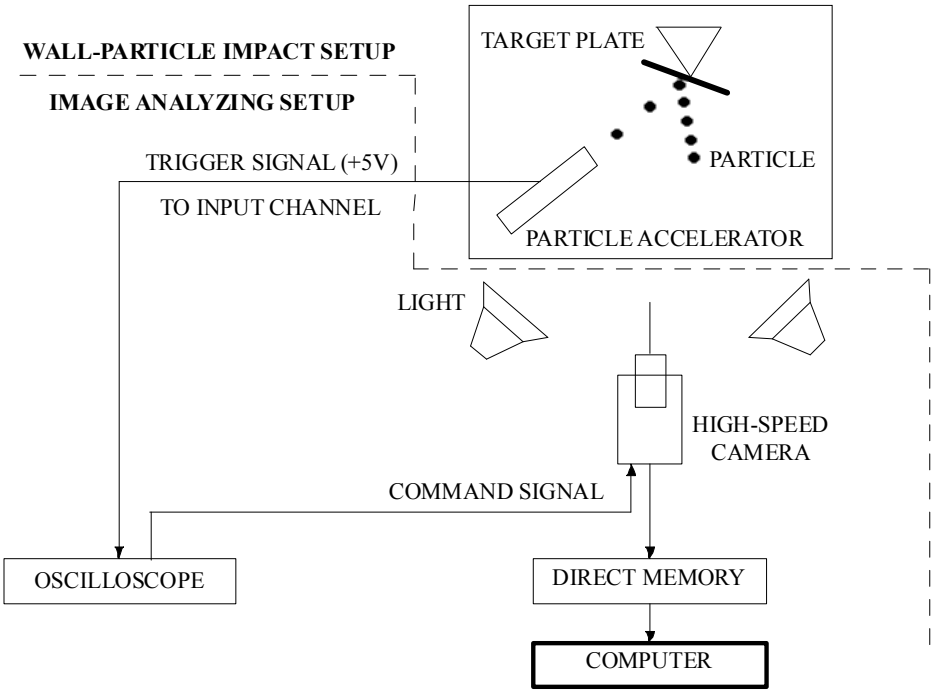

Figure 4-1: Apparatus Schematic Diagram

The postprocessing of the images is done with special high-speed camera software on the computer. Except for the triggering method and photography technique, the measurement apparatus has not been changed during the renovation of wall-impact setup. Discussion of relevant experimental components follows.

4.2 Triggering the Camera

For tracking the particle trajectory the high speed photography method has been used in this research. The particle speed for this study varied between ~10-90 m/sec. In this range, the

fraction of time required for particle to travel a distance of (for example 10 mm) is in the order of hundreds of a microsecond and the collision-process time is in the order of ten microseconds [40, 41]. By a rough estimation, at least four frames are required to calculate the inbound and rebound velocity vectors of collision, which totally take approximately 100 microseconds. In photography standards, an apparatus is required that is capable of taking ~4000 images per second in order to fulfill the whole idea. Normal frame rate for commercial video cameras varies between 18-30 frames per second (fps). For this range, the elapsed time between two successive images varies between 34-56 milliseconds, which let the particle drift a distance approximately 0.3-5 meter.

Figure 4-2: High speed digital imaging camera

The high speed digital imaging system of MotionScope® PCI from REDLAKE Company has been used to capture the particle trajectory with the recording frame rate range between 60-8000 fps and shutter rate of 1X-20X (See Figure 4-2). The camera uses the Rotary Sequenced Image Memory features in the Direct Memory panel for temporary storage of data. at maximum, 8000 fps camera can store 16000 frames in a period of 2 milliseconds. Reaching the last segment of

memory after 2 milliseconds, the hardware starts to overwrite the new data from the first sector of memory (See Figure 4-3).

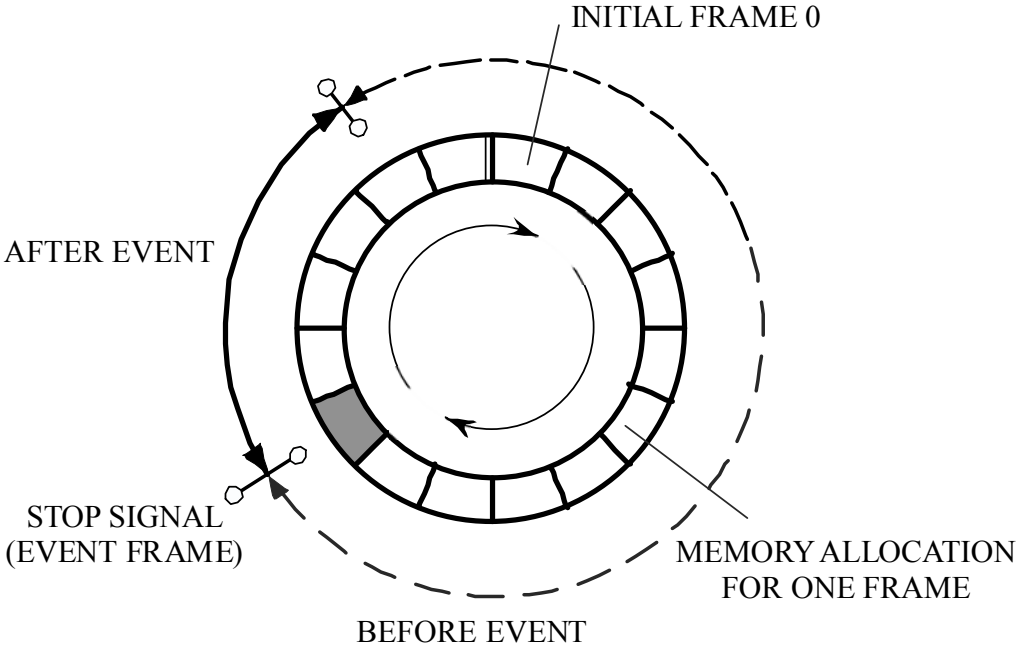

Figure 4-3: The Rotary Sequenced Image Memory Structure

Whenever the camera receives a Stop signal, the Direct Memory Panel starts to save the images before and after receiving the command, with the ratio defined in the camera software on the computer. Stop signal is sent from the Tektronix TDS 5104 Digital Phosphor oscilloscope as the main control system. At the single triggering mode the oscilloscope depicts variations of input triggering voltages from the photogates. Right after that, the triggering-voltage passes the threshold and the oscilloscope sends a Stop signal to the Direct Memory Panel to store the' data. This signal should be sent exactly when particle crosses the photogates beams at predefined locations. By cutting the IR beams, the photogates circuits increase the output voltage above the predefined threshold which terminates sending the Stop command by the oscilloscope. The lag time in these circuits should be at the minimum level in order to have better accuracies and control, which required special IR detectors with Output Rise/Fall Time in order of nanoseconds.

For the first three setups, the educational Vernier photogates have been used. Comparing the beam cross-section area of photogates, particle diameter, and the dimensions of photogates, the adjustment of beam location in order to be crossed by the particles was almost impossible. In the final design an electrical circuit was designed to be compatible with the geometry of the whole system and completely reliable on tracking the particles (See Figure 4-4).

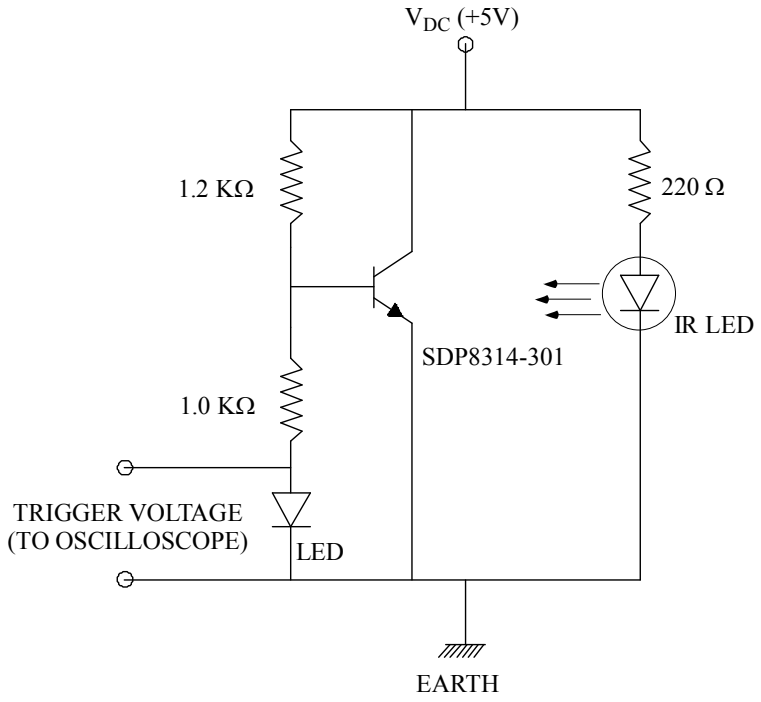

Figure 4-4: Photogate circuit diagram

For the IR detector, which fulfills the requirements of fast response and short Output Rise/Fall Time, the Honeywell's SDP 8314-301 Optoschmitt Detector was chosen. The complete datasheet of Optoschmitt detector can be found in Table B.1. Three photogates were used in the apparatus. Instead of tracking particle to send the triggering voltage, one photogate was located on the accelerator barrel to check the position of sabot as a reliable mechanical movement to be tracked. For contingency, another two photogates were mounted on the muzzle with a resin

mount to measure the particle velocity and compare that with the REDLAKE software result (See Figure 4-5).

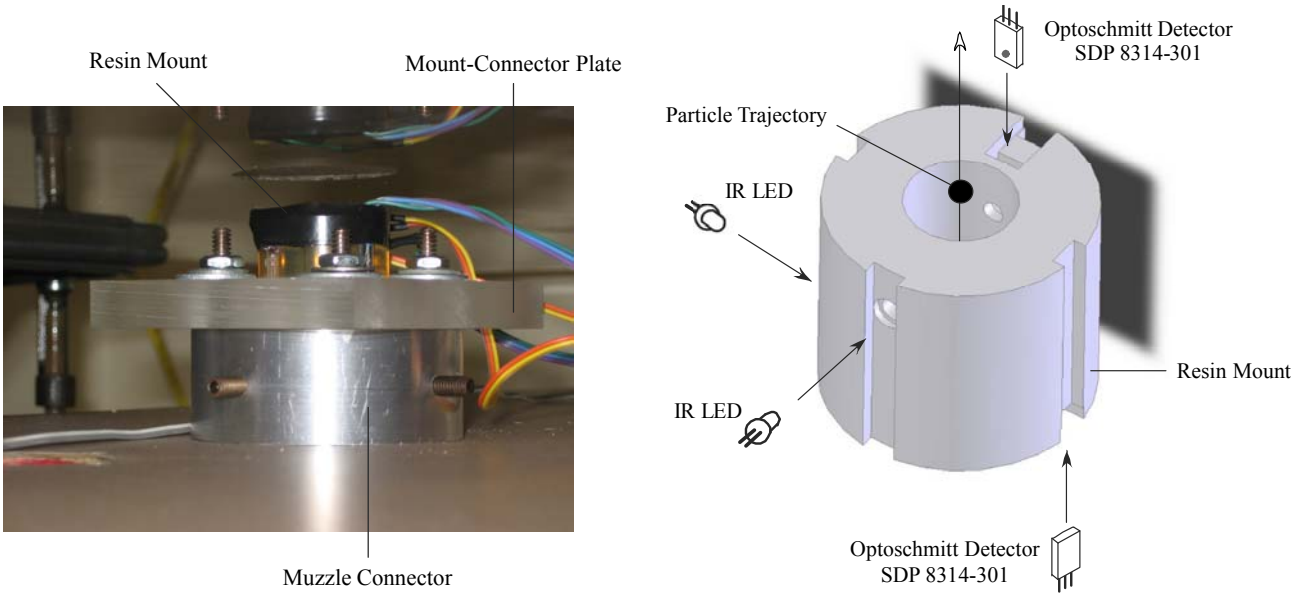

Figure 4-5: Photogates mount
(a) Connection of photogate mount with other elements (b) Location of circuit elements in mount

4.3 Image Analysis

In high speed photography, the raw data of collision studies is a series of successive-frame images of particle trajectory. The REDLAKE software from the manufacturer of MotionScope® PCI high speed camera have been used in this study in order to calculate the approach and rebound velocities and relative position of the particle in each frame and results were exported to separate data files for each collision event. Additionally, the coordinates of left corners of the images and two arbitrary points on the anvil surface were measured for each event and reported in the exported file of event (See Figure 4-6 (a)).

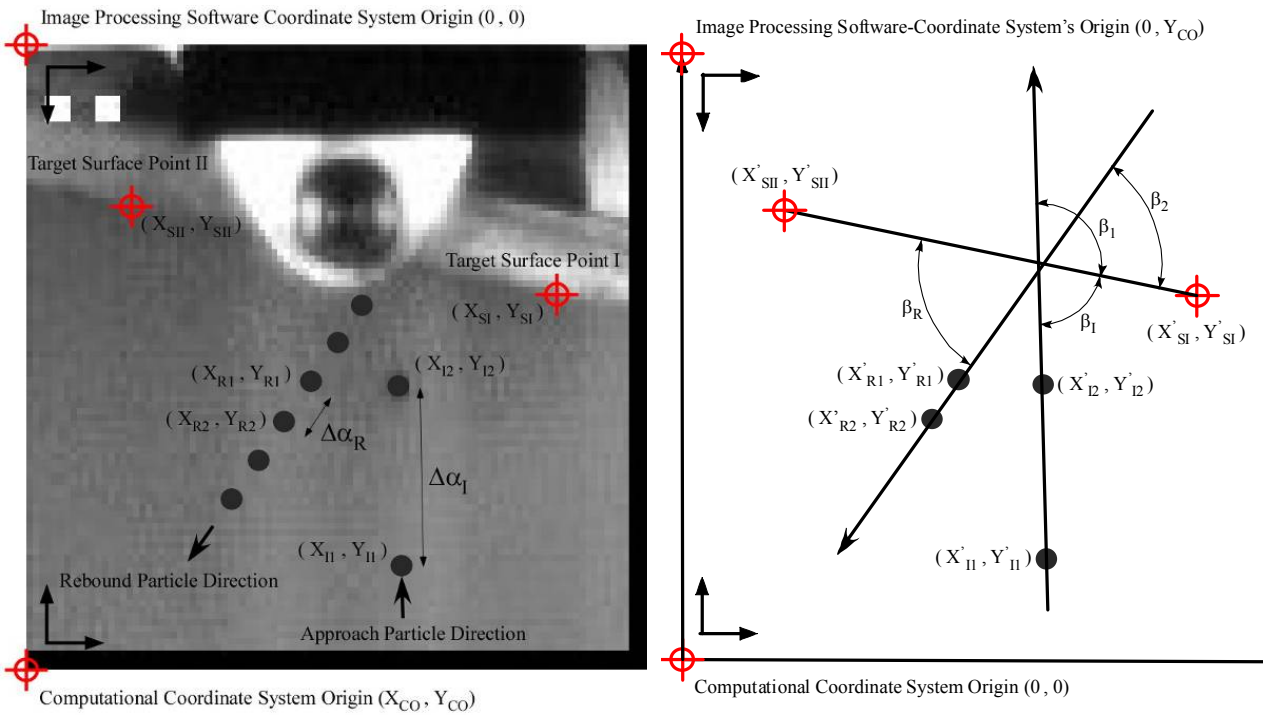

Figure 4-6: Image analysis technique

A series of mathematical manipulations have been done to measure the approach and rebound incident angles. The REDLAKE Image Processing Software assumes the origin coordinate system in upper left corner of the screen. For simplicity in calculations, a transform combination of translation and mirroring is required in order to have the coordinate system in the common X-Y coordinate system with Z axis normal to the plane (See Figure 4-6 (b)).

$$\begin{aligned} X' &= X \\ Y' &= -(Y - Y_{CO}) \end{aligned} \qquad (4\text{-}1)$$

where, primes indicate the coordinates after transformation.

The slopes of approach and rebound particle trajectories and the target plane can be calculated from geometry, knowing two points of each line.

$$\begin{aligned} m_s &= \frac{Y'_{SI} - Y'_{SII}}{X'_{SI} - X'_{SII}} \\ m_I &= \frac{Y'_{I1} - Y'_{I2}}{X'_{I1} - X'_{I2}} \end{aligned} \qquad (4\text{-}2)$$

$$m_R = \frac{Y'_{R1} - Y'_{R2}}{X'_{R1} - X'_{R2}}$$

Knowing the slope directions, the angles between the target surface and Approach/Rebound direction can be obtained.

$$\beta_1 = \frac{m_s - m_I}{1 + m_s m_I}$$
$$\beta_2 = \frac{m_s - m_R}{1 + m_s m_R} \qquad (4\text{-}3)$$

The restitution coefficients are the ratios of velocities components normal and tangential to the plates, which by knowing the approach and rebound velocity vectors, the components can be calculated in the restitution coefficients.

$$e_N = \frac{V_{RN} Sin(\beta_R)}{V_{IN} Sin(\beta_I)} = \frac{\frac{\Delta\alpha_R}{\Delta t} Sin(\beta_R)}{\frac{\Delta\alpha_I}{\Delta t} Sin(\beta_I)} = \frac{\Delta\alpha_R Sin(\beta_2)}{\Delta\alpha_I Sin(\pi - \beta_1)}$$
$$e_T = \frac{V_{RT} Cos(\beta_R)}{V_{IT} Cos(\beta_I)} = \frac{\frac{\Delta\alpha_R}{\Delta t} Cos(\beta_R)}{\frac{\Delta\alpha_I}{\Delta t} Cos(\beta_I)} = \frac{\Delta\alpha_R Cos(\beta_2)}{\Delta\alpha_I Cos(\pi - \beta_1)} \qquad (4\text{-}4)$$

In equations (4-4), velocities can be directly substituted from the REDLAKE results or calculated from the distances that particle passed in a period of time between two successive frames.

4.4 Direct Compressed Air Shooting (Capstone Design)

Using high pressure air in the barrel to directly accelerate the particle was the technique utilized by the Capstone design team under the supervision of Prof. Taslim at Northeastern University, 2006.

(a) (b)

Figure 4-7: Direct compressed air setup

The system consisted of a removable barrel with a bore diameter equal that of the particle which connected to the building's compressed air line (Low Pressure) with a solenoid control valve and a pressure regulator in between. The terminal velocity of the particle at the end of the barrel could be controlled by the amount of air flow set with the pressure regulator. A vertical feeder was mounted on the top of the barrel mount for injecting particles into the barrel. For safety, all the components, including the anvil and photogates were located in a see-through bullet proof box (See Figure 4-7). By applying voltage to the solenoid valve, the compressed air flew in the system and accelerated the particle using the dynamic pressure of the flow. Position of barrel in this setup was horizontal which affected the particle trajectory with gravitational forces in low velocities. Two IR photogates were mounted in front of barrel to capture the particle movement, in order to trigger the high speed camera. The anvil was designed as a fixture to hold different target plates with rotational capability to study the oblique impacts.

A series of experiments have been done with this setup for brass particles, impacting aluminum target plate at different incident angles for a range of velocities (raw data sheets of analyzed images are attached in Tables C.1-C.5 in Appendices). Summaries of results and calculated restitution coefficients are discussed in the Results and Discussion section.

Because of barrel's caliber and particles-size tolerances, usually particles started bouncing on the internal barrel wall during the acceleration which gave a rotational motion to the particles. The deviation of trajectory from barrel axis was compounded in the horizontal barrel position by the gravity field, especially at low velocities. At higher air pressures, the impingement effect of the air jet on the wall drifted the particles with different angles of approach, not necessarily normal to the camera view axis. These deviations decreased the accuracy of measurements and a large area of craters for a fixed incident velocity could be seen on the target plate. Additionally, comparing the infrared beam cross sectional area with the particle size as well as the trajectory deviations increased the probability of the particles not crossing the beam. In the worst case, one out five shootings was captured by photogates and the triggering signal was sent to the camera.

4.5 Viscous Driven Accelerator

Fluid viscosity of applies shear stresses on the particle surface in contact with the flow. The vector summation of these forces in the flow direction is known as drag. In the studies of particle trajectory in the presence of viscosity, drag forces have a major role both in accelerating and decelerating the particles with respect to the flow velocity. Flow over a sphere is a much studied subject in fluid dynamics and many studies have been done on different aspects of the problem.

Assume a spherical particle of velocity u_P with diameter d_p surrounded by a vertical parallel flow with a velocity magnitude of U, relative velocity of $u_P\big|_{rel.}$ and in the gravitational field of g.

$$u_P\big|_{rel.} = U - u_P \tag{4-5}$$

The main forces apply on this particle are gravitational and viscous forces. The vector summation of these forces determines the particle to accelerate or decelerate. For gravitational forces, one can use equations (2-1). Introducing a new variable as particle acceleration $a_G = (1 - \frac{\rho_a}{\rho_P})g$ due to gravitational forces, then,

$$F_{Buoyancy} = \frac{4\pi d_p^3}{3}\rho_p a_G \tag{4-6}$$

Depending on the regime, different equations for the drag forces on a sphere have been reported by the investigators. The particle Reynolds number $\mathrm{Re} = \frac{\rho u_P\big|_{rel.} d_P}{\mu}$ indicates the type of flow regime passing the particle. For $\mathrm{Re} \le 2$, the Stokes flow assumption governs the equations of fluid particles and viscosity forces are dominant. Exact analytical derivations explain the behavior of flow in this region. For $2 < \mathrm{Re} \le 100$ viscousity effects are comparable with inertial forces, but still one can expect the smooth flow around the sphere without vortex shedding in the downstream. In $\sim 100 < \mathrm{Re}$ Von Karman Street vortices start to shape and as Reynolds number increases the drag coefficient decreases. In each range of these Reynolds number, an analytical or empirical equations is presented for the drag Coefficient with reasonable accuracy (See Table 4-1).

Table 4-1: Drag coefficient in different flow regimes

Reynolds Number	Drag Coefficient
$\mathrm{Re} \le 2$	$C_D\big\|_{Stokes} = \frac{24}{\mathrm{Re}}$ (4-7)
$2 < \mathrm{Re} \le 100$	$C_D\big\|_{Laminar} = 0.44$ (4-8)

100 < Re	$C_D\big\vert_{Turbulent} = 0.2$	(4-9)

One can write the Newton second law, by applying the drag and buoyancy forces as external forces on a particle body.

$$\frac{4}{3}\pi d_p^3 \rho_p \frac{d^2x}{dt^2} = F_{Buoyancy} - F_{Drag} \qquad (4\text{-}10)$$

where, $F_{Drag} = \frac{1}{2}\rho_a(\pi d_P^2)u_P\big\vert_{rel.}{}^2 C_D$.

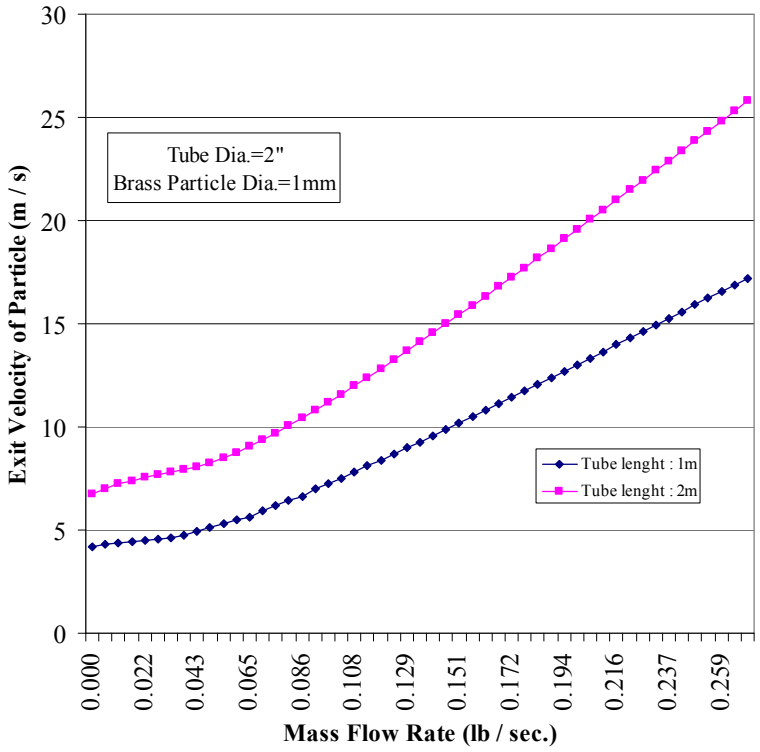

Figure 4-8: Final particle velocity with respect to mass flow rate of air

A mathematical Code has been written to track a falling particle trajectory in a vertical- parallel duct flow (Code A.1). The code then used for modeling a falling brass particle (~1 mm Diameter) in a vertical duct (2" Diameter) with downward air flow for two different drop heights (Figure 4-8). With the help of numerical results, obtained by modeling, a new setup of viscous

driven accelerator was designed and erected in the Gas Turbine laboratory of Northeastern University (See Figure 4-9(a) & A.1-5).

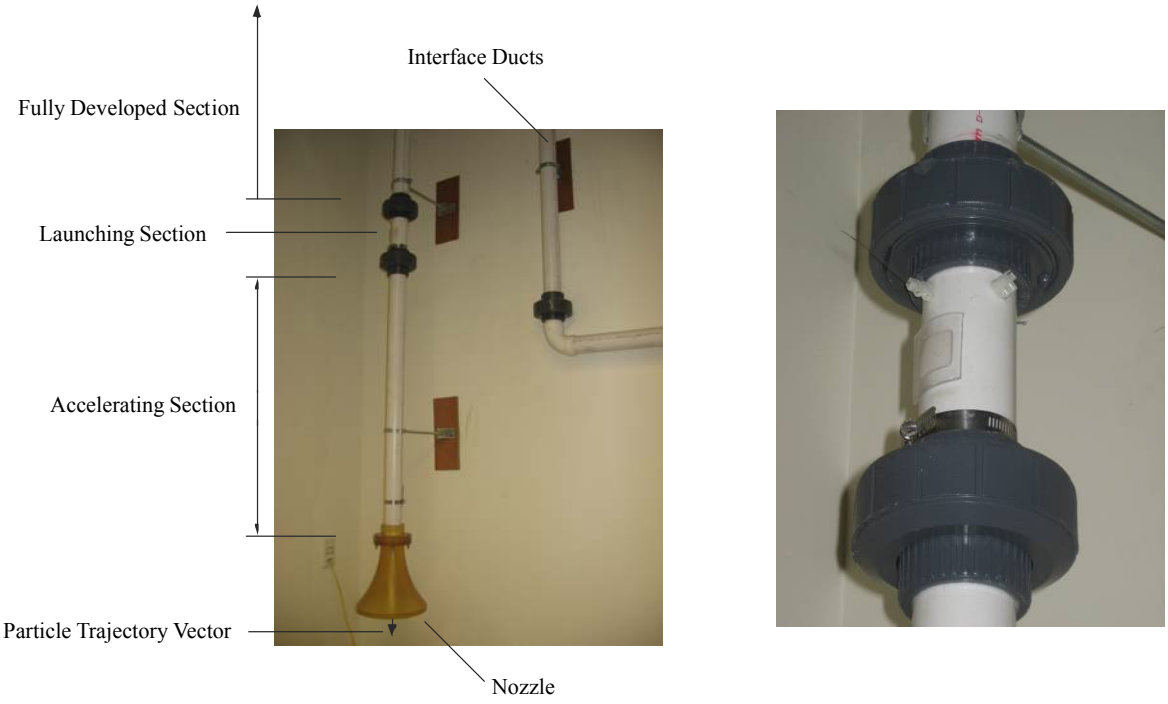

(a) (b)

Figure 4-9: Viscous driven accelerator – general design
(a) General assembly (b) Particle launcher

The system consisted of a series of interface plumbing to convey compressed air flow from local compressor (High Pressure) to the apparatus. A rather long vertical duct as a flow developing section was installed before the particle launcher in order to satisfy the parallel flow assumption. At the center line of this section a 3/32" brass vacuum line was mounted with miniature elastic piano wires to hold the particle in place before launching. The launcher itself is a duct segment with access to the tip of vacuum line in order to place the particles in the system (See Figure 4-9(a)). The accelerating section is a hollow vertical duct that allows the particle to accelerate in the presence of the air flow. At the muzzle of this section a divergent nozzle with a half angle of ~8^{o} was mounted in order to prevent any separation of exiting air jet from the nozzle wall. A number of experiments have been done with this setup for brass particles impacting on an

aluminum target plate with different incident velocity vector. (raw data sheets of analyzed images are shown in Tables D.1-D.4 of the appendices). Summaries of results and calculated restitution coefficients are discussed in Results and Discussion section.

In particle free fall studies, it was noticed that particles did not follow the same path as the axis of the accelerator, but again the target plate became a trace of many distributed craters in a circle of 2 cm in diameter. Different reasons can be the sources of these deviations in free fall. Local air streams around the setup probably can alter the particle from vertical decent. This probability was too small as the most trajectory path of the particles happened in the confined area (accelerating section). As mentioned before, the particle release system in this setup was based on the vacuum suction pressure in a 3/32" brass pipe which was mounted securely along the axis of the accelerator. Experimental results demonstrated that the particle deviation from the pipe centre axis depended on the ball valve closing time for vacuum line. The slower the closing time was, the more deviation from axis had been seen. It is speculated that the contact surface of brass pipe and the particle should be symmetrical in order to have a sudden detachment. Moreover, because of geometrical position of the setup in the lab and a rather long vacuum line, changes in vacuum line pressure transferred to the particle with a delay, or in some cases, even the particle stuck in the opening of brass pipe. Along with all these deviations, which altered the assumption of planar impact, triggering the camera by photogates was one of the obstacles of experiment. In many cases, the deviated particle did not cross the beams and camera did not capture the images. For higher air velocities, the probability of tracing the falling particles was almost impossible. In this type of setups, because of very small size of particles and their very high velocities, using the curtain photogates to cover larger areas was not practical. Additionally, Figure 4-8 predicts

only a terminal particle velocity around ~20 m/sec, which is way below the velocity ranges in an IPS, with the limited air flow rate of the high pressure compressor in the lab.

4.6 Indirect Compressed Air Shooting (Preliminary Design)

In viscous driven accelerator, to accelerate a particle to high velocities, a tremendous amount of continuous air flow was required, which were accompanied with vibrations in the system and separation of unsteady flow at the outlet. Additionally, deviation of particle trajectory was resulted from direct particle/air flow interaction, which by the presence of unsteady flow, this effect was more dominant. To avoid this direct interaction deficiency, an interface boundary, was considered to avoid the direct particle/air flow contact. The idea was originated from the free moving piston-cylinder concept. The compressed high pressure air behind the piston exerts uniform forces which accelerate the piston. If the piston is designed as a particle carrier, eliminating any particle-flow interaction, the particle would have the same speed as that of piston at the end of accelerating, phase as a unified mass. Figure 4-10, presents a schematic diagram of this process. In phase (A), the particle is launched in the sabot (piston), and the sabot is at its initial position. With initiating high pressure compressed gas, the sabot including the particle starts to accelerate (phase (B)). Reaching to the end of the barrel, the sabot will impact with a spring stopper (phase (C)). During this impact, the particle will continue moving along the piston axis with the speed of the piston at the time of collision. In return the piston is pushed back by the elastic forces of compressed spring and discharges the used compressed gas stored in the barrel (phase (D))

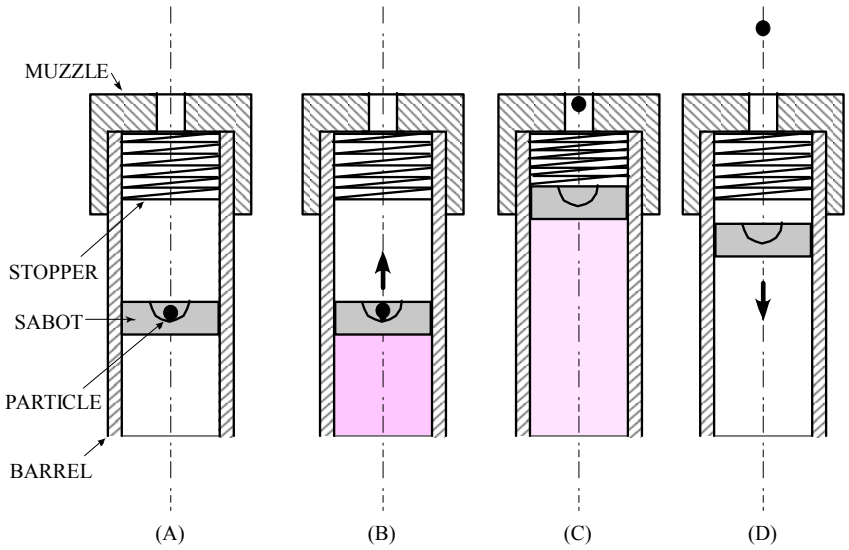

Figure 4-10: Schematic diagram of indirect compressed air shooting

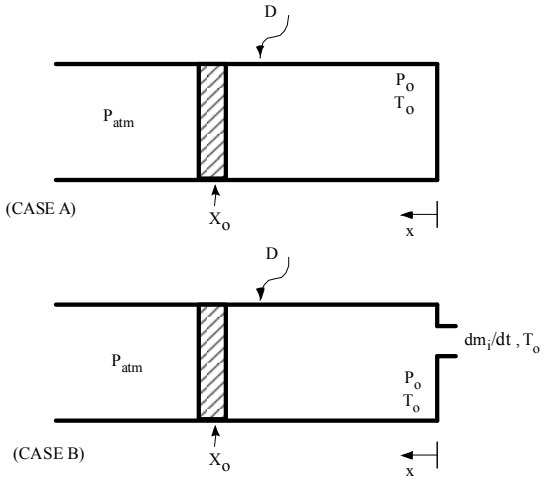

Figure 4-11: Schematic diagram of piston-cylinder modeling

For inducing the high pressure gas behind the sabot, two different models were studied in order to predict the pressure behavior with respect to the movement of sabot, and its final velocity (Figure 4-11). In case (A) high pressure compressed gas was stored behind a pinned stationary piston, which suddenly was released and the compressed gas started to expand. In contrary, case (B) was the modeling of free moving piston-cylinder in atmospheric pressure, which suddenly was initiated with incoming high pressure gas as an inlet to the system and accelerated the piston.

In case (A), assume high pressure compressed gas with pressure P_o and temperature T_o is stored behind the pinned stationery piston in a cylinder (Diameter D) at position x_o with respect to the origin. By releasing the pin, piston starts to move due to the exerted pressure. At any instant, the ideal gas equation and the piston-cylinder volume can be written as;

$$PV = m\frac{R}{M}T \tag{4-11}$$

$$V = \frac{\pi D^2}{4}x \tag{4-12}$$

Substituting the volume (V), from Equation (4-12) in to Equation (4-11),

$$m = \frac{\pi D^2}{4}\frac{M}{R}\left(\frac{Px}{T}\right) \tag{4-13}$$

It can be deduced that:

$$\left(\frac{Px}{T}\right) = Cons. \tag{4-14}$$

Similarly, one can write the conservation of energy equation as:

$$\begin{aligned} \frac{dE}{dt} &= -P_{atm}\dot{V} - \frac{1}{2}M_P\dot{x}^2 \\ \frac{d}{dt}(mc_vT) &= -P_{atm}\frac{\pi D^2}{4}\dot{x} - \frac{1}{2}M_P\dot{x}^2 \end{aligned} \tag{4-15}$$

For the piston as an isolated mass system, Newton's second law is valid and can be written as,

$$m_P\ddot{x} = (P - P_{atm})\frac{\pi D^2}{4} \tag{4-16}$$

In summary, the governing equations for a system of piston-cylinder in case (A) are,

$$\begin{cases} \left(\dfrac{Px}{T}\right) = \dfrac{4Rm}{\pi D^2 M} & (a) \\ mc_v \dfrac{dT}{dt} = -P_{atm}\dot{V} - \dfrac{1}{2} m_P \dot{x}^2 & (b) \\ m_P \ddot{x} = (P - P_{atm})\dfrac{\pi D^2}{4} & (c) \end{cases} \tag{4-17}$$

In case (B), a system of piston-cylinder, initially at atmospheric conditions, is under consideration, and is exposed to a continuous inlet mass $\dot{m}_i$ of the same gas inside the chamber. The piston can freely move along the cylinder and, at any instant, Equation (4-13) is valid for the system except for constant mass (m) which should be substituted by $\widetilde{M}$ as a function of time. Rewriting Eq. (4-13) in terms of $\dfrac{Px}{T}$, we get

$$\widetilde{M} = \frac{\pi D^2 M}{4R}\frac{Px}{T} \tag{4-18}$$

For the control volume of piston-cylinder with inlet mass, the continuity equation has the form of

$$\frac{d\widetilde{M}}{dt} = \dot{m}_i \tag{4-19}$$

Substituting Eq. (4-18) in to Eq. (4-19) and rearranging all terms, the conservation of mass in piston-cylinder system can be written as,

$$\frac{d}{dt}\left(\frac{Px}{T}\right) = \dot{m}_i \frac{4R}{\pi D^2 M} \tag{4-20}$$

Similarly, applying the conservation of energy for this system with the bulk flow as an inlet,

$$\frac{dE}{dt} = -P_{atm}\dot{V} + \dot{m}_i h \tag{4-21}$$

Recalling $E = \widetilde{M} c_v T$, $h = c_p T_o$ and substituting Eq. (4-20) into Eq. (4-21), the general form of the energy conservation will be:

$$c_v \frac{\pi D^2 M}{4R} \frac{d}{dt}(Px) = -P_{atm} \frac{\pi D^2}{4} \dot{x} + \dot{m}_i c_p T_o \tag{4-22}$$

Neglecting the friction dissipations for the piston as an isolated mass system, Newton's second law is valid and can be written as,

$$m_p \ddot{x} = (P - P_{atm}) \frac{\pi D^2}{4} \tag{4-23}$$

In summary, the governing equations for a system of piston-cylinder in case (B) are:

$$\begin{cases} \dfrac{d}{dt}\left(\dfrac{Px}{T}\right) = \dot{m}_i \dfrac{4R}{\pi D^2 M} & (a) \\ c_v \dfrac{\pi D^2 M}{4R} \dfrac{d}{dt}(Px) = -P_{atm} \dfrac{\pi D^2}{4} \dot{x} + \dot{m}_i c_p T_o & (b) \\ m_p \ddot{x} = (P - P_{atm}) \dfrac{\pi D^2}{4} & (c) \end{cases} \tag{4-24}$$

A numerical finite difference scheme in FORTRAN compiler has been developed to model nonlinear-unsteady Equations (4-17) and (4-24) with respect to time (Code B.1). The code then was used for modeling of an aluminum sabot (~3.175 cm Diameter and ~20 gr Mass) in a vertical barrel (~3.175 cm I.D. and 1.00 m length) with upward air flow (~0.145 kg/sec).). Results show that generating a high initial pressure behind the sabot does not have a significant effect on the final velocity of the particle. Based on the numerical results a new setup of indirect compressed air shooting was designed and erected in the Gas Turbine laboratory of Northeastern University (See Figure B.1-5).

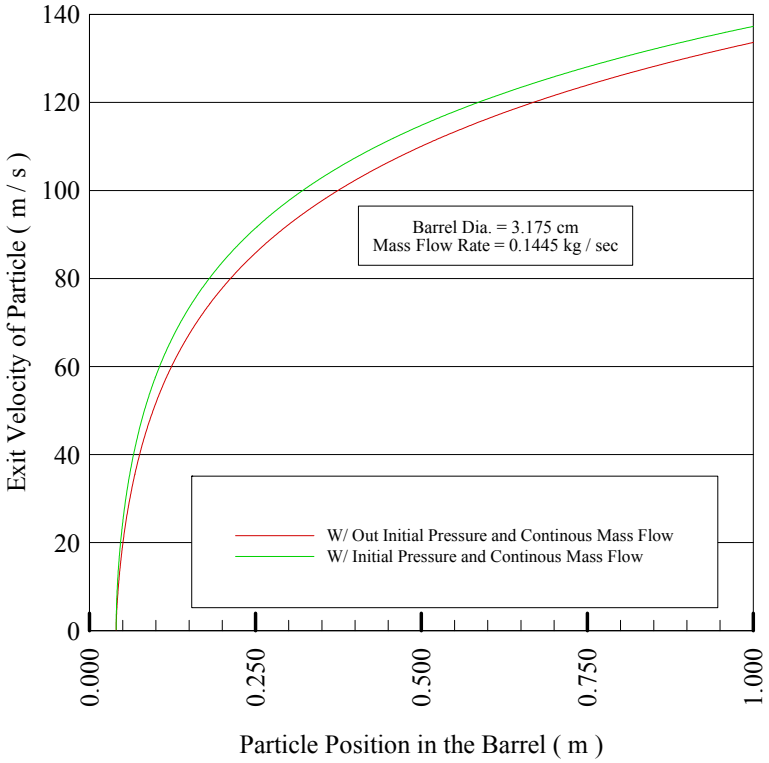

Figure 4-12 Final velocity of shooting particle in preliminary design

In some preliminary tests, it was noticed that during the shooting process, when the maximum air flow was sent into the system, a considerable amount of bending momentum was applied on the high pressure flexible hose, that connected the barrel system to the main high pressure line which made the system unsecured. The applied stress required a strong structure that had to be mounted to the lab floor to avoid any movement of the system. Increasing the size of the system made the vertical alignment of the barrel problematic and required a precise aliment system which was expensive and had a short maneuverability range.

Also these experiments demonstrated a drastic decrease in the shooting particles velocity at the end of the barrel in the order of 10 m/sec. Reviewing back all the calculations, it was noticed that in design of the system, the valve opening time was neglected and step function was used for modeling the inlet flow rate of air. In practice, the flow rate behavior of air was found to be more similar to a slope function rather than step function. That means a monotonic increase in the air

mass flow rate from zero to the maximum flow rate available in the system. Figure 4-13 shows the data results of recompiling the code with new assumptions for different valve opening times.

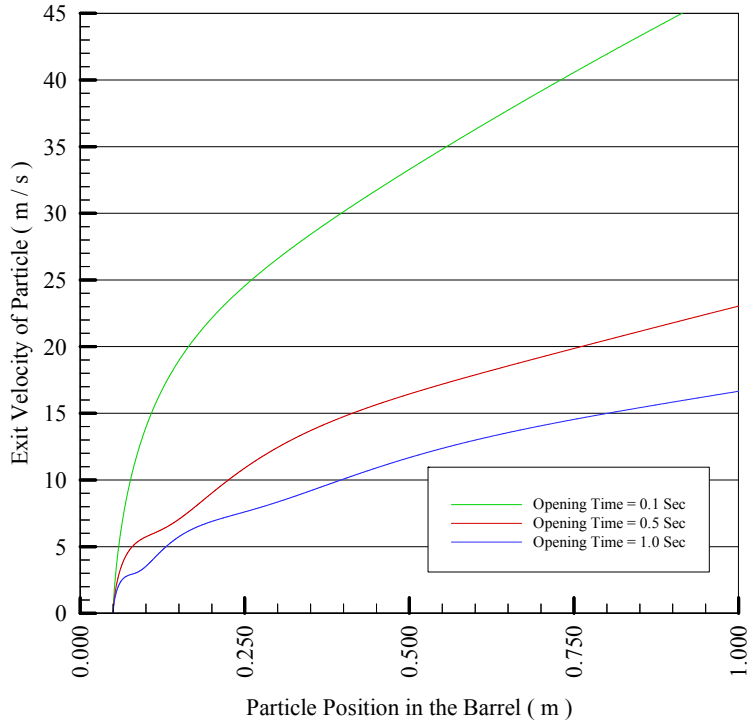

Figure 4-13 Final velocity of shooting particle in preliminary design

These data demonstrated that, reaching higher velocities depicted in Figure 4-12, the opening time should be much less than 0.001 seconds. Fulfill this requirement, the existing valve should be replaced by a new control valve with short response time. These types of control valves are custom-made and are not available as stock items. Taking into account the problematic vertical alignment procedure of the barrel and expense of substituting the new control valve with short response time, this design was not developed further for data gathering.

4.7 Indirect Compressed Air Shooting (Final Design)

In all different methods described earlier, lack of precise trajectory path of particle and inability to control the speed of particle were the source of errors in measurements. The lack of particle‘s trajectory preciseness was overcome by the use of indirect compressed air shooting

method as described in Section 4.6, but still the control of the speed and reaching the high velocities required tremendous amount of compressed air and short response control gate valves. These failures in shooting system were voided in the modified new indirect compressed air shooting system, known here as Final Design. The idea stemmed from the functionality of paintball guns (Markers). The valve set, installed in the paintball marker, releases the high pressure compressed gas in a fraction of second. This time interval is in the order of hundreds of micro seconds which met the requirement of a short response control gate valve. The system includes a hammer, a case, a needle and a high pressure valve (Figure 4-14-A). At the first stage, the compressed gas is kept in high pressure chamber by the needle and spring. Because of the needle's shape, the compressed gas itself helps the needle secure the channel avoiding any leakage (Figure 4-14-B). By triggering the system, the hammer (Mass) is released and accelerated by the compressed spring force behind it. When the hammer with large momentum hits the needle, it can overcome the needle's spring force and applied pressure of compressed gas on it which cause the needle to move backward and open the channel for letting the compressed gas go through it to the launcher side (Figure 4-14-C).

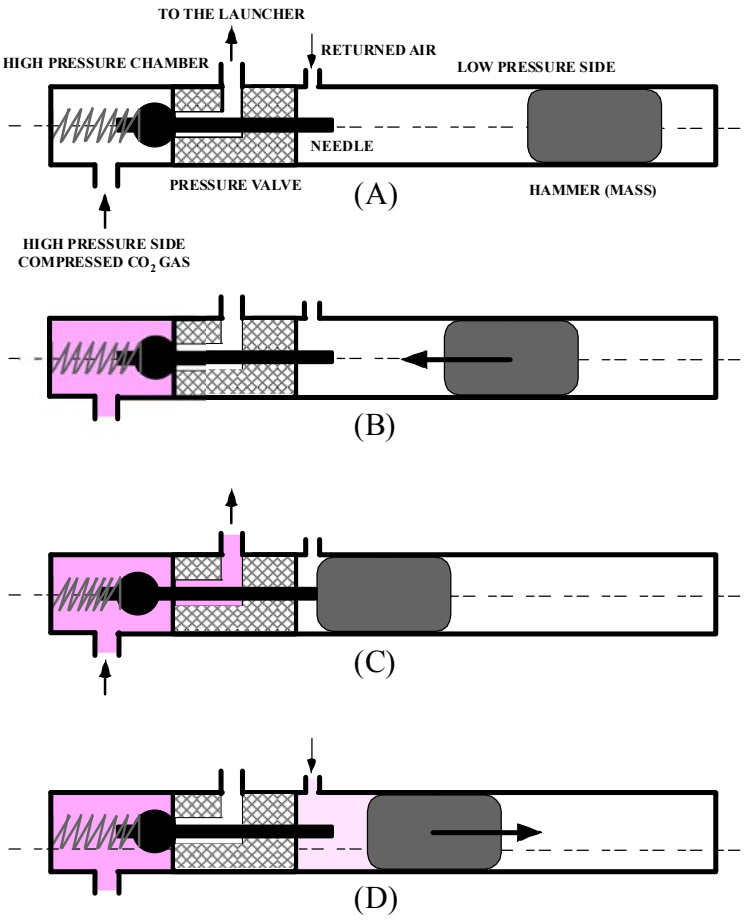

Figure 4-14 Paintball marker's high pressure mechanism diagram

The time interval of high pressure valve opening would not last more than a few hundreds of microseconds. The needle under the compressed spring force shuts off the flow. A portion of the compressed gas which goes through the channel to the launcher side comes back through the return air channel to the low pressure side and pushes back the hammer to its initial secured place (Figure 4-14-D). As a result, the flow of compressed gas is released in a fraction of a second. By connecting the launcher channel to the indirect compressed air shooting system, one can reach higher velocities as we desired in Section 4.6. Based on the above hypothesises, a new setup of indirect compressed air shooting system was designed and erected in the Gas Turbine laboratory of Northeastern University (See Figure C.1-6).

(a) (b)

Figure 4-15 General Arrangement
(a)Wall-particle impact setup (b) Image analysis setup

This system consisted of two sections: Wall-particle impact setup and image analysis setup (Figure 4-15). The Wall-particle impact setup was set up based on the Final Design (Figure C.1-6) which was mounted on two isolated tables avoiding any transfer of vibration to the anvil. A paintball marker "View Loader Triton II" was installed on the setup for releasing the high pressure compressed CO_2.

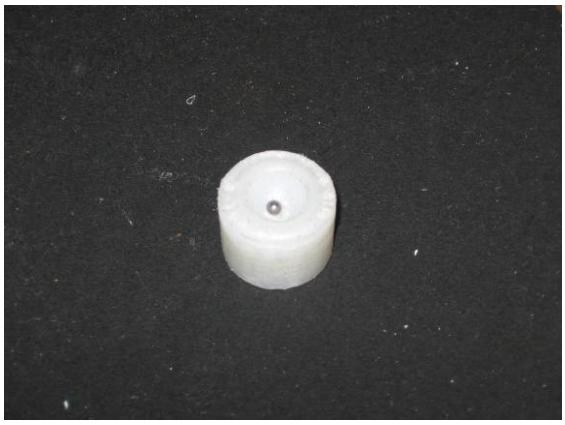

Figure 4-16 Sabot view with launched stainless steel sphere

. A 2.55 gr scarified sabot made from neoprene plastic (1.758 cm in diameter) was used as a small particle carrier it was at the interface between the high pressure gas and the particle (Figure 4-16). Because of hard compaction which happened during the collision of the sabot and the

stopper spring at the end of the barrel, the sabot sustained considerable deformation and erosion and had to be replaced after several uses.

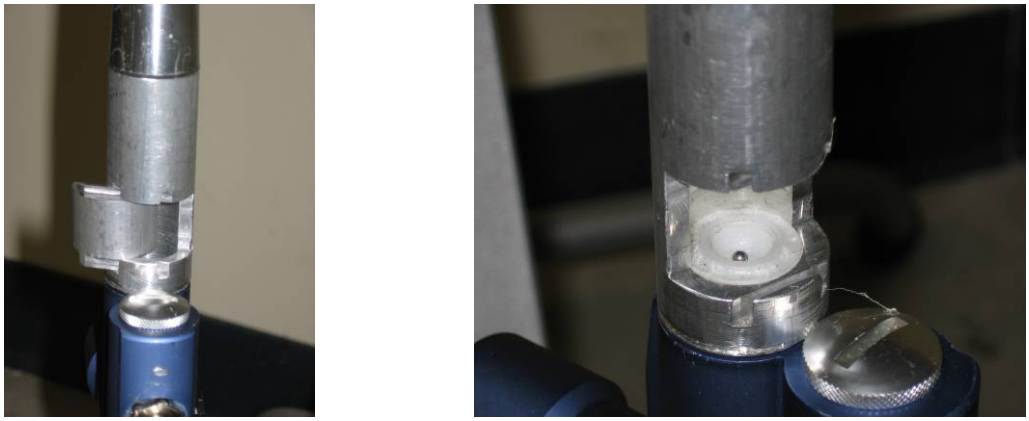

(a) (b)

Figure 4-17 Launcher section
(a) General view (b) Launched sabot

Between the barrel and the marker a launcher section was mounted in order to launch the loaded sabot in the system. The launcher was sealed by a cover when the loaded sabot rested in its position thus eliminating any gas leakage. The same triggering system was used as described in Section 4.2.

The system worked with high pressure compressed CO_2. The tank preussure calculated by Eqn. 4-25.

$$P = 314.04[psi]\exp\left(\frac{T}{69.64[^\circ F]}\right) \qquad (4\text{-}25)$$

For the standard temperature of $T = 77^\circ F$, the CO_2 pressure in the tank would be approximately 65.5 bar (~949 psi). Based on these data, the Code B.1 then was run for a barrel with 20 cm length and 1.758 cm caliber exposed to effective pressure of ~16.5 bar with initial volume of 4 cm^3 of pure CO_2 gas. The results demonstrated a sabot velocity of ~1120 m/sec after traveling 8 cm in the barrel. Of course the actual velocity was slightly lower due to the system leaks and opening time interval of the high pressure valve opening .A series of experiments were done with

this setup for stainless steel particles, impacting aluminum target plate at different incident angle for a range of velocities (raw data sheets of analyzed images attached in Tables E.1 in the appendices). Summaries of results and calculated restitution coefficients are discussed in the Results and Discussion section.

4.8 Results and Discussion

Three different setups were designed, manufactured and tested in this study. The experimental results are presented in Figure 7-1 through Figure 7-24. In the Capstone Design and Viscous driven setup, dependency of normal restitution coefficient (NRC) on impact velocity has been confirmed (Figure 7-1 and Figure 7-14) validating the prediction of restitution coefficients by Equations 3-15 through 3-20. Behavior of NRC trend for 10 psi in Figure 7-14 probably is because of error in data gathering or local surface asperities. The immobility of the anvil kept the history of indentations on the target surface for further collisions. These asperities deviated the angle of impact. To overcome this problem, it is suggested that the target plate be replaced after each collision or shifted to a new position to avoid multiple collisions on the same spot on the target plate. No strong dependency found between tangential restitution coefficient (TRC) and the impact velocity (Figure 7-2). Capstone Design data demonstrated an increase in measurement accuracy of NRC with the impact velocity of the particle. A possible explanation for this accuracy is the domination of the inertia forces for shooting particle in the jet flow. On the other hand, the large error interval of TRC for all Capstone Design experimental data is conspicuous. The impingement jet of air which was discharged from the barrel caused a deviation in rebounded particle trajectory. In all cases, the values of restitution coefficients were more accurate in normal impact (Less than 5% error) and divergencies of data were observed in the glancing angles (~ 20%). The error interval of inbound angle for all Capstone Design and

viscous driven setup data was less than $\pm 1.95\,\mathrm{deg}$. Comparing the first two apparatuses, the viscous driven setup had more accuracy of measurement especially in free fall conditions (eliminating the particle-air flow interaction error), but for higher velocity and pressure results showed high inaccuracies in the measurements. In higher flow velocities, the particle trajectory deviated from a straight normal path because of highly complex turbulent flow at the exit of nozzle. However, for very low velocities, the free fall setup showed very good accuracy of less than 1%. Both cases showed very poor behavior at high velocities. However, the preliminary data obtained from final design setup (Figure 7-23 and Figure 7-24) at high velocities of ~100 m/sec in worst cases had the error interval of less than 20%. The recent data obtained with this setup in the Gas Turbine laboratory of Northeastern University demonstrated less than 6% error intervals. The rather large precision error of impact angle measurement was due to loose barrel during the triggering. The fixture mounted on the barrel became loose after repeated shooting because of the pushing back forces of the triggered gun and caused uncertainty in measurments of the incident angle changed with some uncertainty. A new structure mounted to the ground is required to firmly hold the gun thus avoiding any misalignment.

CHAPTER 5 NUMERICAL MODELLING OF IMPACT

5.1 Overview

For obtaining a general correlation between restitution coefficients and other impact parameters, which is valid over a wide range of particle velocity and is required diameter a tremendous amount of measurement studies for each case, is required. One solution is using a numerical method to model the behavior of collision and predict the restitution coefficients and other kinematic properties of colliding particle after collision. Numerical modeling can save loads of time and energy for predicting the parameters. However, the bottleneck of these methods is unreliability of numerical simulation results. A prevalent approach is to validate the numerical data of standard test cases with experimental results and calibrating the numerical model for each special case. This study presented the results of finite element commercial code for the simulation of wall-sand particle collision for a range of velocities applicable to the IPS for different particle sizes. ABAQUS® a commercial finite element software was used to model the unsteady, completely elastoplastic impact problem.

5.2 The Finite Element Model

The oblique collision of a spherical particle with a target wall can be illustrated by Figure 3-1. As discussed earlier, the collision phenomenon happens on a plane normal to the target wall, so by planarity characteristic of impact phenomena, only half of the geometry was required to be solved to obtain the rebound characteristics. Disk shape deformable plate was used as the target plate. It is reported that if the dimension of the target plate is some order magnitude greater than the particle diameter, it then has no effect on the numerical solution[46]. For each particle

diameter case, the dimension of target plate was also scaled with the same aspect. Unstructured tetrahedral grid with non-uniform seed distribution on edges applied on both parts. The undeformed mesh is shown in Figure 5-1. Fully fixed boundary conditions specified on the side of cylindrical plate and symmetry boundary conditions applied on the cutting plane for both parts. The plate and projectile material properties were not identical. They had different Young modulus of elasticity, Poisson's ratio and density. The yield stress of the material was specified as a function of the equivalent plastic strain at different equivalent plastic strain rates for each of the materials. The general contact algorithm applies for defining the contact problem with all parts faces involved. The dynamic friction coefficient as a function of incident angle with respect to the Sommerfeld's data [32] was set for each cases separately. A "key point" was defined at the center of the particle to track the history of particle velocity at the centroid point. Velocity components for each impact incident angle and velocity magnitudes were calculated and applied to the model as the initial boundary condition. The environment variable pre_memory was set to 1000 MB to run this analysis with ABAQUS/EXPLICIT Solver.

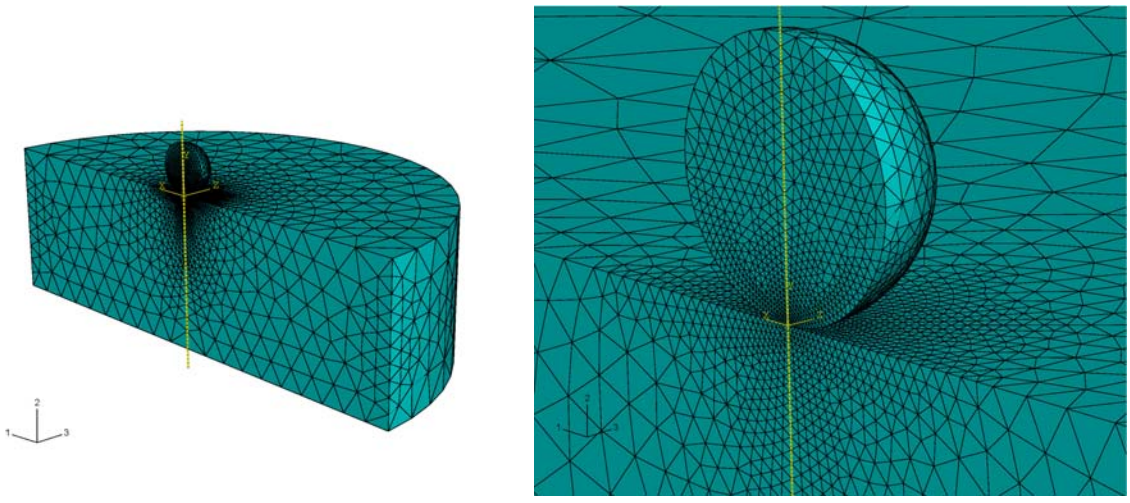

(a) (b)

Figure 5-1 Undeformed tetrahedral mesh generated for wall-particle iImpact

Deformed shapes with stress distribution at different stages of the analysis are shown in Figure 7-49 for a 150mμ sand particle with 100m/sec impact velocity to an Aluminum plate at a 45^{o} incident angle. As shown in Figure 7-49, the projectile eventually put the permanent crate on the target plate and leaves the surface with rotational velocity. Figure 5-2 compares velocity components histories of defined the Key point to calculate the normal and tangential restitution coefficients.

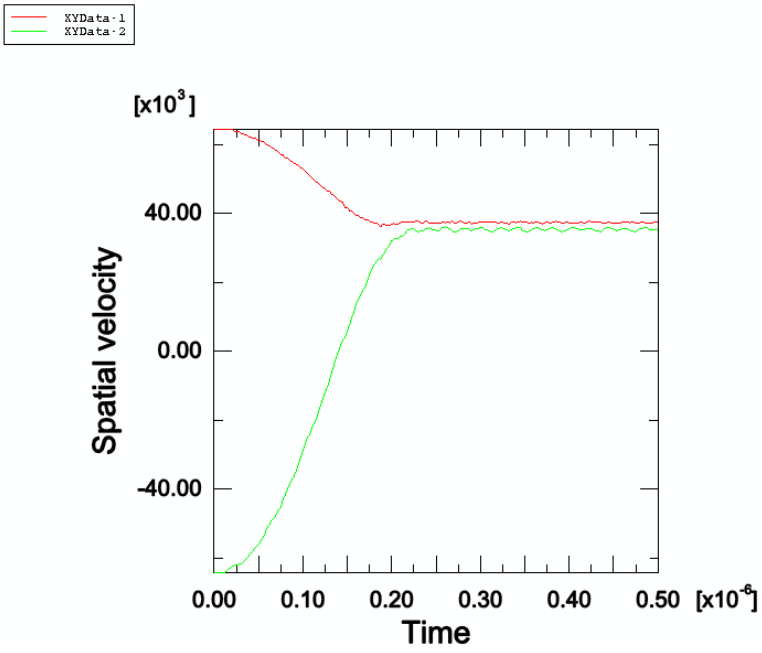

Figure 5-2 Velocity components histories of defined key point at the particle centroid

5.3 Calibration Method

A set of experimental data were found in open literature survey and modeled in order to calculate the restitution coefficients. The numerical results then were compared with the experimental data to calibrate the physical parameter set in the numerical model. Material properties and nomenclatures were found to be fading in those reports because of different material standards and incompatibility of them especially in presenting the mechanical

properties. Trial and error approach was taken in the modeling to find the nearest value of the experimental data in a family standard of materials. Taking into account that the friction coefficient has the minimum effect on normal compact, this procedure was used for normal impacts. Then the model was run for oblique impacts for in a range of incident angles by knowing the material used for experimental data. For each of the incident angles the dynamic friction coefficient then was calibrated with the trend of Sommerfeld et al. results [32] in order to match with experimental data. The results are presented in Figure 7-25 through Figure 7-34. Good agreement is observed between the calibrated dynamic friction factor and Sommerfeld's results, validating the prediction of higher dynamic friction coefficient because of the dominancy of surface roughness in glancing angles.

5.4 Results and Discussion

Based on calibrated values of dynamic friction coefficients obtained for different particle diameters, the model was run for a range of particle diameters in C-Spec, ACC and ACF standards for different impact velocities and incident angles.

Particle Diameter (μm):	15, 50, 165, 500, 700
Impact Velocity (m/sec):	05, 10, 50, 100
Incident Angle (^{o}):	90, 75,60, 45, 30, 15

Results are presented in Figure 7-35 through Figure 7-48. It was observed that the tangential restitution coefficients were almost independent of particle impact velocity but rather dependent on the particle size (Figure 7-35 through Figure 7-39). A possible explanation for this dependency regardless of impact velocity is increase of contact surface between the particle and wall which would exert higher frictional forces. On the other hand, the normal restitution coefficients obtained by numerical results were all independent of particle diameter. However,

they showed a strong dependency on the particle impact velocity (Figure 7-40 through Figure 7-43). By comparing the impulse ratios presented in Figure 7-44 through Figure 7-48 and μ_o (Eq. 3-21), no sliding conditions was occurred during the collision process for all the cases under study. Third order polynomials for tangential restitution coefficients (Table 5-1) and fourth order polynomials for normal restitution coefficients (Table 5-2) were used for data curve fitting.

Impact Velocity (m/sec)	Normal Restitution Coefficient Trend Line Equation*
100	$-1E\text{-}06\ \theta^3 + 0.0003\ \theta^2 - 0.0234\ \theta + 1.1338$
50	$-1E\text{-}06\ \theta^3 + 0.0003\ \theta^2 - 0.0219\ \theta + 1.0951$
10	$-5E\text{-}07\ \theta^3 + 0.0001\ \theta^2 - 0.0085\ \theta + 0.9465$
5	$-5E\text{-}07\ \theta^3 + 0.0001\ \theta^2 - 0.0071\ \theta + 0.9637$

Table 5-1 Summary of normal restitution coefficient equations based on numerical results

Particle Diameter (μm)	Tangential Restitution Coefficient Trend Line Equation
015	$-5E\text{-}07\ \theta^4 + 8E\text{-}05\ \theta^3 - 0.0044\ \theta^2 + 0.086\ \theta + 0.3437$
050	$+1E\text{-}07\ \theta^4 - 2E\text{-}05\ \theta^3 + 0.0013\ \theta^2 - 0.324\ \theta + 0.9012$
150	$+2E\text{-}07\ \theta^4 - 3E\text{-}05\ \theta^3 + 0.0018\ \theta^2 - 0.042\ \theta + 0.9394$
500	$+2E\text{-}07\ \theta^4 - 4E\text{-}05\ \theta^3 + 0.0022\ \theta^2 - 0.007\ \theta + 1.0497$
700	$+3E\text{-}07\ \theta^4 - 5E\text{-}05\ \theta^3 + 0.0030\ \theta^2 - 0.068\ \theta + 1.2745$

Table 5-2 Summary of tangential restitution coefficient equations based on numerical results

* All Angles are in degrees,

CHAPTER 6 EFFICIENCY ANALYSIS OF INERTIAL PARTICLE SEPARATOR

6.1 Overview

Efficiency analysis of inertia particle separator system is the performance study of IPS in separating the sand particles from air flow and preventing the digestion of these particles into the engine core. Several studies were reported on IPS analysis by using the particle trajectory methods experimentally and numerically [2, 13, 14, 18-21, 68]. As discussed earlier in most of numerical models, the Tabakoff et al. data [16-21]were reported to be used. These empirical data are reported for some nominal velocities. Experimental results demonstrated the high dependency of restitution coefficients on impact velocity and particle size. To present the effects of restitution coefficient on efficiency of the IPS, it is required to have a flow field in the IPS. Fluent® as a commercial finite volume software for solving the Navier-Stokes equations was used for the analysis of the flow field in the Inertial Particle Separator. Results then compared with the experimental data and the CFX® results. Good agreement was observed between the two numerical models and experimental data, validating the convergency of solution and mesh independency. Results of the flow fields were then used for the calculation of the particle trajectories in the flow field using the numerical results of the restitution coefficients obtained by the ABAQUS® software.

6.2 Flow Field Analysis

A typical solid model of IPS was prepared in IGES format and was imported as a volume into GAMBIT® mesh generator (Figure 6-1). The model was a 72^{o} slice of the whole IPS system, which included the inlet ducts and vanes, core section, the scavenge ducts and sane

Separators. Importing solid volumes from one software to another introduces tolerances and torsions of the surfaces and edges. Because of complexity of scavenge area with none-uniform surfaces, complete model was constructed again in GAMBIT® by using the guide lines of the imported solid.

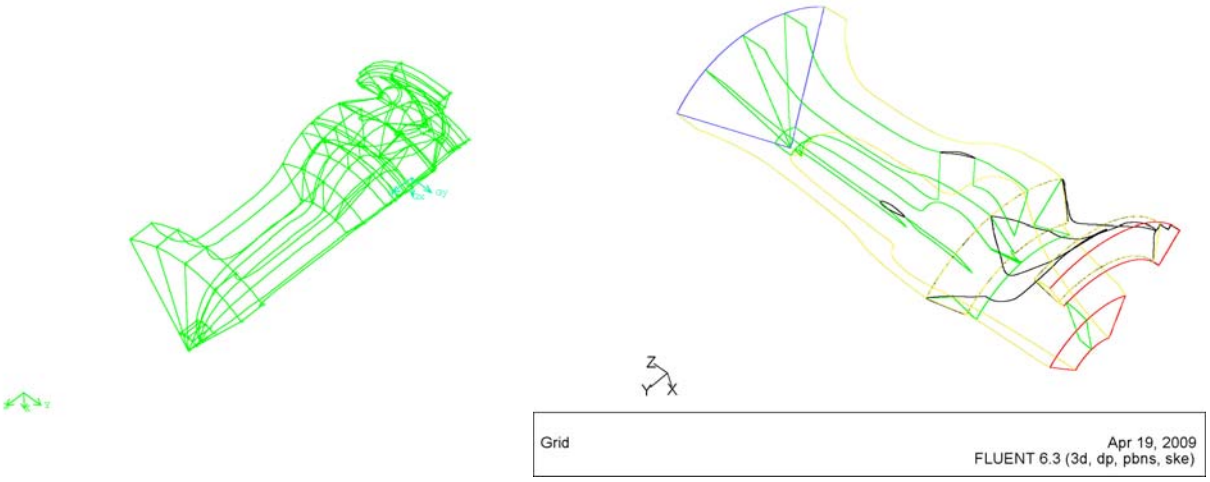

(a) (b)

Figure 6-1 Schematic diagram of inertia particle separator model

The created model then divided into 18 sub-volumes to get finer meshes in complex areas (Figure 6-2).

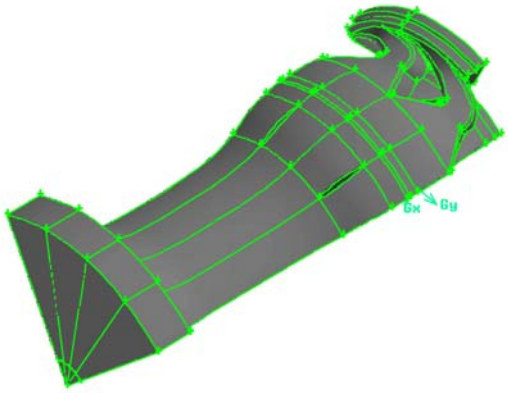

Figure 6-2 Volume descritization for hexagonal meshing

Because of complexity of flow and size of the model, in this study hexagonal grid was chosen for mesh generation of the domain (Figure 6-3). Only in scavenge area the "hexacore" scheme was applied to discretize the scavenge domain. 1,100,000 elements were created to mesh the IPS system in real scale model.

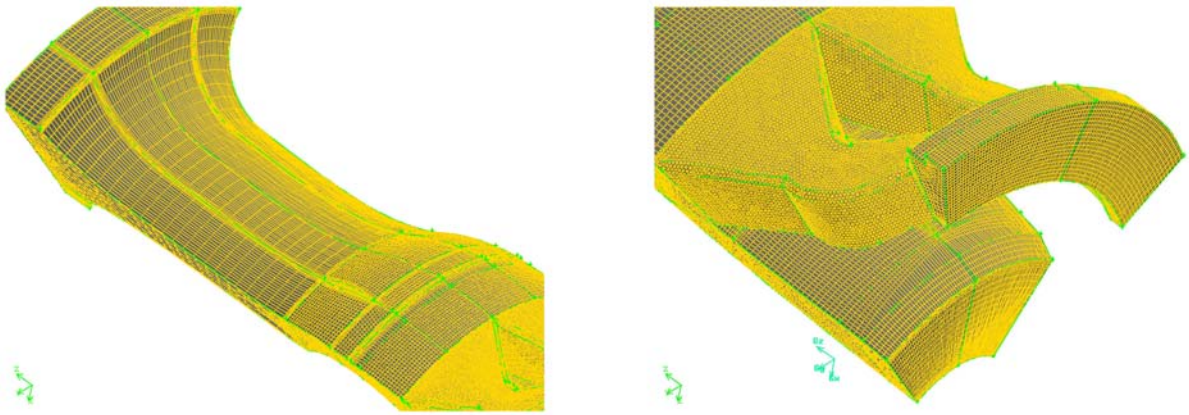

(a) (b)

Figure 6-4 Final meshed model

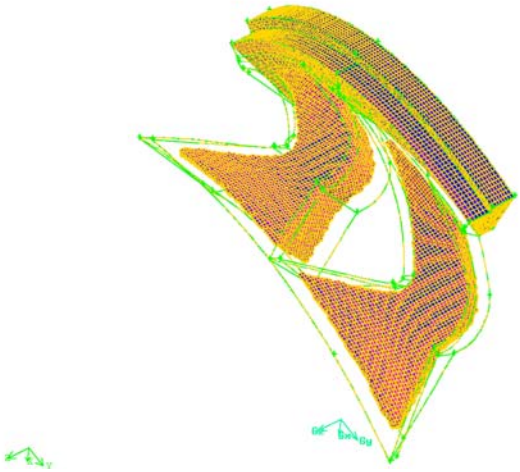

Figure 6-5 "Hexacore" meshing scheme used for scavenges' ducts

For boundary conditions, a constant mass flow of 2.40 lb/sec was set for the inlet of IPS and outflow of 80% and 20% were assumed for the core and scavenge exits. The side-cut planes at +/- 36^{o} were set as non-conformal periodic zones with 72^{o} of rotation. Incompressible air with standard $k-\varepsilon$ turbulence model was used. The convergency criteria were set to 1.00E-5 and the

solution was converged after about 400 iterations. Below these convergency criteria, the numerical solutions started to oscillate because of the grid sizes and the round-off error problem. Figure 6-6 and Figure 6-7 demonstrate the flow field velocity and pressures contour. Results presented a decent high velocity of air flow in IPS especially in the Core section. However the maximum velocities in sand particle separation area before scavenge ducts were 35m/sec slower than that in the core area. These data were the base of choosing nominal velocities in modeling the sand particle impact in ABAQUS®. Similarity of periodic planes in Figure 6-7 was the test case of convergency of numerical solution.

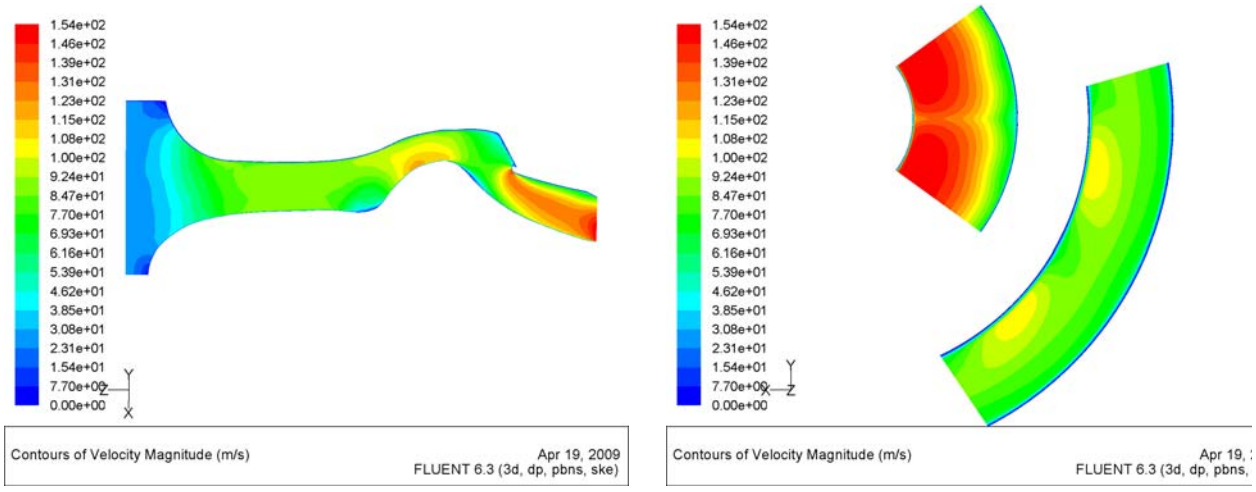

(a) (b)

Figure 6-6 Velocity contours
(a) Periodic plane (b) Core and scavenge exit

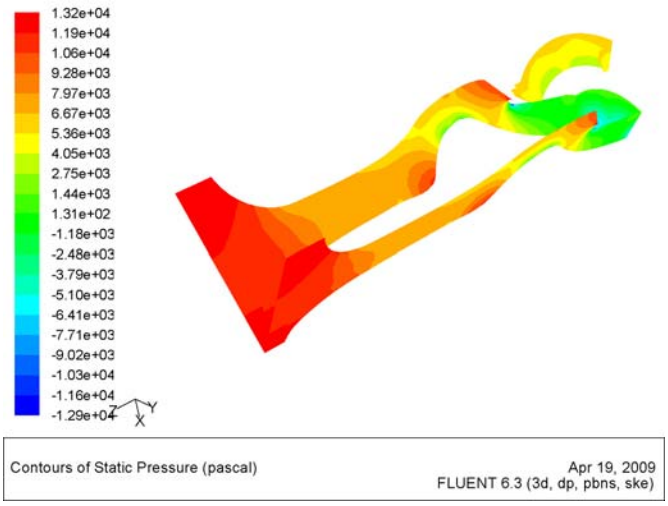

Figure 6-7 Pressure contours on boundary planes

6.3 Particle Trajectory Analysis

Study of particle trajectories in the flow required complete understanding of particle – flow interaction. Newton's second law is applicable to the moving particle in the flow and can be written as:

$$\frac{du_p}{dt} = F_D(u - u_p) + \frac{g_x(\rho_p - \rho)}{\rho_p} + F_x \qquad (6\text{-}1)$$

Equation 6-1 is completely compatible the Eqs. 2-1 and 2-2. By knowing the flow field and particle characteristics, the acceleration of particle at each time iteration will be known and with the initial known position, the particle path can be calculated. Fluent® uses the same concept to find the particle trajectory in the domain by knowing the flow field parameters. Figure 6-8 present a sample 100 mm sand particle trajectory in the flow. The trajectory path demonstrates that for one particle to go through the scavenge section six wall-particle impact can occur. These numbers of collisions if calculated in practical problem, present a considerable amount of momentum transfer from the flow to the IPS walls which can be a source of pressure drop in the system.

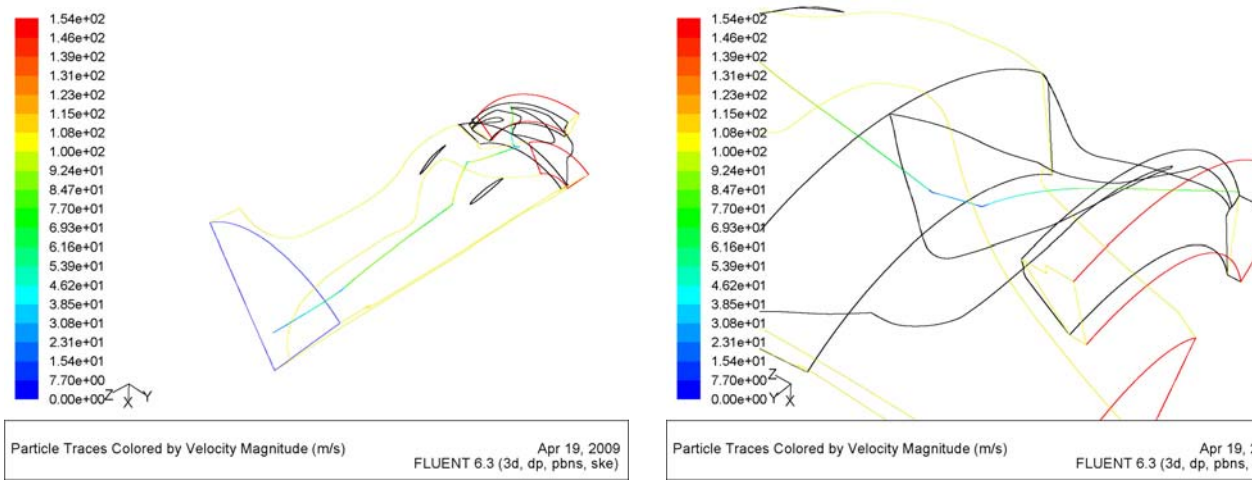

(a) (b)

Figure 6-8 Sample 100 μm particle trajectory

In this research 1,800 particles virtually injected from the inlet plane by a uniform distribution into the numerical domain of IPS model and their trajectories were studied over the time. For collision parameters and restitution coefficients, different models were applied by using the User Defined Functions (UDF) in Fluent® (Code C.1). Particle sizes were chosen from sand particle distribution standards. Number of particles escaped from each of the boundaries then recorded and the results were presented in Table E.1 and Figure 6-9.

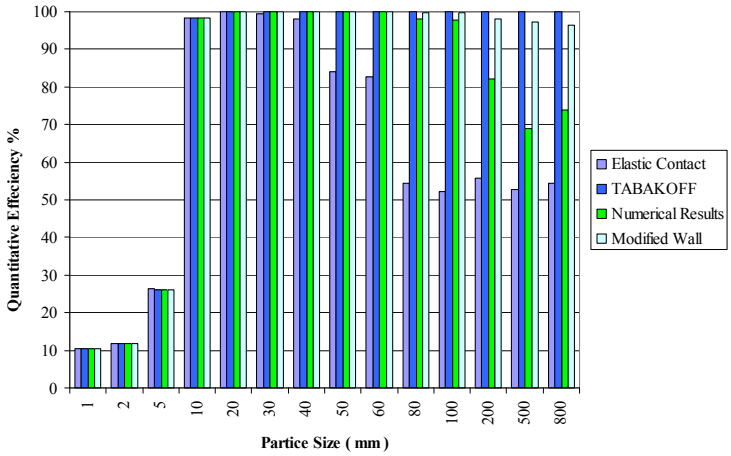

Figure 6-9 IPS Quantitative efficiency for each particle diameter

Results show completely different behavior for different models in predicting the digested sand particles in the IPS. Practically, the IPS design based on the TABAKOFF empirical equations, which in-field results of vehicles, demonstrated a very high over-prediction of the efficiency. On the other hand, the worst scenario of fully elastic collision underestimates the efficiency, which could cost engine failure. For all models, the results revealed that the efficiency of IPS was not dependent on particle sizes of less than 10 μm. The reason of this independence is the dominancy of viscous to inertial forces for small micro particles. For sizes less than 10 μm, the particles completely follow the streamlines of the flow and probability of wall-particle impact drastically drops.

6.4 Results and Discussion

In the current work, the physics of wall-particle impact have been investigated both numerically and experimentally. The results show a strong dependency of normal restitution coefficients on impact velocity and a strong dependency of tangential restitution coefficients on colliding particle size. Still the precision errors of the experimental results are relatively high and require more calibration of the shooting system for high speed particles. However, the trend line of all experimental data agreed with the numerical results from ABAQUS® and with the experimental results presented in open literature by others.

The numerical flow field solutions of IPS, on the other hand was in very good agreement with experimental data and numerical results of the CFX® Software. For particle trajectory studies, four different cases were considered in modeling: Completely elastic collision, Tabakoff ‘s empirical correlations, calibrated numerical correlations obtained by numerical simulations, and modified wall impact correlations. Fully elastic collision and Tabakoff’s model of wall-particle collision are two known cases in modeling at the IPS system which their prediction have

controversy with experimental results. The efficiency analysis of IPS with numerical results of restitution coefficients are in good agreement with in-field results of IPS efficiencies. Figure 6-10 and Figure 6-11 present the results of quantitative and mass efficiencies of a typical IPS obtained from Table E.1. The quantitative efficiency is base on the number of particles that extracted from the flow and sent to the scavenge section regardless of their mass. It revealed that both of these efficiencies are required for optimization of IPS system. For example, based on ACF Standards, the mass efficiency of IPS even with numerical restitution coefficient results is about 97% while the number of particles separated by the scavenge system is less than 65%. This discrepancy stemmed from the lightness of small particle in comparison with larger particles. This erroneous may cost an engine if prober sand separation systems are not installed. In the last step of this study, a new design was proposed to increase the efficiency of IPS system by modifying the upper-internal wall materials of the IPS in order to have smaller normal restitution coefficients. Using materials that can damp most of the kinetic energy of the particles, the rebound particle will stay near the upper wall and will be swiped out by the scavenge flow. The model of this modified wall IPS was tested numerically by Fluent® and results are shown in Table E.1 and Figure 6-10 and Figure 6-11. A drastically increasing of efficiency of more than 10% observed in C Spec standard.

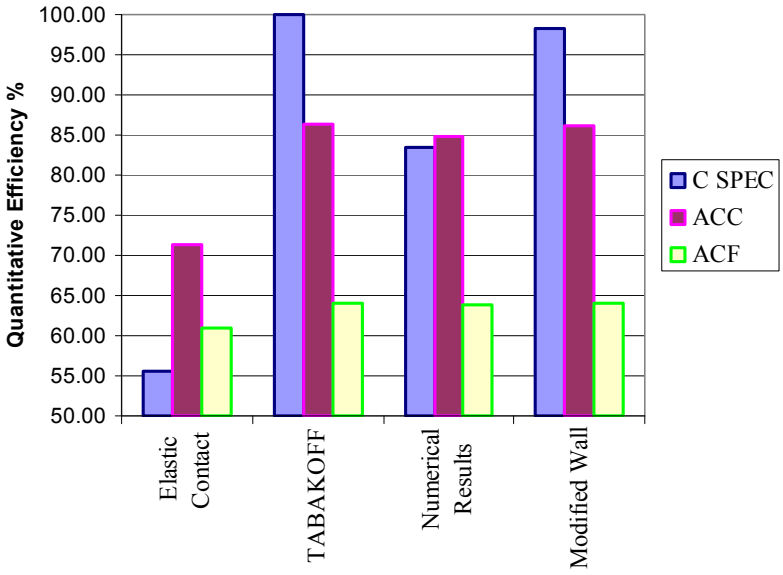

Figure 6-10 Total IPS quantitative efficiency

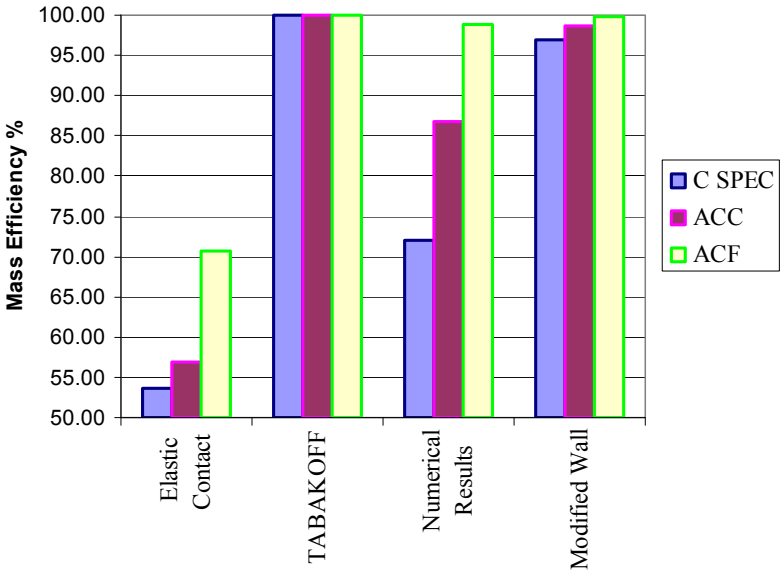

Figure 6-11 Total IPS mass efficiency

CHAPTER 7 APPENDICES

7.1 TABLES

Table A.1: Beaufort Scales (Wind Speed)

Force	Speed Km/hr	Name	Conditions at Sea	Conditions on Land
0	< 2	Calm	Sea like a mirror.	Smoke rises vertically.
1	1-5	Light air	Ripples only.	Smoke drifts and leaves rustle.
2	6-11	Light breeze	Small wavelets (0.2 m). Crests have a glassy appearance.	Wind felt on face.
3	12-19	Gentle breeze	Large wavelets (0.6 m), crests begin to break.	Flags extended, leaves move.
4	20-29	Moderate breeze	Small waves (1 m), some whitecaps.	Dust and small branches move.
5	30-39	Fresh breeze	Moderate waves (1.8 m), many whitecaps.	Small trees begin to sway.
6	40-50	Strong breeze	Large waves (3 m), probably some spray.	Large branches move, wires whistle, umbrellas are difficult to control.
7	51-61	Near gale	Mounting sea (4 m) with foam blown in streaks downwind.	Whole trees in motion, inconvenience in walking.
8	62-74	Gale	Moderately high waves (5.5 m), crests break into spindrift.	Difficult to walk against wind. Twigs and small branches blown off trees.
9	76-87	Strong gale	High waves (7 m), dense foam, visibility affected.	Minor structural damage may occur (shingles blown off roofs).
10	88-102	Storm	Very high waves (9 m), heavy sea roll, visibility impaired. Surface generally white.	Trees uprooted, structural damage likely.
11	103-118	Violent storm	Exceptionally high waves (11 m), visibility poor.	Widespread damage to structures.
12	119+	Hurricane	14 m waves, air filled with foam and spray, visibility bad.	Severe structural damage to buildings, wide spread devastation.

Table B.1: Honeywell SDP8314-301 Datasheet

Product Specification	
Product Type	IR Component
Angular Response (Degree)	50
Turn-on Threshold Irradiance	0.37 mW/cm² maximum
Output	Open-Collector
Output Logic	Inverter
Package Style	Side-Looking
Package Components	Plastic
Package Color	Black
Operating Temperature Range	-40 °C to 85 °C [-40 °F to 185 °F]
Hysteresis (H)	33% to 67%
Operating Supply Voltage	4.5 V to 12.0 V
Supply Voltage	12.0 Vdc
High Level Output Current	100 μA maximum
Low Level Output Voltage	0.4 V maximum
Low Level Output Current	16 mA
Applied Output Voltage	35 V
Operating Point Temperature Coefficient	-0.76 %/°C
Output Rise Time	7.0 ns
Output Fall Time	7.0 ns
Propagation Delay, Low-High, High-Low	5.0 μs
Clock Frequency	100 kHz
Duration of Output Short Vcc or Ground	1.0 second
Irradiance	25 mW/cm²
Comment	Output is LO when incident light intensity is above the turn-on threshold level.
Availability	Global
Product Name	Optoschmitt Detector
Supply Current max.	15 mA @ 25 °C

Table C.1: Direct Compressed Air Shooting – Summary of Results

Angle	Pressure	Experiment	Inbound Vel.	Inbound Angle	Outbound Angle	$ß_2/ß_1$	RCFN	RCFT
(Deg.)	(Psi)		(mm/sec)	(Deg.)	(Deg.)			
15.0	**20**	**1**	31,449	13.0	11.2	0.861	0.803	0.937
		2	32,889	13.7	11.8	0.861	0.812	0.948
		3	29,685	12.8	10.5	0.820	0.755	0.926
		4	30,457	13.8	10.1	0.728	0.688	0.953
	40	**1**	35,604	13.5	10.6	0.782	0.733	0.944
		2	38,234	14.3	10.9	0.757	0.697	0.929
		3	36,876	14.0	11.4	0.816	0.788	0.973
		4	35,364	14.4	11.0	0.766	0.723	0.953
	60	**1**	40,198	13.7	1.3	0.091	0.088	0.982
		2	42,604	14.4	16.1	1.116	0.997	0.888
		3	44,302	13.6	6.5	0.480	0.450	0.951
		4	44,505	15.5	12.3	0.797	0.732	0.926
	80	**1**	47,789	14.8	11.5	0.779	0.732	0.948
		2	47,623	14.1	16.2	1.143	0.997	0.866
		3	47,480	13.7	11.6	0.846	0.793	0.943
		4	42,687	15.2	19.5	1.283	1.155	0.886
	100	**1**	46,828	13.8	10.3	0.745	0.702	0.950
		2	50,555	16.6	12.4	0.745	0.698	0.950
		3	45,005	16.8	13.6	0.808	0.734	0.917
		4	45,031	14.7	16.2	1.097	0.996	0.903

Table C.2: Direct Compressed Air Shooting – Summary of Results

Angle	Pressure	Experiment	Inbound Vel.	Inbound Angle	Outbound Angle	$ß_2/ß_1$	RCFN	RCFT
(Deg.)	(Psi)		(mm/sec)	(Deg.)	(Deg.)			
22.5	**20**	**1**	31,394	21.6	15.8	0.730	0.665	0.933
		2	27,325	24.6	16.8	0.684	0.571	0.864
		3	31,729	20.1	12.0	0.596	0.550	0.949
		4	27,631	18.3	14.8	0.810	0.719	0.898
	40	**1**	34,725	20.8	15.4	0.742	0.687	0.946
		2	32,828	22.2	14.5	0.653	0.579	0.913
		3	41,406	22.3	16.7	0.748	0.678	0.927
		4	32,327	21.1	14.6	0.693	0.627	0.927
	60	**1**	38,467	22.2	16.9	0.762	0.687	0.922
		2	40,714	21.7	13.7	0.632	0.595	0.970
		3	39,577	21.7	19.4	0.897	0.715	0.805
		4	38,415	20.9	11.8	0.564	0.509	0.932
	80	**1**	46,402	21.2	14.9	0.704	0.656	0.953
		2	41,960	22.3	14.8	0.662	0.603	0.939
		3	44,279	21.1	17.3	0.823	0.699	0.862
		4	40,097	22.0	15.4	0.703	0.641	0.936
	100	**1**	47,557	21.5	15.4	0.720	0.639	0.908
		2	47,726	21.6	14.2	0.659	0.592	0.924
		3	47,272	20.2	14.8	0.733	0.661	0.921
		4	48,229	22.2	15.7	0.707	0.626	0.910

Table C.3: Direct Compressed Air Shooting – Summary of Results

Angle	Pressure	Experiment	Inbound Vel.	Inbound Angle	Outbound Angle	$ß_2/ß_1$	RCFN	RCFT
(Deg.)	(Psi)		(mm/sec)	(Deg.)	(Deg.)			
45.0	**20**	**1**	30,168	44.3	36.0	0.814	0.535	0.717
		2	28,093	42.4	30.1	0.709	0.511	0.807
		3	26,812	44.2	35.4	0.800	0.523	0.716
		4	26,303	44.1	32.1	0.726	0.558	0.864
	40	**1**	35,384	44.2	29.9	0.675	0.484	0.821
		2	35,481	44.1	26.1	0.593	0.441	0.870
		3	36,308	44.1	14.5	0.330	0.279	1.039
		4	32,376	43.7	23.5	0.538	0.386	0.847
	60	**1**	39,274	43.8	30.3	0.691	0.489	0.803
		2	38,261	45.0	32.9	0.731	0.516	0.798
		3	41,308	43.6	29.1	0.667	0.476	0.816
		4	31,358	44.2	32.5	0.735	0.500	0.764
	80	**1**	43,040	43.9	36.5	0.832	0.529	0.688
		2	42,937	44.6	31.8	0.713	0.498	0.792
		3	44,701	46.1	31.9	0.691	0.456	0.762
		4	42,384	45.7	32.1	0.701	0.480	0.786
	100	**1**	45,020	44.9	29.6	0.661	0.466	0.815
		2	47,156	45.2	29.6	0.656	0.473	0.837
		3	48,457	45.0	30.7	0.683	0.459	0.772
		4	45,079	43.1	26.4	0.612	0.458	0.864

Table C.4: Direct Compressed Air Shooting – Summary of Results

Angle	Pressure	Experiment	Inbound Vel.	Inbound Angle	Outbound Angle	$ß_2/ß_1$	RCFN	RCFT
(Deg.)	(Psi)		(mm/sec)	(Deg.)	(Deg.)			
67.5	**20**	**1**	29,155	67.5	61.3	0.907	0.437	0.580
		2	29,163	65.9	40.8	0.619	0.340	0.880
		3	30,212	66.8	46.2	0.691	0.394	0.881
		4	29,021	64.9	50.6	0.780	0.452	0.793
	40	**1**	37,918	65.4	43.1	0.660	0.393	0.915
		2	36,741	66.0	43.5	0.658	0.382	0.908
		3	34,707	67.3	56.3	0.837	0.431	0.686
		4	36,076	66.1	59.7	0.903	0.496	0.654
	60	**1**	41,034	67.8	50.7	0.748	0.384	0.770
		2	41,917	67.3	57.9	0.860	0.406	0.610
		3	36,338	68.6	57.4	0.837	0.412	0.671
		4	38,619	68.6	55.4	0.808	0.414	0.728
	80	**1**	42,748	67.4	51.1	0.758	0.382	0.741
		2	44,467	65.7	48.5	0.738	0.358	0.703
		3	45,322	67.0	55.7	0.831	0.376	0.605
		4	41,752	65.9	46.8	0.709	0.352	0.740
	100	**1**	45,383	69.0	54.0	0.783	0.378	0.713
		2	26,446	66.4	51.8	0.781	0.409	0.736
		3	45,089	67.8	70.7	1.042	0.416	0.358
		4	46,177	66.1	47.1	0.713	0.380	0.795

Table C.5: Direct Compressed Air Shooting – Summary of Results

Angle	Pressure	Experiment	Inbound Vel.	Inbound Angle	Outbound Angle	$ß_2/ß_1$	RCFN	RCFT
(Deg.)	(Psi)		(mm/sec)	(Deg.)	(Deg.)			
90.0	**20**	**1**	26,758	89.7	89.4	0.997	0.449	0.884
		2	28,974	89.2	87.4	0.980	0.441	1.502
		3	29,459	87.3	87.3	1.000	0.424	0.424
		4	22,132	88.9	85.6	0.963	0.566	2.174
	40	**1**	37,518	89.0	80.8	0.908	0.385	3.475
		2	35,706	88.9	87.1	0.979	0.396	1.056
		3	36,613	88.6	87.2	0.983	0.342	0.712
		4	33,875	90.9	-91.0	-1.000	-0.410	0.426
	60	**1**	37,347	89.9	87.9	0.978	0.396	6.347
		2	40,089	88.3	87.3	0.988	0.382	0.628
		3	42,364	89.8	92.0	1.024	0.392	-4.539
		4	42,412	89.9	87.9	0.978	0.388	6.357
	80	**1**	31,045	89.1	78.5	0.881	0.522	6.937
		2	42,847	88.1	82.9	0.941	0.388	1.429
		3	42,335	88.4	87.7	0.991	0.418	0.621
		4	44,107	88.1	-88.5	-1.005	-0.358	0.273
	100	**1**	42,717	89.4	86.7	0.970	0.388	2.113
		2	42,643	89.8	89.5	0.997	0.395	0.996
		3	42,748	89.3	89.1	0.998	0.378	0.459
		4	44,746	89.1	85.8	0.963	0.386	1.841

Table D.1: Viscous Driven Shooting – Summary of Results

Angle (Deg.)	Pressure (Psi)	Experiment	Inbound Vel. (mm/sec)	Inbound Angle (Deg.)	Outbound Angle (Deg.)	$ß_2/ß_1$	RCFN	RCFT
22.5	**0**	**1**	6,899	21.8	19.9	0.910	0.840	0.931
		2	6,939	21.9	16.5	0.754	0.687	0.932
		3	7,311	22.2	18.0	0.809	0.731	0.920
		4	6,970	22.3	17.2	0.770	0.713	0.946
	5	**1**	9,267	22.4	17.9	0.798	0.723	0.924
		2	9,228	23.4	18.2	0.776	0.709	0.935
		3	9,487	22.3	14.6	0.654	0.608	0.958
		4	9,019	21.8	18.3	0.841	0.763	0.920
	10	**1**	12,868	20.3	17.3	0.852	0.760	0.903
		2	13,070	22.2	17.6	0.791	0.725	0.934
		3	12,971	21.3	18.3	0.858	0.763	0.901
		4	12,283	22.2	13.1	0.590	0.554	0.972
	15	**1**	17,540	23.0	16.1	0.699	0.632	0.932
		2	17,545	22.3	17.1	0.766	0.710	0.948
		3	14,746	22.7	17.0	0.748	0.665	0.911
		4	17,342	22.8	16.9	0.738	0.653	0.907
	20	**1**	20,476	22.1	18.1	0.819	0.754	0.937
		2	16,990	22.2	17.2	0.772	0.703	0.931
		3	18,524	22.5	16.1	0.715	0.633	0.909
		4	17,858	22.6	16.7	0.738	0.672	0.933

Table D.2: Viscous Driven Shooting – Summary of Results

Angle	Pressure	Experiment	Inbound Vel.	Inbound Angle	Outbound Angle	$ß_2/ß_1$	RCFN	RCFT
(Deg.)	(Psi)		(mm/sec)	(Deg.)	(Deg.)			
45.0	**0**	**1**	7,182	44.6	37.0	0.829	0.645	0.846
		2	7,163	45.7	39.4	0.862	0.644	0.805
		3	6,843	45.6	39.5	0.866	0.651	0.806
		4	6,797	45.5	39.6	0.870	0.659	0.811
	5	**1**	10,330	45.6	39.7	0.870	0.630	0.776
		2	9,754	44.2	38.7	0.876	0.633	0.768
		3	9,994	45.5	36.5	0.802	0.629	0.865
		4	9,682	45.7	37.5	0.820	0.624	0.834
	10	**1**	10,129	45.3	37.6	0.829	0.631	0.830
		2	12,480	45.3	35.0	0.772	0.579	0.837
		3	13,750	46.4	35.5	0.764	0.565	0.833
		4	12,129	46.0	34.5	0.750	0.555	0.836
	15	**1**	12,657	45.5	34.9	0.767	0.583	0.850
		2	15,622	45.5	33.4	0.733	0.536	0.829
		3	17,050	45.5	33.5	0.735	0.544	0.838
		4	14,070	45.7	30.5	0.668	0.616	1.070
	20	**1**	28,087	38.2	33.4	0.874	0.600	0.717
		2	16,815	48.6	37.9	0.781	0.533	0.775
		3	16,538	45.7	36.4	0.797	0.537	0.746
		4	17,023	46.7	34.9	0.747	0.538	0.818

Table D.3: Viscous Driven Shooting – Summary of Results

Angle (Deg.)	Pressure (Psi)	Experiment	Inbound Vel. (mm/sec)	Inbound Angle (Deg.)	Outbound Angle (Deg.)	$ß_2/ß_1$	RCFN	RCFT
67.5	**0**	**1**	7,020	67.1	66.0	0.985	0.643	0.675
		2	7,175	67.4	67.7	1.004	0.610	0.602
		3	6,820	66.9	66.2	0.989	0.614	0.635
		4	7,276	67.3	66.7	0.991	0.615	0.634
	5	**1**	9,310	67.8	67.3	0.993	0.646	0.662
		2	10,200	67.8	71.5	1.054	0.574	0.471
		3	9,483	67.7	66.8	0.986	0.579	0.606
		4	9,520	67.3	66.9	0.994	0.583	0.594
	10	**1**	14,037	67.5	65.3	0.968	0.548	0.608
		2	13,740	67.6	66.3	0.981	0.546	0.581
		3	13,558	68.7	64.4	0.937	0.534	0.656
		4	12,947	67.1	63.2	0.942	0.538	0.643
	15	**1**	17,059	67.6	64.8	0.959	0.519	0.592
		2	16,943	67.5	64.6	0.958	0.508	0.581
		3	16,123	68.2	62.8	0.922	0.527	0.676
		4	15,847	66.9	63.2	0.944	0.517	0.614
	20	**1**	18,289	67.8	60.9	0.898	0.487	0.665
		2	20,943	68.2	62.6	0.918	0.492	0.638
		3	18,958	69.0	65.0	0.942	0.518	0.629
		4	18,345	68.7	64.4	0.937	0.514	0.631

Table D.4: Viscous Driven Shooting – Summary of Results

Angle	Pressure	Experiment	Inbound Vel.	Inbound Angle	Outbound Angle	$ß_2/ß_1$	RCFN	RCFT
(Deg.)	(Psi)		(mm/sec)	(Deg.)	(Deg.)			
90.0	**0**	**1**	7,452	88.6	89.8	1.013	0.611	0.090
		2	6,775	89.6	89.9	1.003	0.604	0.176
		3	6,775	89.6	85.0	0.949	0.605	7.001
		4	6,729	89.5	88.6	0.990	0.608	1.609
	5	**1**	9,385	90.0	89.9	1.000	0.533	1.050
		2	9,414	88.7	89.7	1.011	0.575	0.132
		3	10,084	89.4	88.9	0.995	0.572	0.985
		4	9,458	90.7	91.4	1.008	0.601	1.202
	10	**1**	12,698	89.6	83.6	0.933	0.497	7.433
		2	12,003	88.3	91.2	1.033	0.511	-0.350
		3	12,378	89.3	88.4	0.991	0.537	1.137
		4	11,870	87.5	90.4	1.033	0.544	-0.086
	15	**1**	16,404	89.0	89.9	1.010	0.507	0.059
		2	16,802	89.0	78.4	0.881	0.525	6.131
		3	16,445	89.9	87.7	0.976	0.414	14.610
		4	13,579	89.5	75.3	0.841	0.375	11.166
	20	**1**	16,264	89.8	89.4	0.996	0.505	1.202
		2	18,926	88.0	90.6	1.029	0.511	-0.162
		3	19,132	90.0	83.5	0.928	0.548	186.669
		4	17,937	88.0	90.5	1.029	0.494	-0.130

Table E.1: Indirect Compressed Air Shooting – Summary of Results

	RCFN											
	22.5 Deg			45.0 Deg			62.5 Deg			90.0 Deg		
	Angle	e_N	Velocity	Angle	e_N	Velocity	Angle	e_N	Velocity	Angle	e_N	Velocity
	24.616	0.418	65.366	42.855	0.511	64.423	75.521	0.294	70.580	88.900	0.282	70.925
	25.047	0.657	64.998	44.469	0.414	69.552	76.102	0.275	67.881	89.502	0.261	70.936
	23.884	0.749	66.503	44.360	0.469	66.658	76.581	0.232	69.386	89.380	0.281	69.552
	27.320	0.504	70.669	46.974	0.414	72.127	75.328	0.263	70.200	89.631	0.279	71.813
	25.244	0.648	69.572	45.572	0.426	72.566	77.949	0.243	66.815	89.974	0.265	72.117
Ave.	25.222	0.595	67.422	44.846	0.447	69.065	76.296	0.261	68.972	89.478	0.274	71.069
STD	1.284	0.132	2.555	1.533	0.042	3.508	1.047	0.025	1.589	0.392	0.010	0.999
Error +	2.736	0.282	5.447	3.268	0.090	7.478	2.233	0.053	3.389	0.835	0.021	2.129
Error -	-2.736	-0.282	-5.447	-3.268	-0.090	-7.478	-2.233	-0.053	-3.389	-0.835	-0.021	-2.129
Min	22.486	0.314	61.974	41.578	0.357	61.587	74.063	0.208	65.584	88.642	0.253	68.939
Max	27.959	0.877	72.869	48.114	0.537	76.543	78.530	0.315	72.361	90.313	0.294	73.198

	RCFT							
	22.5 Deg		45.0 Deg		62.5 Deg		90.0 Deg	
	Angle	e_T	Angle	e_T	Angle	e_T	Angle	e_T
	24.616	0.985	42.855	0.826	75.521	0.561	88.900	1.000
	25.047	0.886	44.469	0.729	76.102	0.592	89.502	1.000
	23.884	0.878	44.360	0.778	76.581	0.894	89.380	1.000
	27.320	0.888	46.974	0.717	75.328	0.653	89.631	1.000
	25.244	0.869	45.572	0.809	77.949	0.490	89.974	1.000
Ave.	25.222	0.901	44.846	0.772	76.296	0.638	89.478	1.000
STD	1.284	0.047	1.533	0.048	1.047	0.155	0.392	0.000
Error +	2.736	0.101	3.268	0.102	2.233	0.330	0.835	0.000
Error -	-2.736	-0.101	-3.268	-0.102	-2.233	-0.330	-0.835	0.000
Min	22.486	0.800	41.578	0.670	74.063	0.308	88.642	1.000
Max	27.959	1.002	48.114	0.874	78.530	0.968	90.313	1.000

Table F.1: Numerical Results of Scavenge Efficiency Based on 1800 Sample Particles

		Elastic Contact													
		Particle size (mm)													
Surface	Zone ID	**1**	**2**	**5**	**10**	**20**	**30**	**40**	**50**	**60**	**80**	**100**	**200**	**500**	**800**
Scavenge	13	188	213	473	1772	1800	1789	1767	1514	1485	924	766	604	234	236
Core	14	1612	1587	1327	28	0	11	33	286	312	819	859	796	849	822
Inlet	15	0	0	0	0	0	0	0	0	3	57	175	400	717	742
Percentage		10	12	26	98	100	99	98	84	83	55	52	56	53	54
		TABAKOF													
		Particle size (mm)													
Surface	Zone ID	**1**	**2**	**5**	**10**	**20**	**30**	**40**	**50**	**60**	**80**	**100**	**200**	**500**	**800**
Scavenge	13	188	213	471	1772	1800	1800	1800	1800	1800	1799	1797	1622	1476	1348
Core	14	1612	1587	1329	28	0	0	0	0	0	0	0	1	0	1
Inlet	15	0	0	0	0	0	0	0	0	0	1	3	177	324	451
Percentage		10	12	26	98	100	100	100	100	100	100	100	100	100	100
		Numerical Results													
		Particle size (mm)													
Surface	Zone ID	**1**	**2**	**5**	**10**	**20**	**30**	**40**	**50**	**60**	**80**	**100**	**200**	**500**	**800**
Scavenge	13	188	213	472	1772	1800	1800	1800	1800	1798	1760	1673	1154	648	675
Core	14	1612	1587	1328	28	0	0	0	2	2	36	39	319	558	470
Inlet	15	0	0	0	0	0	0	0	0	0	6	88	327	594	655
Percentage		10	12	26	98	100	100	100	100	100	98	98	82	69	74
		Modified Wall													
		Particle size (mm)													
Surface	Zone ID	**1**	**2**	**5**	**10**	**20**	**30**	**40**	**50**	**60**	**80**	**100**	**200**	**500**	**800**
Scavenge	13	188	213	472	1772	1800	1800	1800	1800	1800	1794	1786	1743	1414	1451
Core	14	1612	1587	1328	28	0	0	0	0	0	6	4	33	51	62
Inlet	15	0	0	0	0	0	0	0	0	0	0	10	24	335	287
Percentage		10	12	26	98	100	100	100	100	100	100	100	98	97	97

DATA APPENDICES

7.2 DRAWINGS

Drawing A.1: Viscous Driven Accelerator (Assembly Configuration)

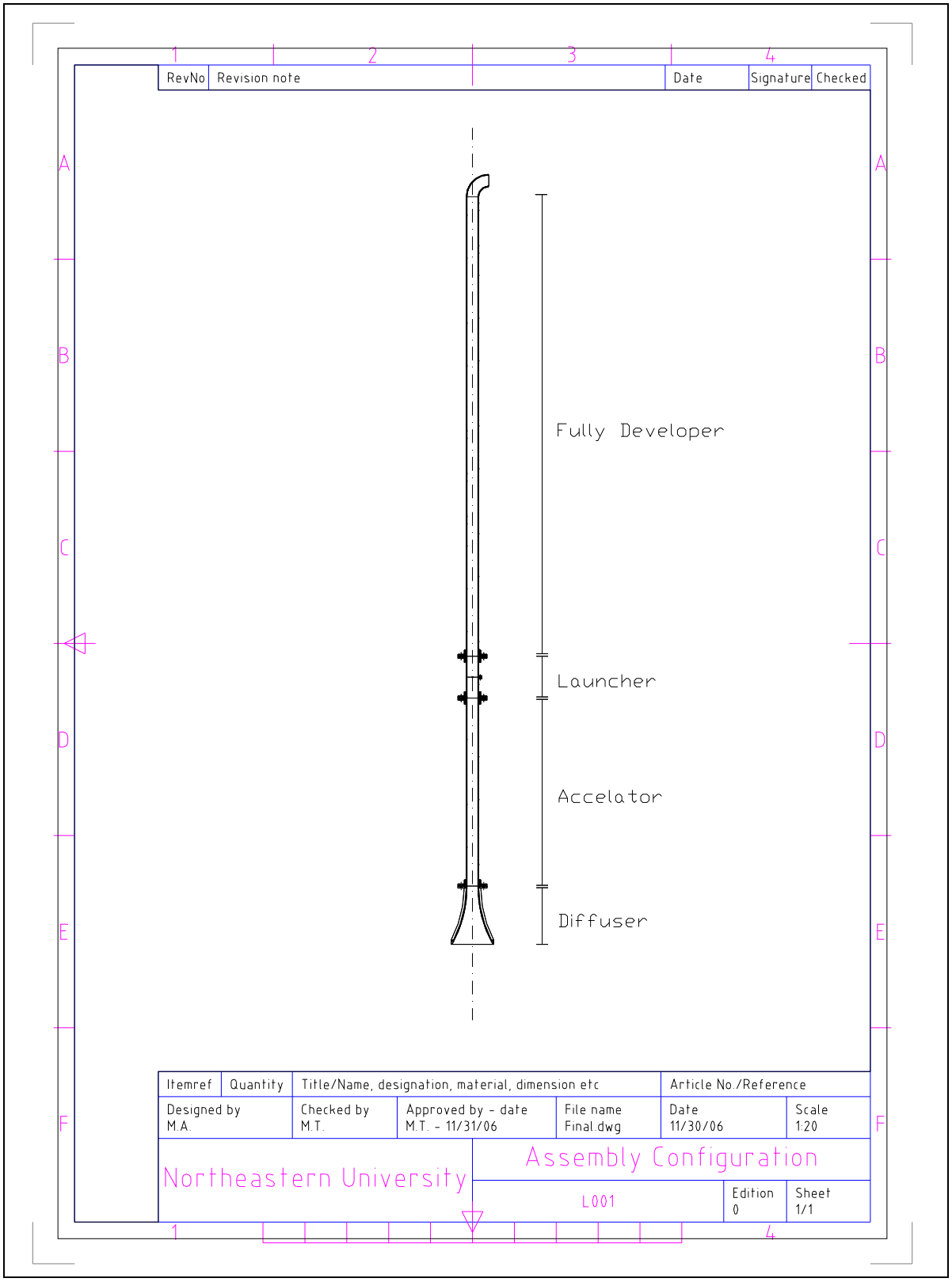

Drawing A.2: Viscous Driven Accelerator (Diffuser Details)

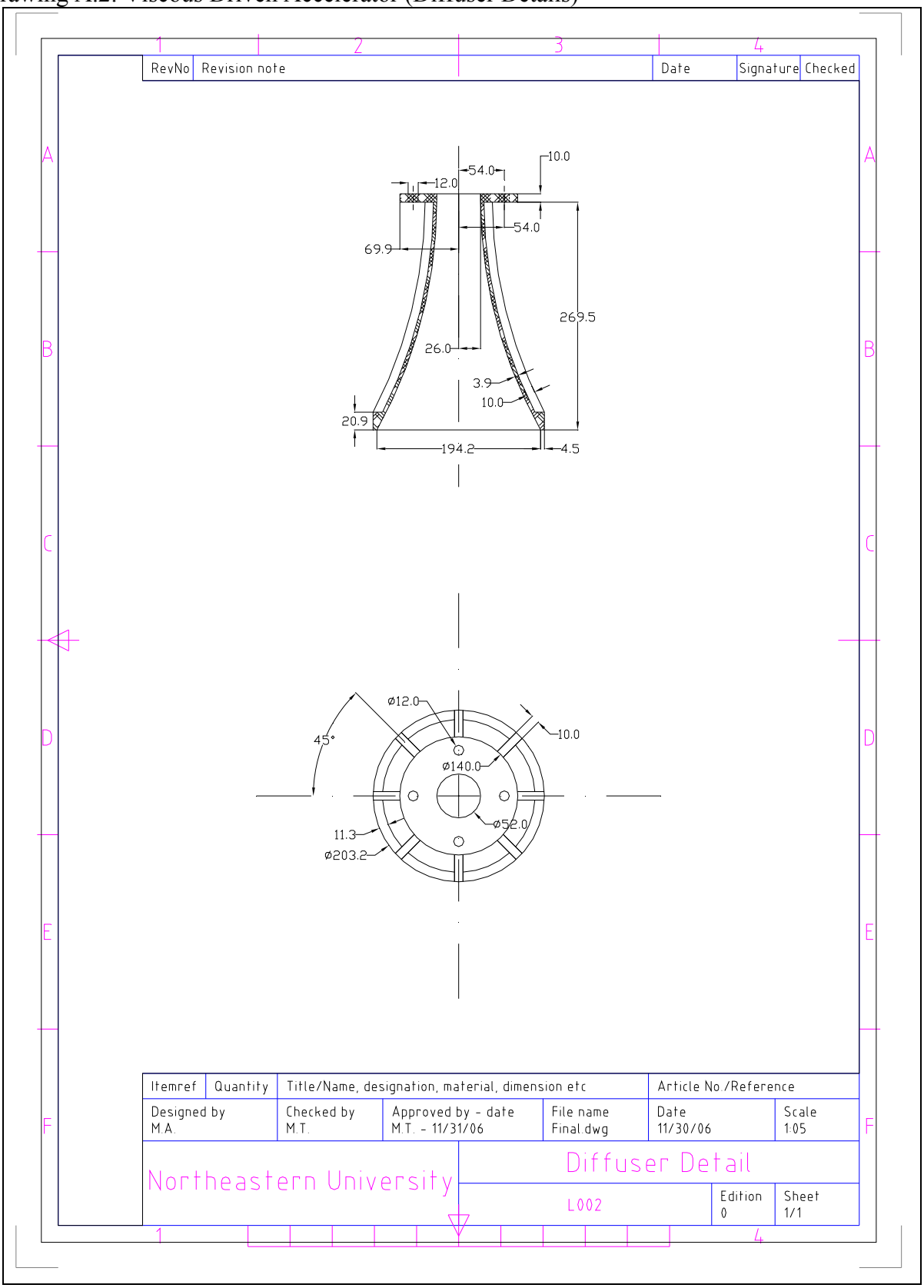

Drawing A.3: Viscous Driven Accelerator (Flange Detail)

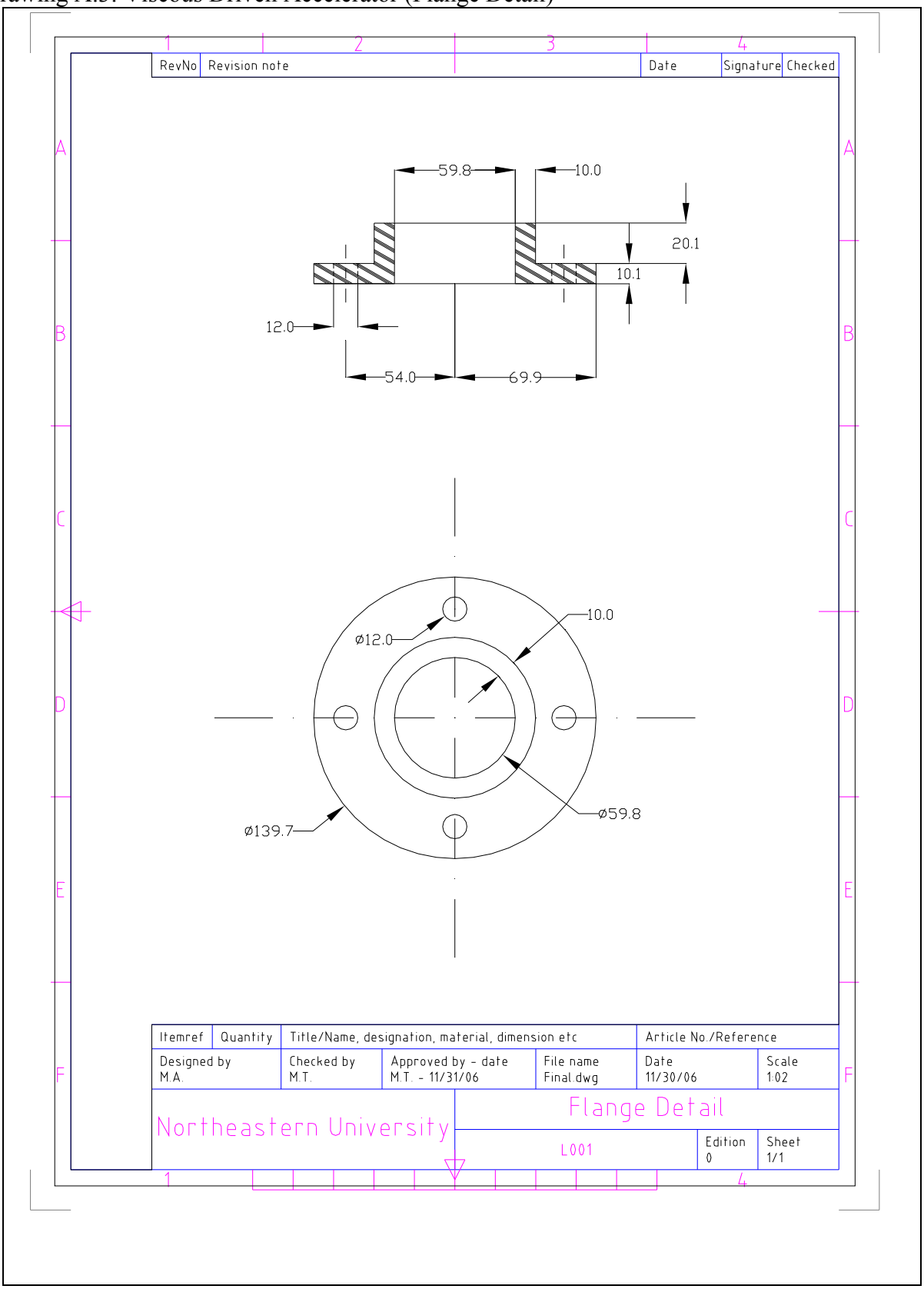

Drawing A.4: Viscous Driven Accelerator (Launcher Section)

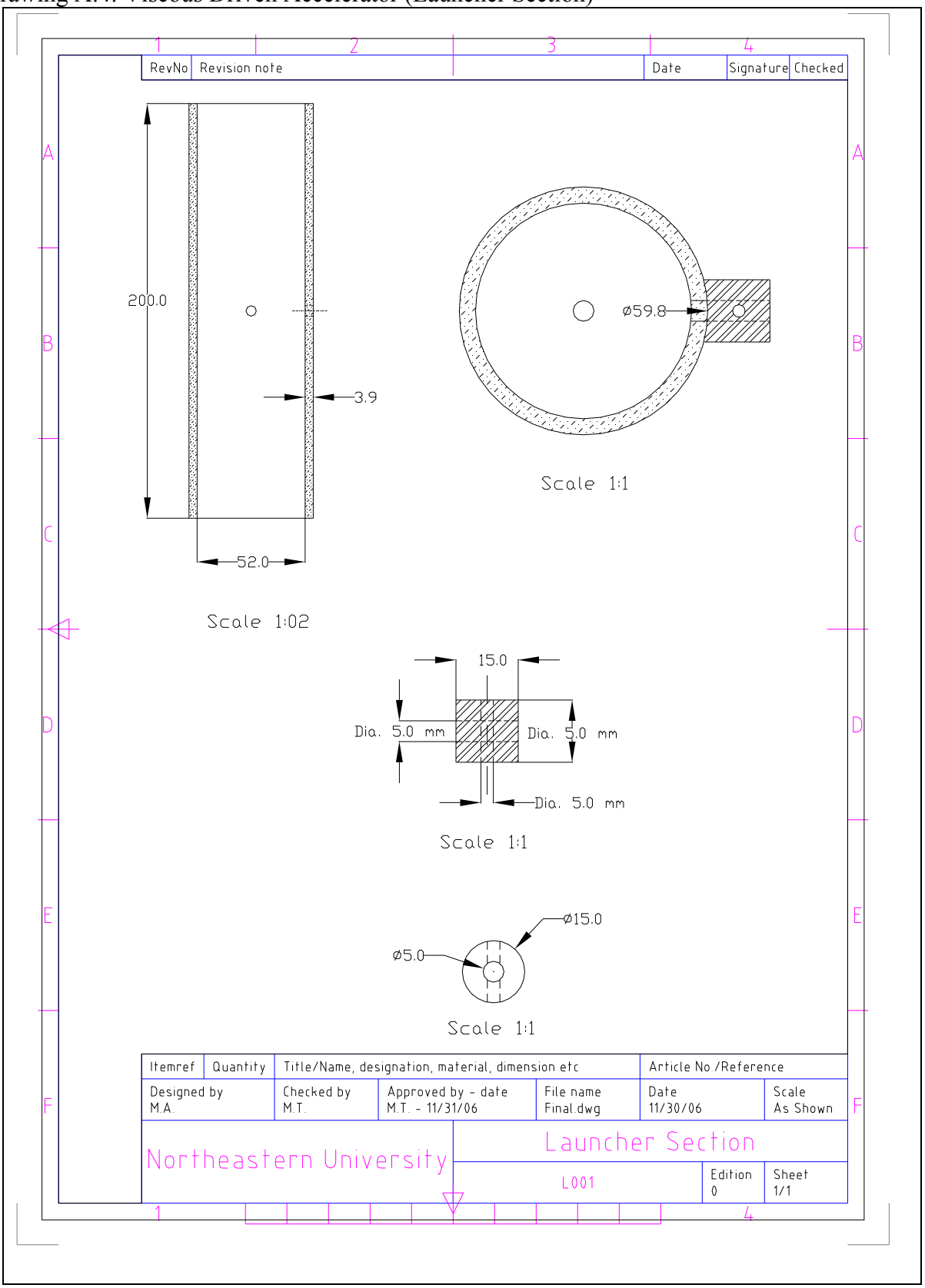

Drawing A.5: Viscous Driven Accelerator (Fully Developer Section)

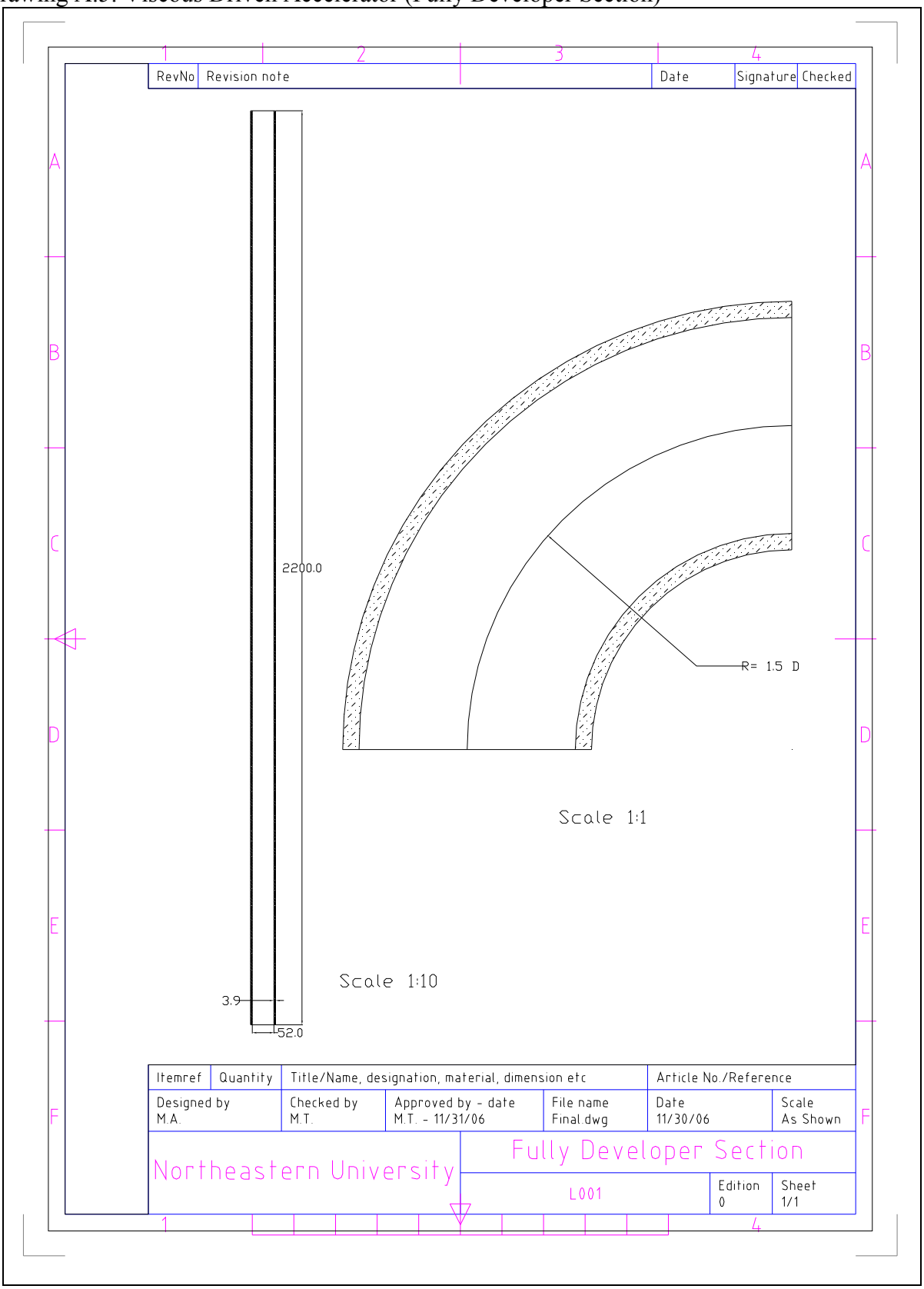

Drawing B.1: Preliminary Design (Launching Setup-General Arrangement)

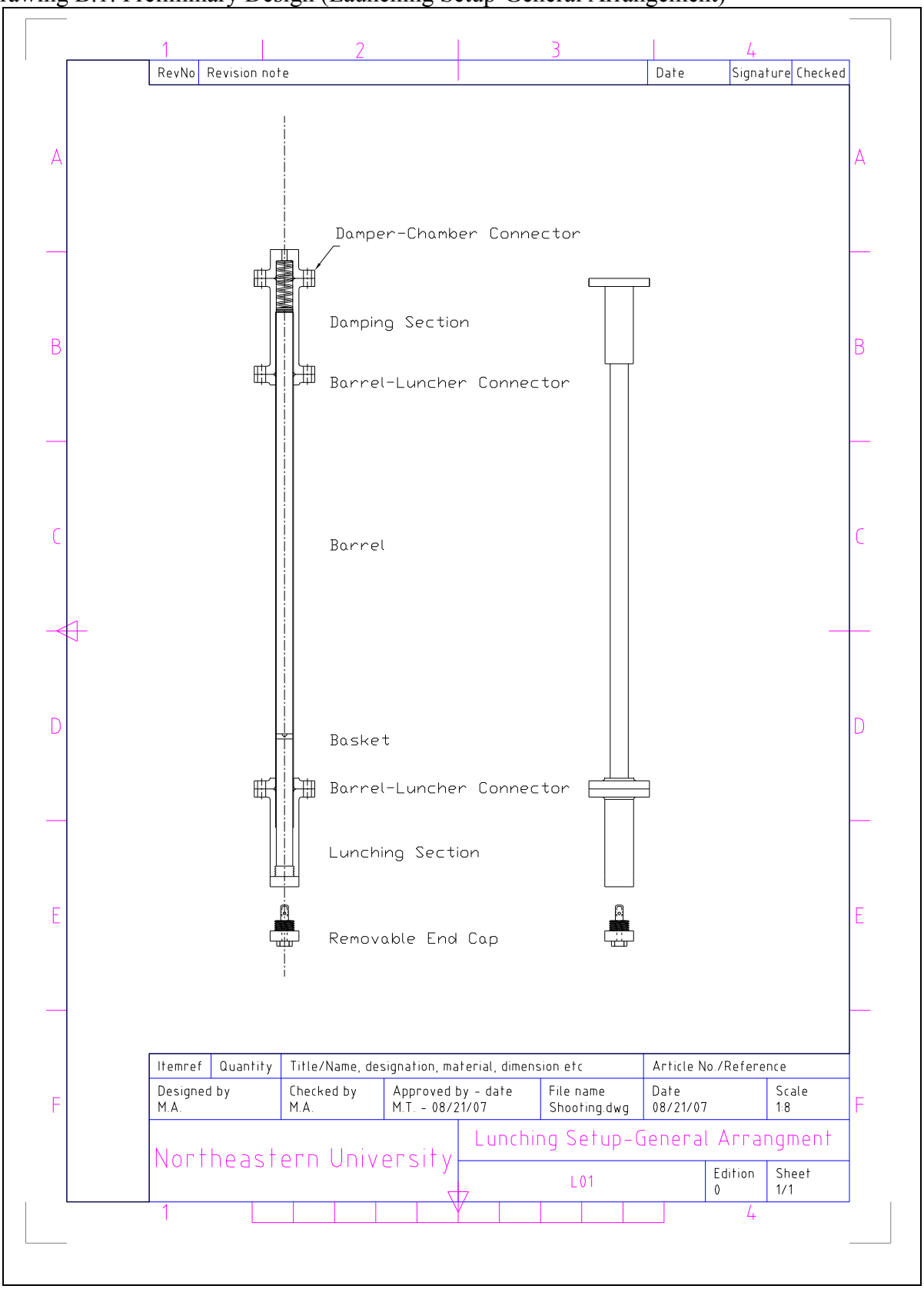

Drawing B.2: Preliminary Design (Launching Setup-Removable End Cap)

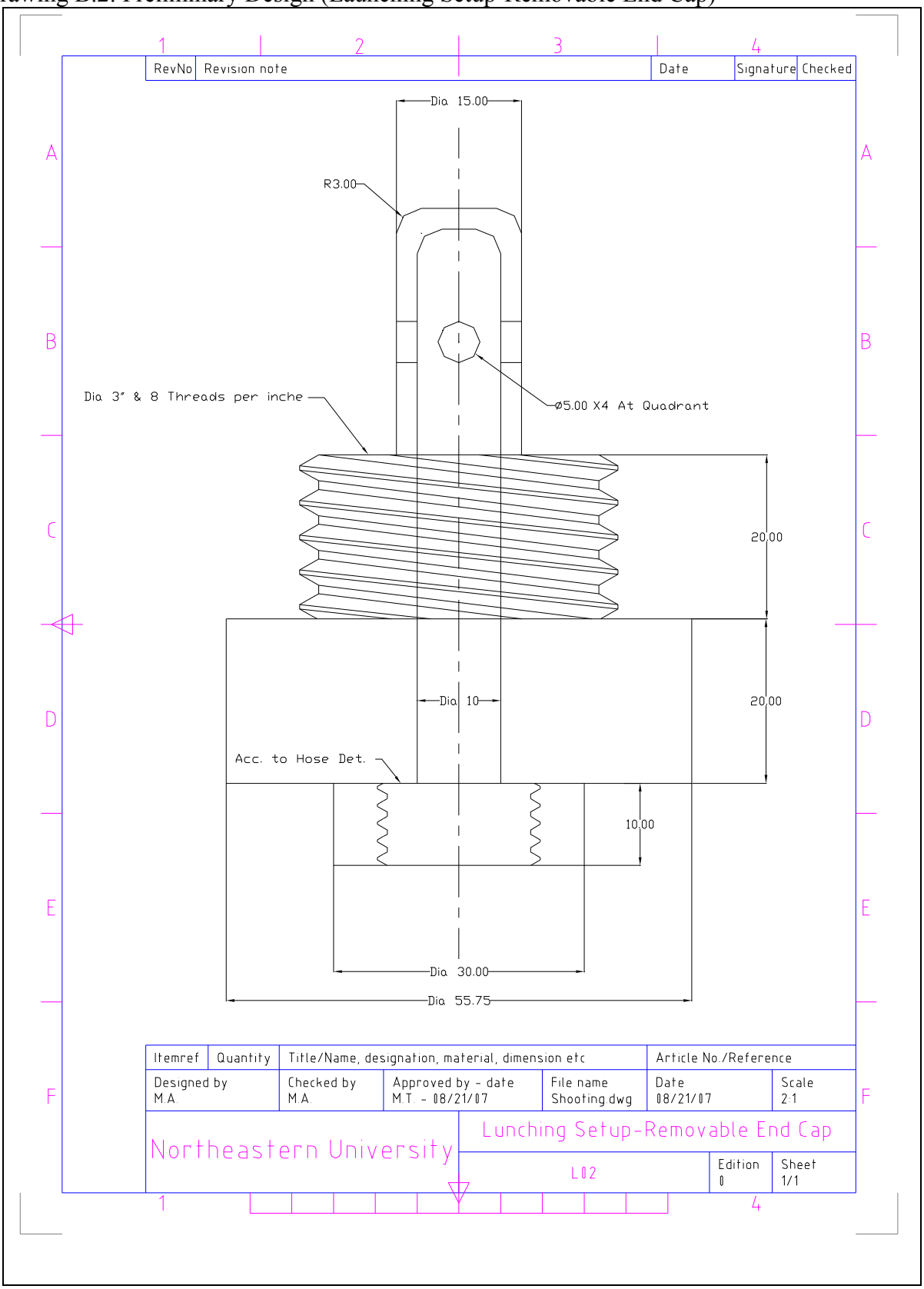

Drawing B.3: Preliminary Design (Launching Setup-Launching Section)

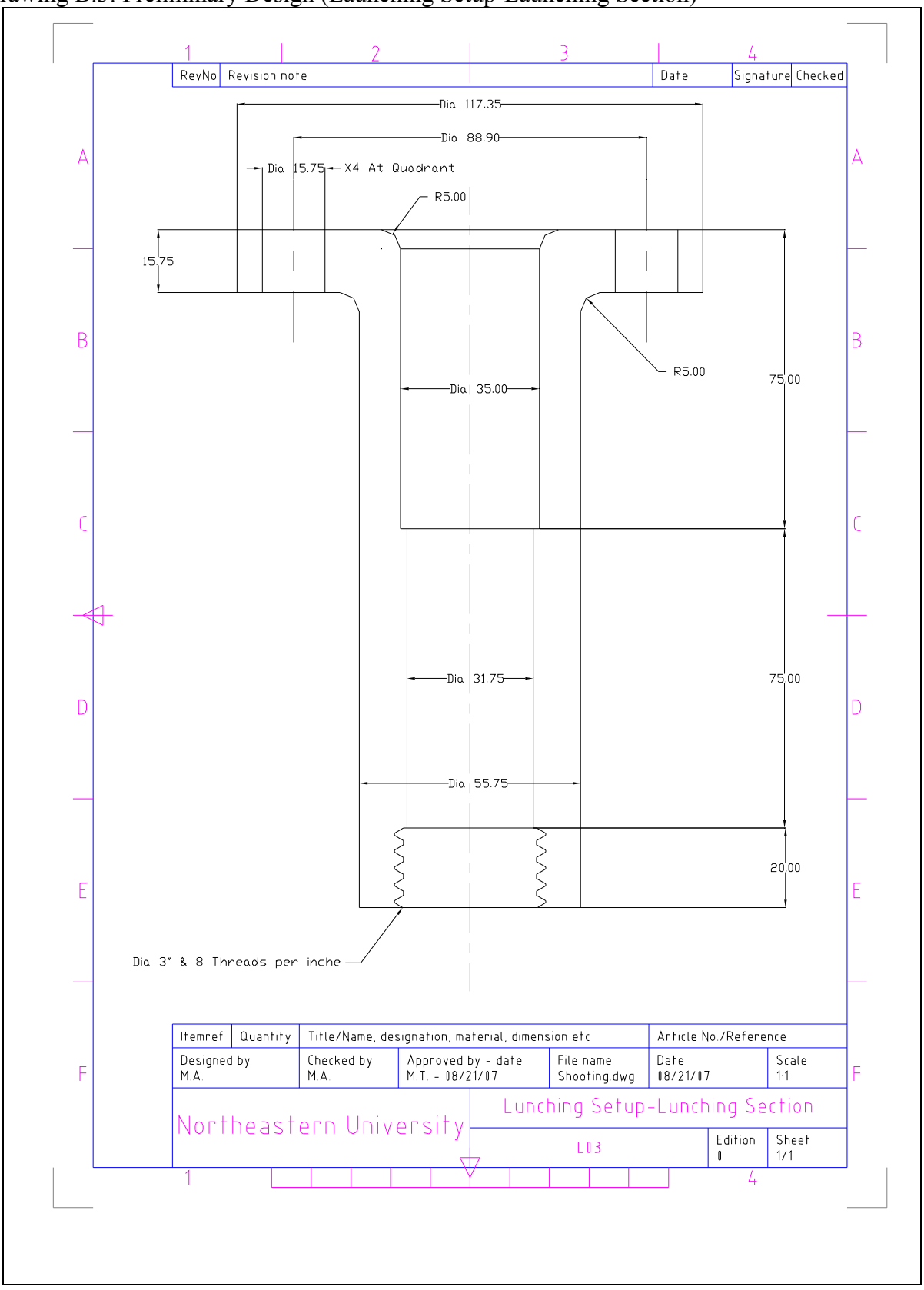

Drawing B.4: Preliminary Design (Launching Setup-Barrel/Launcher Connector)

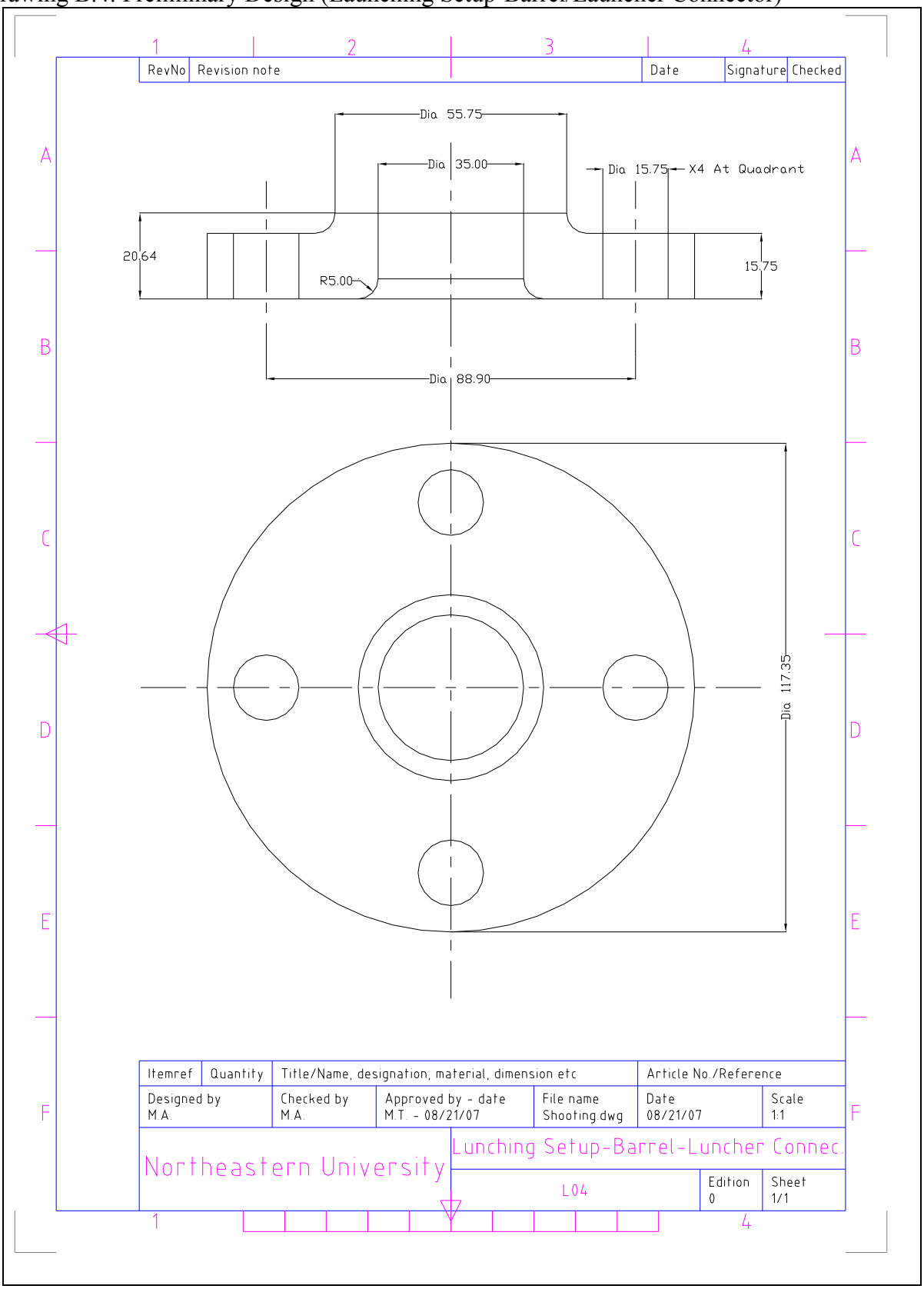

Drawing B.5: Preliminary Design (Launching Setup-Basket)

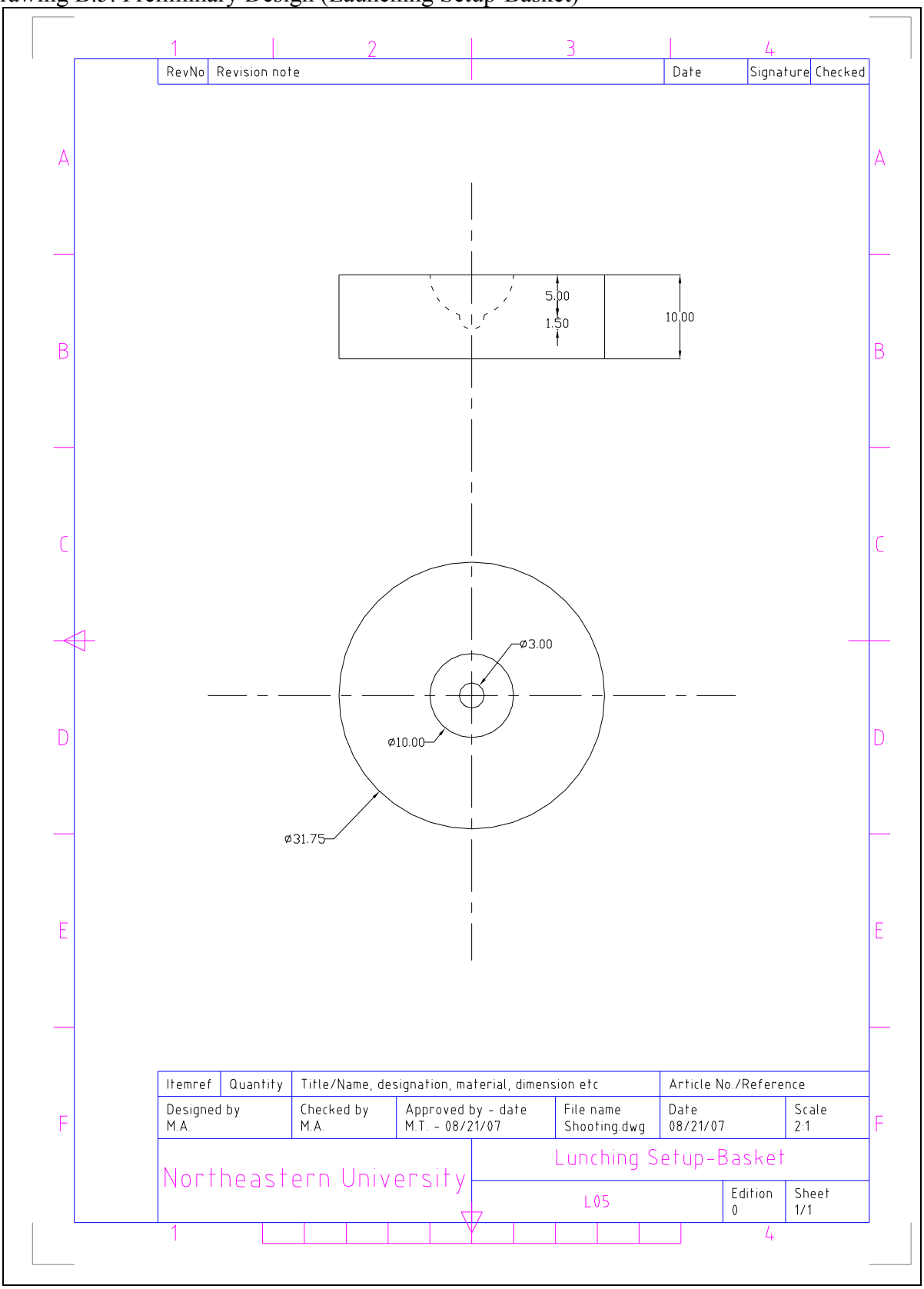

Drawing B.6: Preliminary Design (Launching Setup-Damping Section)

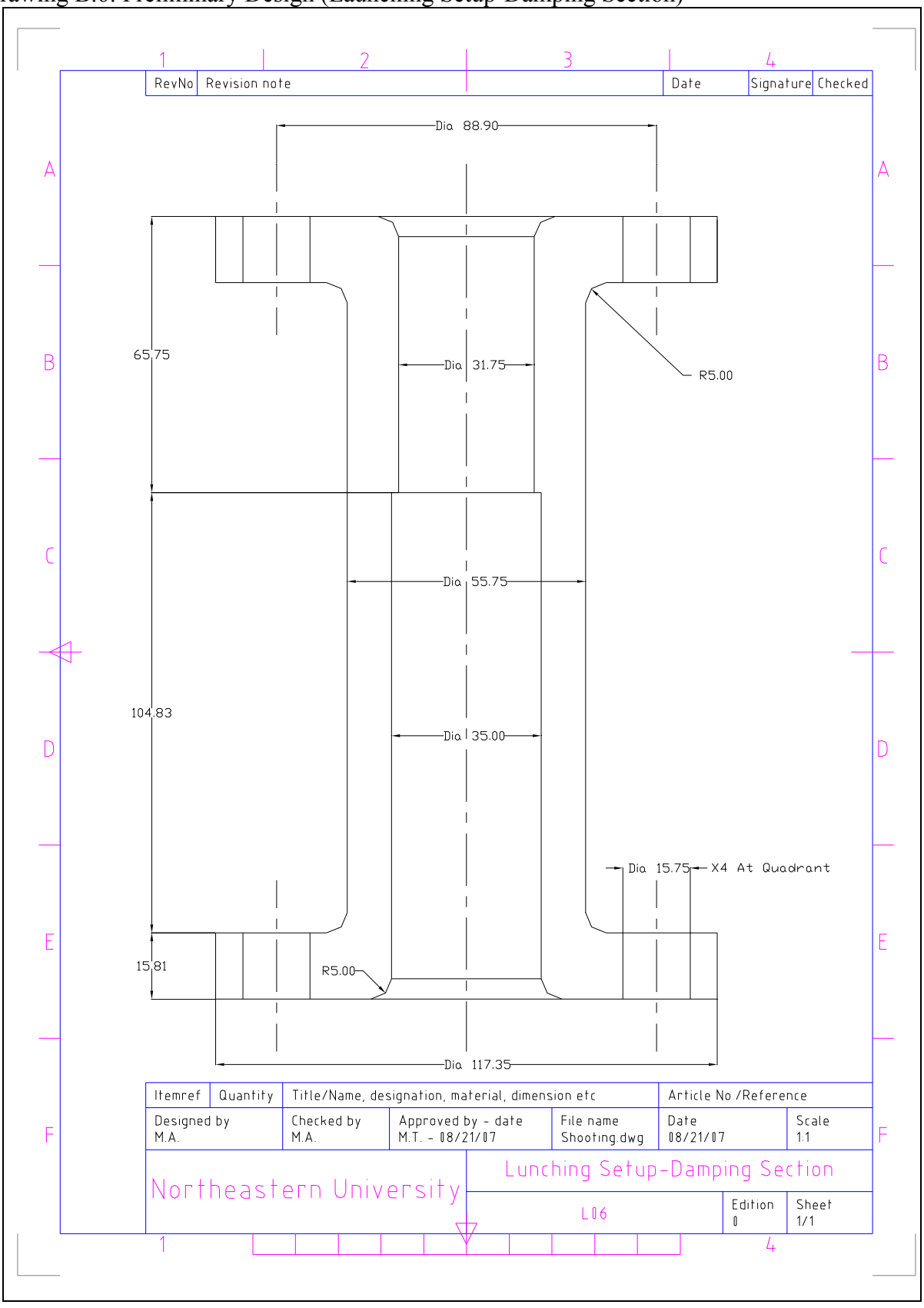

Drawing B.7: Preliminary Design (Launching Setup-Barrel)

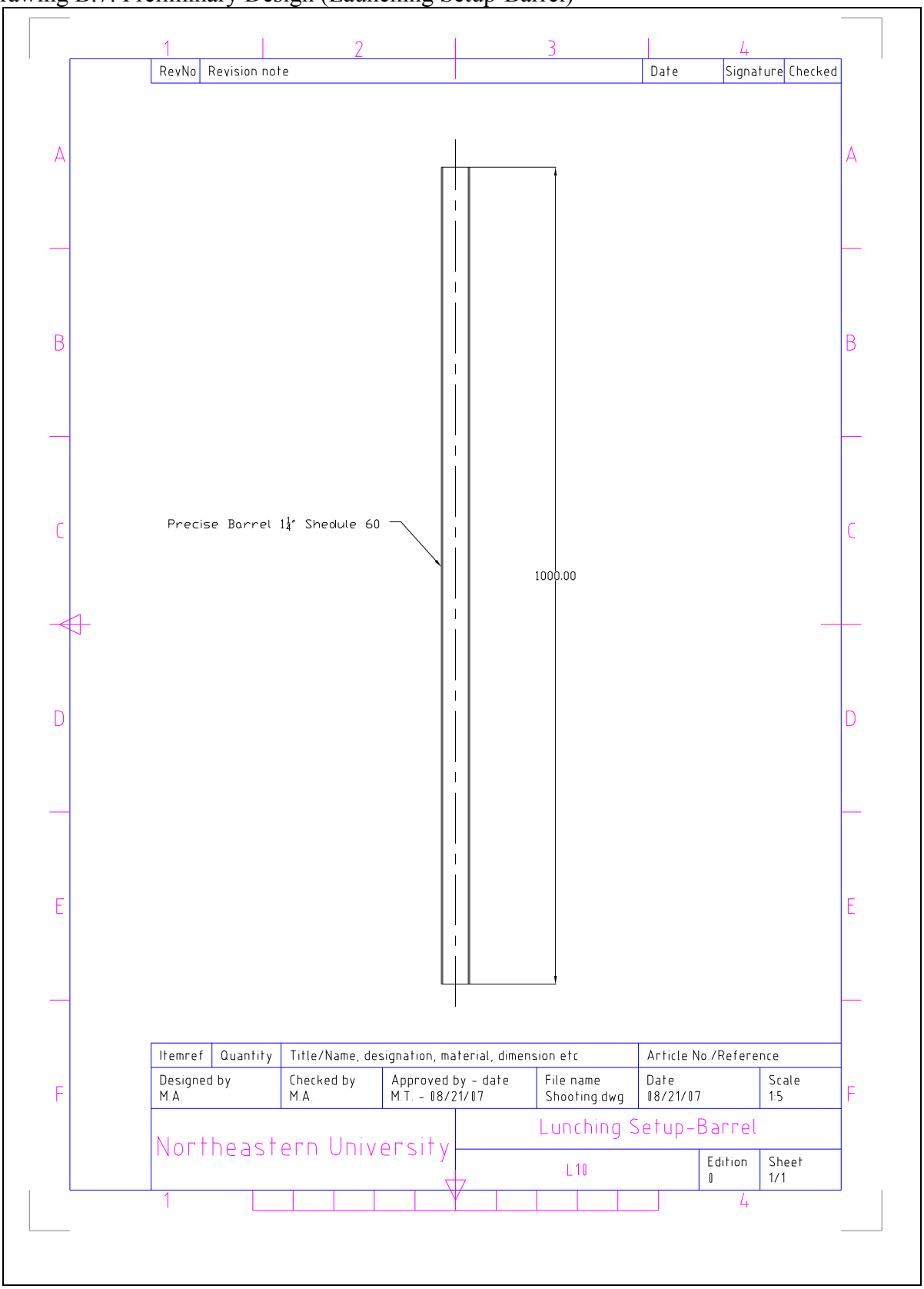

Drawing C.1: Compressed Air Gun (General View)

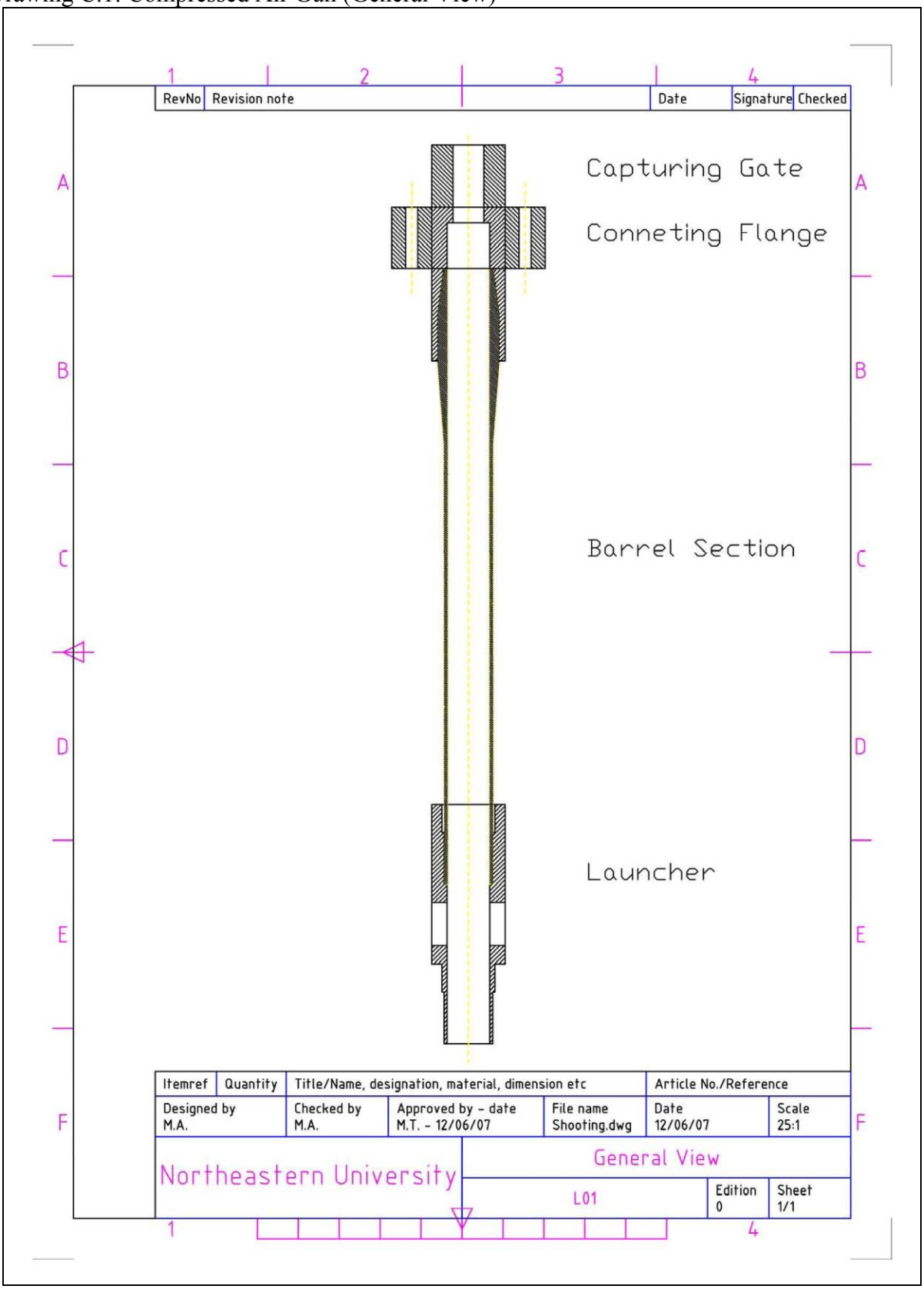

Drawing C.2: Compressed Air Gun (Capturing Gate)

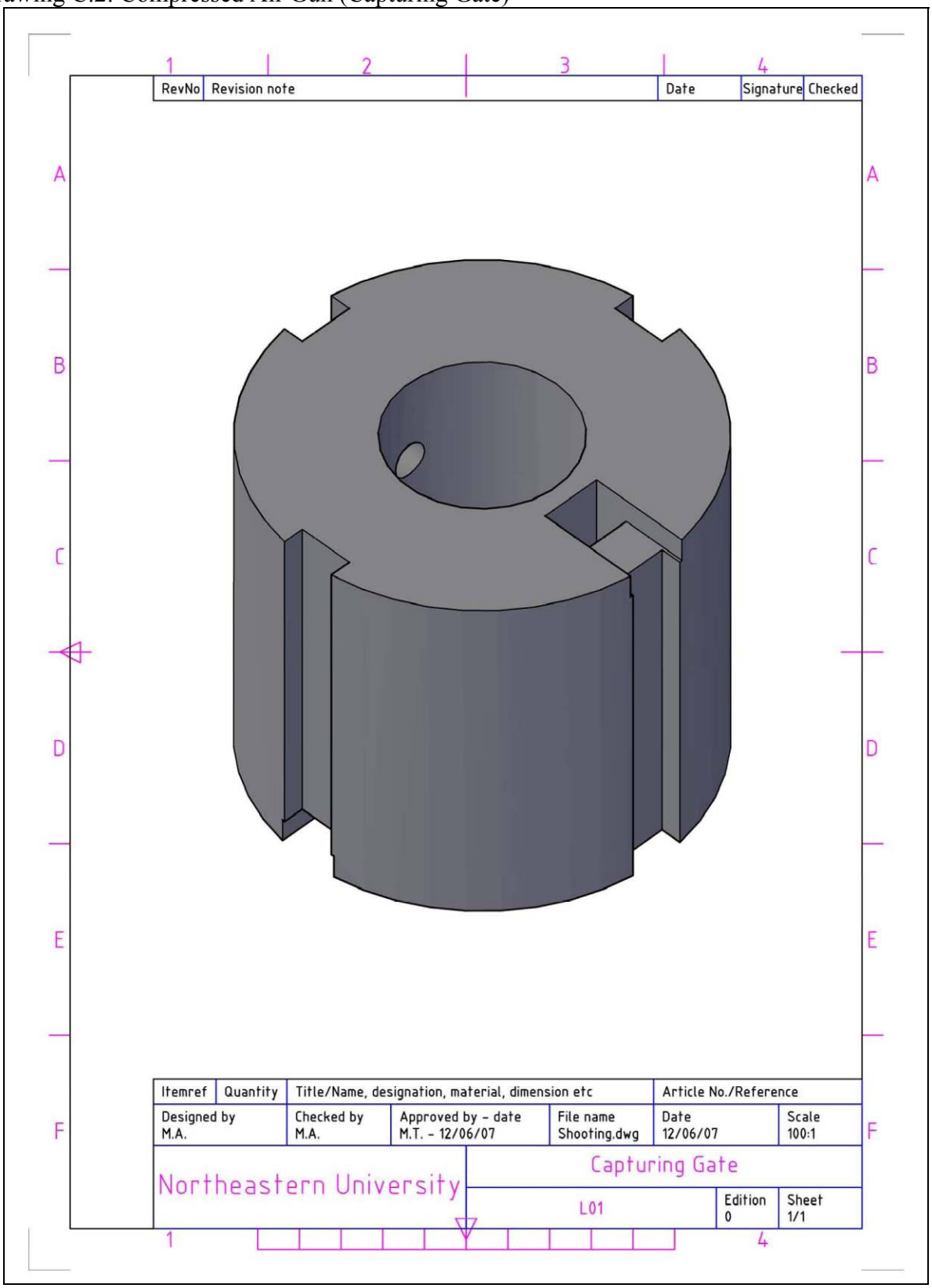

Drawing C.3: Compressed Air Gun (Connection Flange)

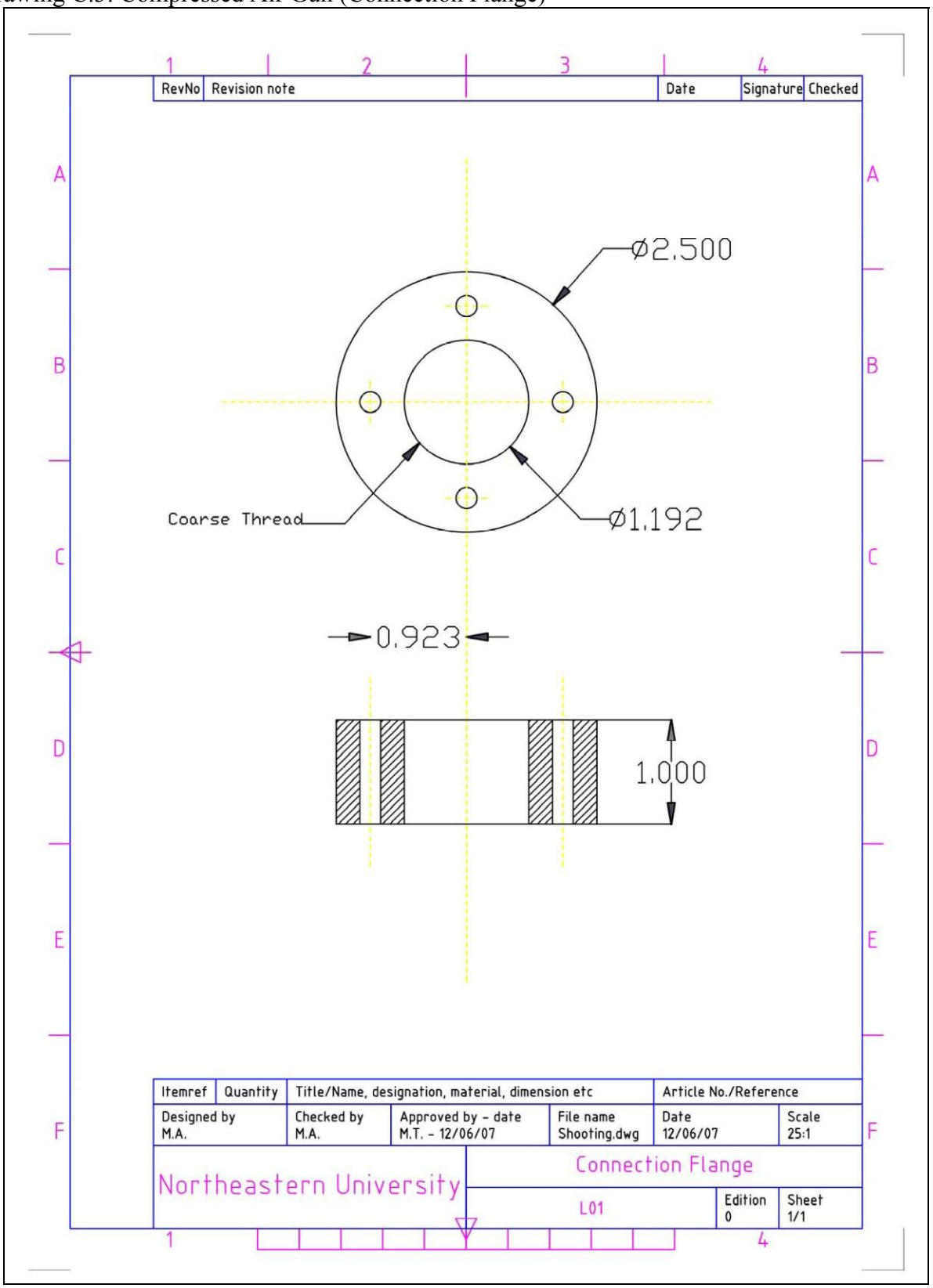

Drawing C.4: Compressed Air Gun (Barrel Cap)

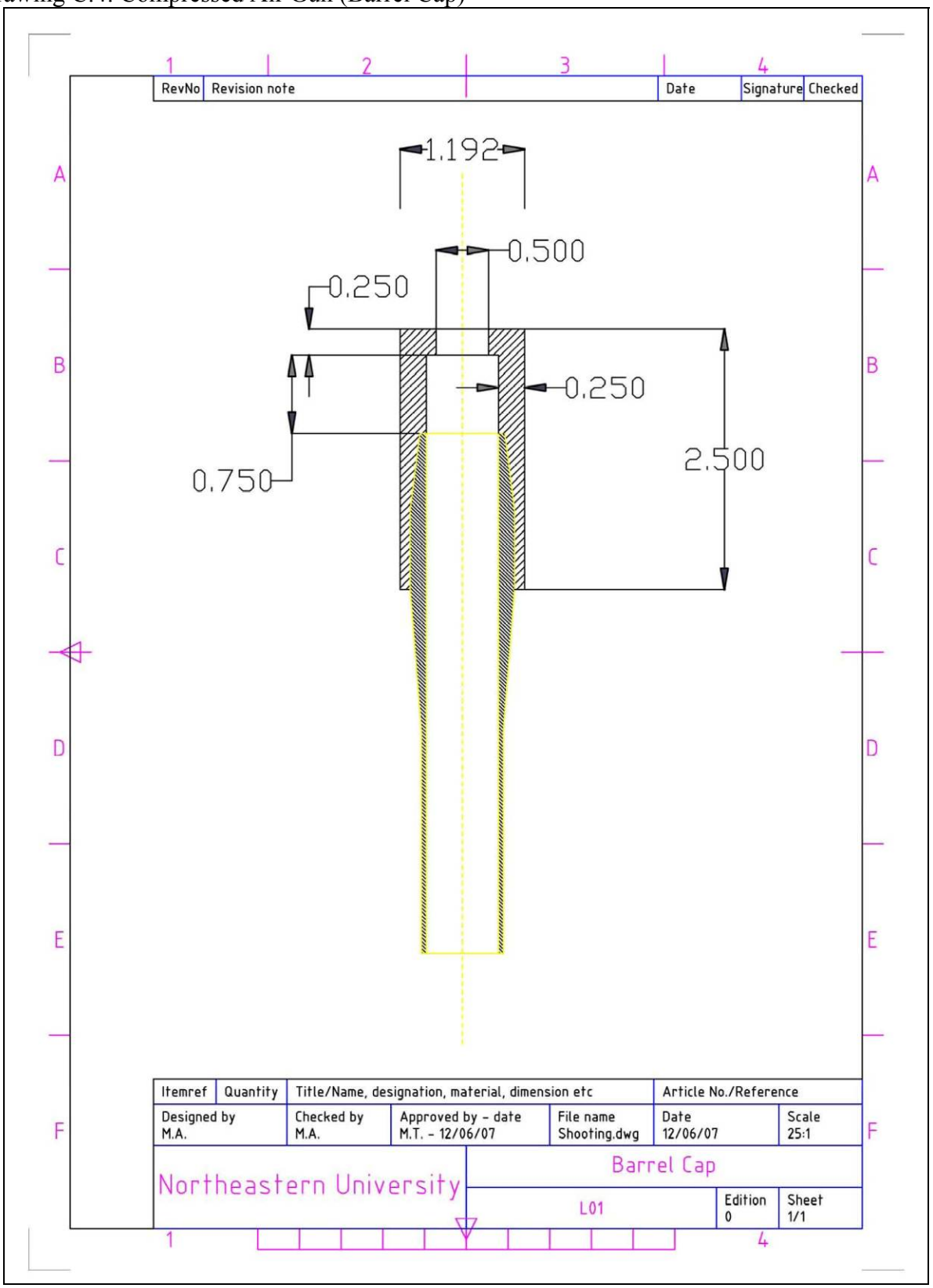

Drawing C.5: Compressed Air Gun (Launcher General View)

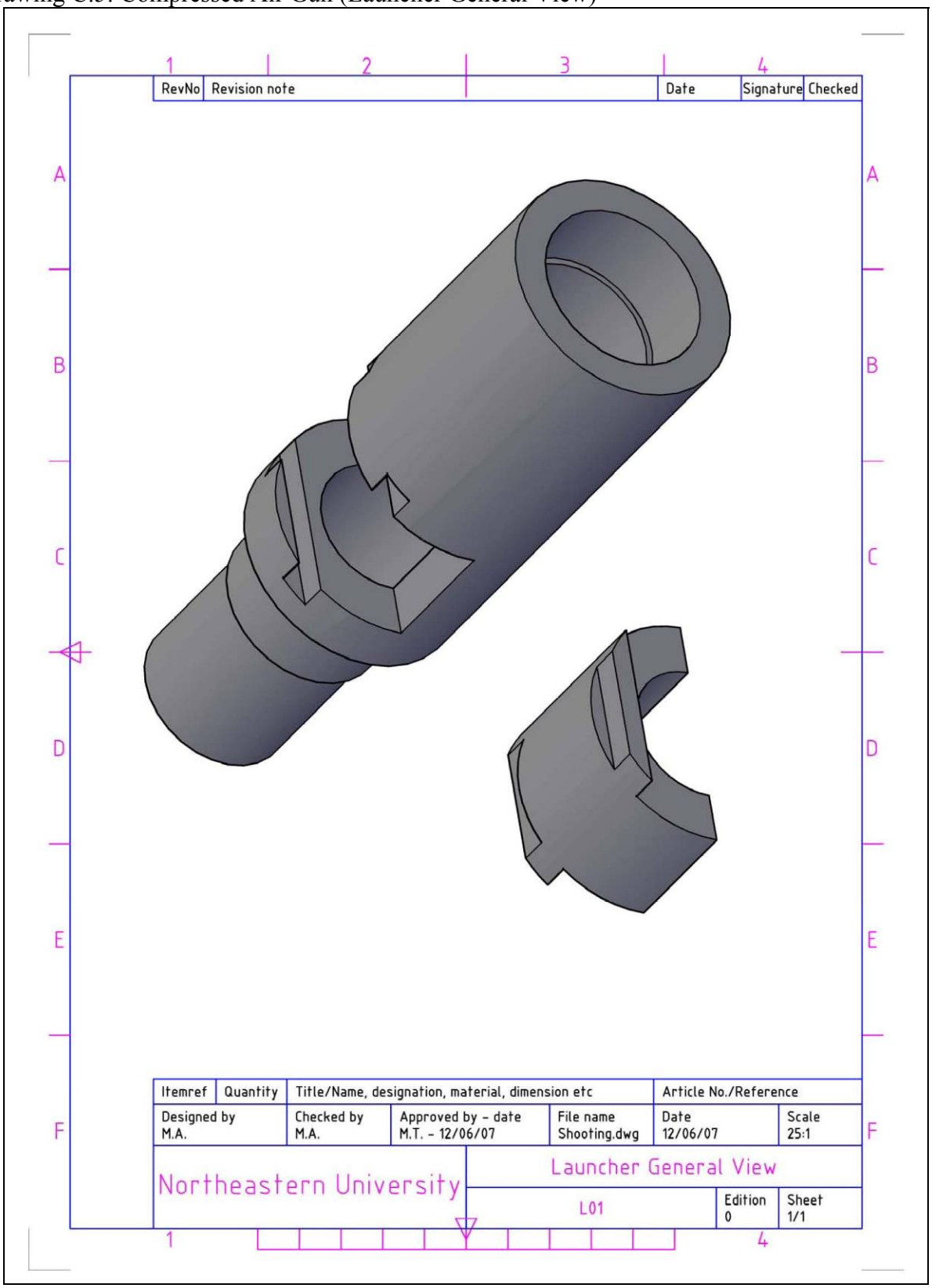

Drawing C.6: Compressed Air Gun (Launcher)

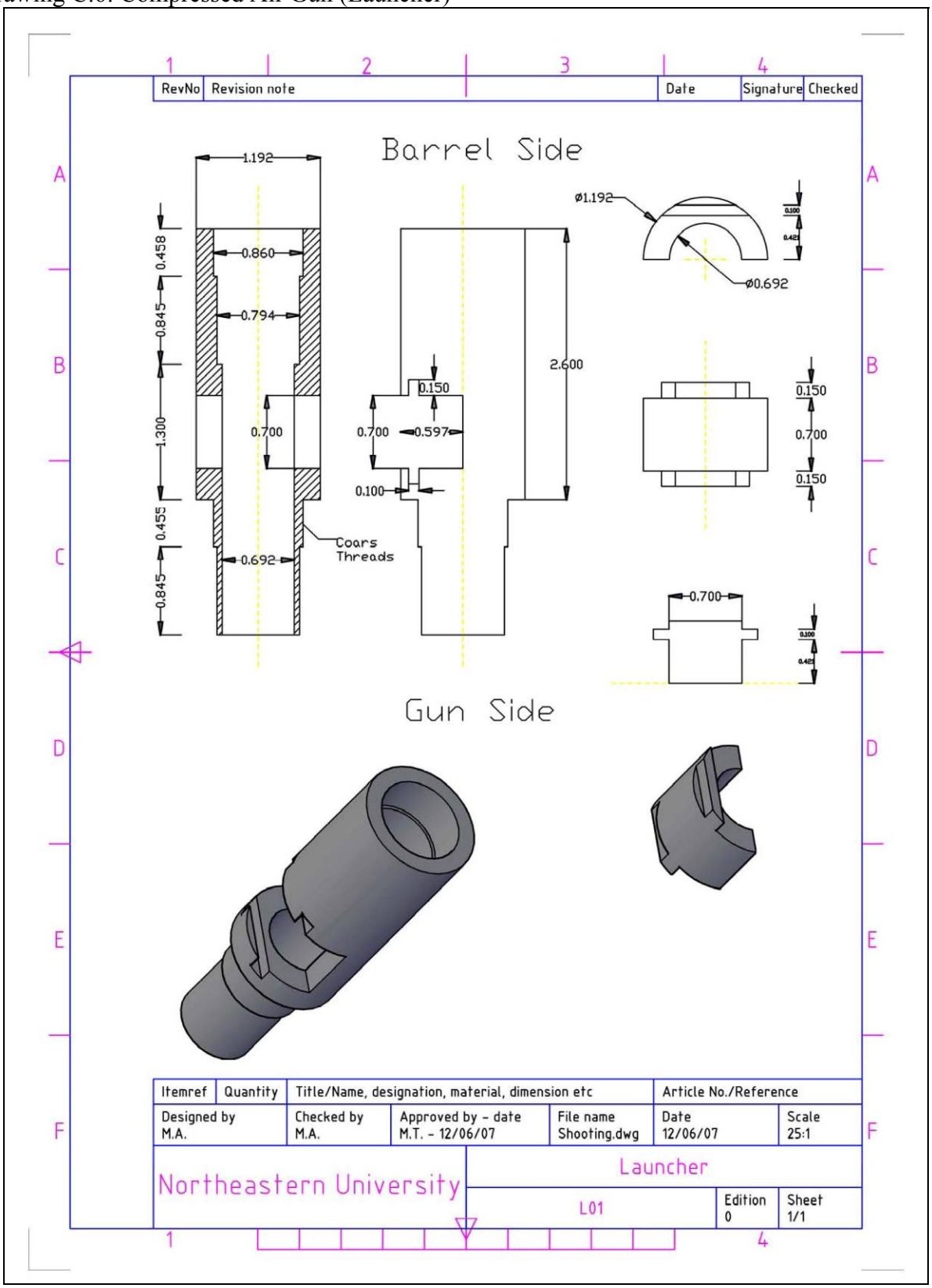

DATA APPENDICES

7.3 CODES

Code A.1: Mathematica® Code for Particle Tracking in a Viscous Driven Flow

```
Q = 0.03;
```

Preliminary Data

```
P = 101;
M = 29;
R = 8.3144;
T = 273.15 + 15;
dia_pipe = 2 * 25.4 / 1000;
ϵ = 0.0015;
len = 1;
d = 1 * 10^-3;
μ = 1.8 * 10^-5;
ρ = 1.2;
ρ_p = 5.553 * 10^3;
g = 9.8;
```

$$\text{re}[u\_] := \frac{\rho\, u\, d}{\mu};$$

$$m = \frac{P\, M}{R\, T}\, Q;$$

$$m_p = 2.204623\, m;$$

```
If[Q == 0,
    v_ma = 0;,
    U = 4 Q / (π dia_pipe^2);
    re_pipe = U dia_pipe ρ / μ;
    f = (-1.8 Log[6.9 / re_pipe + (ϵ / dia_pipe / 3.7)^1.11])^-2;
    v_ma = U (1 + 1.3 √f);]
```

Code A.1: Continue…

```
aD = 3/4 μ^2/(ρ ρp) 1/d^3;
aG = (1 - ρ/ρp) g;
Cv = ρ d/μ;
```

Forced Flow

```
up = 0;
vrel = vma - up;
Print[vma, "-->", re[vrel]]
```

```
x1 = 0;
x2 = 0;
x3 = 0;
x4 = 0;
x5 = 0;
cpass = False;
up = 0;
vrel = vma - up;
pass1 = False;
lCond1 = False;
lCond2 = False;
lCond3 = False;
If[vrel > 0 && re[vrel] ≥ 500,
                          {
                           l1 = vma - 500 μ/(ρ d);
                           solu = NDSolve[
    {u'[t] - aG - 0.44 aD (Cv (vma - u[t]))^2 == 0, u[0] == 0}, u, {t, 0, 2}];
                           utp[t_] := u[t] /. solu;
                           T1 =
   Replace[t, FindRoot[Norm[utp[t]] == l1, {t, 0}].{1}];
                           solutionx =
   NDSolve[{x''[t] - aG - 0.44 aD (Cv (vma - x'[t]))^2 == 0,
     x'[0] == 0, x[0] == 0}, x, {t, 0, T1}];
                           xtp[t_] := x[t] /. solutionx;
                           pass1 = True;
```

Code A.1: Continue…

```
                            up = l1;
                            vrel = vma - up;
                            x1 = xtp[T1].{1};
                            ve1 = utp[T1].{1};
                            lCond1 = True;
                            If[x1 ≥ len,
                                                    {
                                                     te =
     Replace[t, FindRoot[Norm[xtp[t]] = len, {t, 0}].{1}];
                                                     Print[
     te, "-1-", utp[te]];
                                                     cpass = True;
                                                     }
                             ];
                            Print["Turbulance-Forced Flow",
   "/", re[vrel], "-->", T1, "-->", xtp[T1], "-->", utp[T1]]
                            }
]

pass2 = False;
If[vrel > 0 && re[vrel] ≥ 2 && cpass = False,
                           {
                            If[pass1 = True, uinit = up, uinit = 0];
                            l2 = vma - 2 μ / (ρ d);
                            solu = NDSolve[
    {u'[t] - aG - 0.44 aD (Cv (vma - u[t]))^2 = 0, u[0] = uinit}, u, {t, 0, 2}];
                            utp[t_] := u[t] /. solu;
                            T2 =
   Replace[t, FindRoot[Norm[utp[t]] = l2, {t, 0}].{1}];
                            solutionx =
   NDSolve[{x''[t] - aG - 0.44 aD (Cv (vma - x'[t]))^2 = 0,
     x'[0] = uinit, x[0] == 0}, x, {t, 0, T2}];
                            xtp[t_] := x[t] /. solutionx;
                            pass2 = True;
                            up = l2;
                            vrel = vma - up;
                            x2 = xtp[T2].{1};
                            ve2 = utp[T2];
                            lCond2 = True;
                            If[(x2 + x1) ≥ len,
                                                    {
                                                     te =
     Replace[t, FindRoot[Norm[xtp[t]] = len - x1, {t, 0}].{1}];
```

Code A.1: Continue…

```
                                                    Print[
     te, "-2-", utp[te], "-2-", xtp[te]];
                                                    cpass = True;
                                                    }
                            ];
                            Print["Laminar-Forced Flow",
   "/", re[v_rel], "-->", T_2, "-->", xtp[T_2], "-->", utp[T_2]]
                            }
]

If[v_rel > 0 && cpass == False,
                           {
                            If[pass2 == True, u_init = u_p, u_init = 0];
                            solu = NDSolve[
    {u'[t] - a_G - 24 a_D (C_v (v_ma - u[t])) == 0, u[0] == u_init}, u, {t, 0, 0.01}];
                            utp[t_] := u[t] /. solu;
                            T_3 =
   Replace[t, FindRoot[Norm[utp[t]] == v_ma, {t, 0}].{1}];
                            solutionx =
   NDSolve[{x''[t] - a_G - 24 a_D (C_v (v_ma - x'[t])) == 0,
     x'[0] == u_init, x[0] == 0}, x, {t, 0, T_3}];
                            xtp[t_] := x[t] /. solutionx;
                            u_p = v_ma;
                            v_rel = v_ma - u_p;
                            x_3 = xtp[T_3].{1};
                            v_e3 = utp[T_3];
                            lCond3 = True;
                            If[(x_2 + x_1 + x_3) ≥ len,
                                                   {
                                                    te =
     Replace[t, FindRoot[Norm[xtp[t]] == len - x_1 - x_2, {t, 0}].{1}];
                                                    Print[
     te, "-3-", utp[te], "-3-", xtp[te]];
                                                    cpass = True;
                                                    }
                            ];
                            Print["Stokes-Forced Flow",
   "/", re[v_rel], "-->", T_3, "-->", xtp[T_3], "-->", utp[T_3]]
                            }
]
If[cpass == False,
                              {
                               l_4 = 2 μ / (ρ d) + v_ma;
                               u_init = v_ma;
```

Code A.1: Continue…

```
                                solu = NDSolve[
    {u'[t] - aG + 24 aD Cv (u[t] - vma) == 0, u[0] == uinit}, u, {t, 0, 0.1}];
                                utp[t_] := u[t] /. solu;
                                T4 =
   Replace[t, FindRoot[Norm[utp[t]] == l4, {t, 0}].{1}];
                                solutionx =
   NDSolve[{x''[t] - aG + 24 aD Cv (x'[t] - vma) == 0,
     x'[0] == uinit, x[0] == 0}, x, {t, 0, T4}];
                                xtp[t_] := x[t] /. solutionx;
                                up = l4;
                                vrel = up - vma;
                                x4 = xtp[T4].{1};
                                ve4 = utp[T4];
                                If[(x2 + x1 + x3 + x4) ≥ len,
                                                        {
                                                         te =
     Replace[t, FindRoot[Norm[xtp[t]] == len - x1 - x2 - x3, {t, 0}].{1}];
                                                         Print[
     te, "-4-", utp[te], "-4-", xtp[te]];
                                                         cpass = True;
                                                         }
                                 ];
                                Print["Stokes", "/",
   re[vrel], "-->", T4, "-->", xtp[T4], "-->", utp[T4]];
                                }
]
If[cpass == False,
                               {
                                l5 = 500 μ / (ρ d) + vma;
                                uinit = up;
                                solu =
   NDSolve[{u'[t] - aG + 18.5 aD (Cv (u[t] - vma))^1.4 == 0, u[0] == uinit},
    u, {t, 0, 2}];
                                utp[t_] := u[t] /. solu;
                                T5 =
   Replace[t, FindRoot[Norm[utp[t]] == l5, {t, 0}].{1}];
                                solutionx =
   NDSolve[{x''[t] - aG + 18.5 aD (Cv (x'[t] - vma))^1.4 == 0,
     x'[0] == uinit, x[0] == 0}, x, {t, 0, T5}];
                                xtp[t_] := x[t] /. solutionx;
                                up = vma;
                                vrel = vma - up;
                                x5 = xtp[T5].{1};
```

Code A.1: Continue…

```
                                    v_e5 = utp[T_5];
                                    If[(x_2 + x_1 + x_3 + x_4 + x_5) ≥ len,
                                                                        {
                                                                         te = Replace[t,
      FindRoot[Norm[xtp[t]] == len - x_1 - x_2 - x_3 - x_4, {t, 0}].{1}];
                                                                         Print[
     te, "-5-", utp[te], "-5-", xtp[te]];
                                                                         cpass = True;
                                                                         }
                                     ];

                                    Print["Laminar", "/",
   re[v_rel], "-->", T_5, "-->", xtp[T_5], "-->", utp[T_5]];
                                    }
]
If[cpass = False,
                                   {
                                    solutionx =
   NDSolve[{x''[t] - a_G + 0.44 a_D (C_v (x'[t] - v_ma))^2 == 0,
     x'[0] == l_5, x[0] == 0}, x, {t, 0, 2}];
                                    xtp[t_] := x[t] /. solutionx;
                                    te = Replace[t,
    FindRoot[Norm[xtp[t]] == len - x_1 - x_2 - x_3 - x_4 - x_5, {t, 0}].{1}];
                                    solu = NDSolve[
    {u'[t] - a_G + 18.5 a_D (C_v (u[t] - v_ma))^1.4 == 0, u[0] == l_5}, u, {t, 0, te}];
                                    Print[te, "-6-",
   utp[te], "-6-", xtp[te]];
                                    }
]
```

Results

```
Print[utp[te]]
```

Code B.1: Piston-Cylinder with/without Mass Inlet Modeling

```
!     ****************************************************************

!                                  Main

!     ****************************************************************

      Program Main
         Implicit Double Precision (a-h,l-z)

       Parameter(R =8.314D00)!KJ/K Kmol
!        Parameter(D =3.175D-2)!m
         Parameter(D =1.758D-2)!m
!        Parameter(Lo=0.050D00)!m
!        Parameter(Lo=0.040D00)!m
         Parameter(Lo=0.010D00)!m
         Parameter(M =2.900D01)!Kg/Kmol
         Parameter(Cv=0.718D00)!KJ/K Kg
         Parameter(Cp=1.005D00)!KJ/K Kg
         Parameter(Po=1.013D05)!N/m^2
         Parameter(T0=2.930D02)!K
!        Parameter(mp=0.020D00)!Kg
         Parameter(mp=2.550D-3)!Kg
         Parameter(Dt=1.000D-5)!s
         Parameter(Dm=1.000D-3)!Kg

       Pi=DACos(-1.00D00)

         Open(100,File='OutPV.Dat')
         Open(200,File='OutXT.Dat')

       I=360

       mi=I*Dm

!       Initial Conditions
        X =0.00D00
            PX=0.00D00
            T =0.00D00

            Xn  =Lo
            Xn_1=Lo
!           Pn=689475.700D00
        Pn=Po
!       Pn=66.400D05
!       Pn=16.400D05
            Tn=T0

        Time=0.00D00

            Do While (X .Lt. 0.270D00 .and. Time .lt. 2.00D00)
             Time=Time+Dt

         X =(Pn-Po)*Pi*D**2.00D00*Dt**2.00D00/(4.00D00*mp)+2.00D00*Xn-Xn_1
```

Code B.1: Continue…

```
              PX=-Po*R*(X-Xn)/(M*Cv) &
                 +4.00D00*mi*Cp*1.00D03*T0*R*Dt/(Cv*Pi*D**2.00D00*M) &
                   +(Pn*Xn)

              T = Tn* PX/(Pn*Xn) &
                -
mi*Tn**2.00D00*4.00D00*R*1.00D03*Dt/(Pi*D**2.00D00*M*(Pn*Xn))

          vel=(X-Xn)/Dt

              Xn_1=Xn
              Xn  =X

              Tn  =T

              Pn  =PX/X

!         Write(100,*)X,Pn*0.000145,Vel

          Write(100,*)X,Pn/1.00D05,Vel
              Write(200,*)Time,X,T
             End Do
         End

!
```

Code C.1: User Defined Function (UDF) for Defining the Complex Restitution Coefficients

```
/* reflect boundary condition for inert particles */
/* Only for Particle Dia. 015um */
#include "udf.h"
DEFINE_DPM_BC(bc_reflect,p,t,f,f_normal,dim)
{
 real alpha;  /* angle of particle path with face normal */
 real vn=0.;
 real nor_coeff ;
 real tan_coeff ;
 real normal[3];
 int i, idim = dim;
 real NV_VEC(x);

 real velmag ;

 real a0=;
 real a1=;
 real a2=;
 real a3=;

 real b0=;
 real b1=;
 real b2=;
 real b3=;
 real b4=;

 b0= 0.3437;
 b1= 0.0867;
 b2=-0.0044;
 b3= 8.E-5 ;
 b4=-5.E-7 ;

 velmag=NV_MAG(p->state.V);

 if (velmag <= 7.)
   {
    a0=0.9637 ;
    a1=-0.0071;
    a2=0.0001 ;
    a3=-5.E-7 ;
   }

 if ((velmag > 7.) && (velmag <= 30.))
```

Code B.1: Continue…

```
    {
     a0= 0.9465;
     a1=-0.0085;
     a2= 0.0001;
     a3=-5.E-7 ;
    }

  if ((velmag > 30.) && (velmag <= 70.))
    {
     a0= 1.0951;
     a1=-0.0219;
     a2= 0.0003;
     a3=-1.E-6 ;
    }

  if (velmag > 70.)
    {
     a0= 1.1338;
     a1=-0.0234;
     a2= 0.0003;
     a3=-1.E-6 ;
    }

#if RP_2D
  /* dim is always 2 in 2D compilation. Need special treatment for 2d
     axisymmetric and swirl flows */
  if (rp_axi_swirl)
    {
     real R = sqrt(p->state.pos[1]*p->state.pos[1] +
                   p->state.pos[2]*p->state.pos[2]);
     if (R > 1.e-20)
       {
        idim = 3;
        normal[0] = f_normal[0];
        normal[1] = (f_normal[1]*p->state.pos[1])/R;
        normal[2] = (f_normal[1]*p->state.pos[2])/R;
       }
     else
       {
        for (i=0; i<idim; i++)
          normal[i] = f_normal[i];
       }
```

Code B.1: Continue…

```
   }
  else
#endif
    for (i=0; i<idim; i++)
      normal[i] = f_normal[i];

  if(p->type==DPM_TYPE_INERT)
    {
      alpha = acos(MAX(-1.,MIN(1.,NV_DOT(normal,p->state.V)/
                               MAX(NV_MAG(p->state.V),DPM_SMALL))));
      alpha=alpha*180/M_PI
      nor_coeff=a0+a1*alpha+a2*alpha*alpha+a3*alpha*alpha*alpha;

tan_coeff=b0+a1*alpha+b2*alpha*alpha+b3*alpha*alpha*alpha+b4*alpha*alpha*alpha*alpha;
      if ((NNULLP(t)) && (THREAD_TYPE(t) == THREAD_F_WALL))
        F_CENTROID(x,f,t);

      /* calculate the normal component, rescale its magnitude by
         the coefficient of restitution and subtract the change */

      /* Compute normal velocity. */
      for(i=0; i<idim; i++)
        vn += p->state.V[i]*normal[i];

      /* Subtract off normal velocity. */
      for(i=0; i<idim; i++)
        p->state.V[i] -= vn*normal[i];

      /* Apply tangential coefficient of restitution. */
      for(i=0; i<idim; i++)
        p->state.V[i] *= tan_coeff;

      /* Add reflected normal velocity. */
      for(i=0; i<idim; i++)
        p->state.V[i] -= nor_coeff*vn*normal[i];

      /* Store new velocity in state0 of particle */
      for(i=0; i<idim; i++)
        p->state0.V[i] = p->state.V[i];

      return PATH_ACTIVE;
    }
```

Code B.1: Continue…

```
  return PATH_ABORT;
}
```

DATA APPENDICES

7.4 GRAPHS & RESULTS

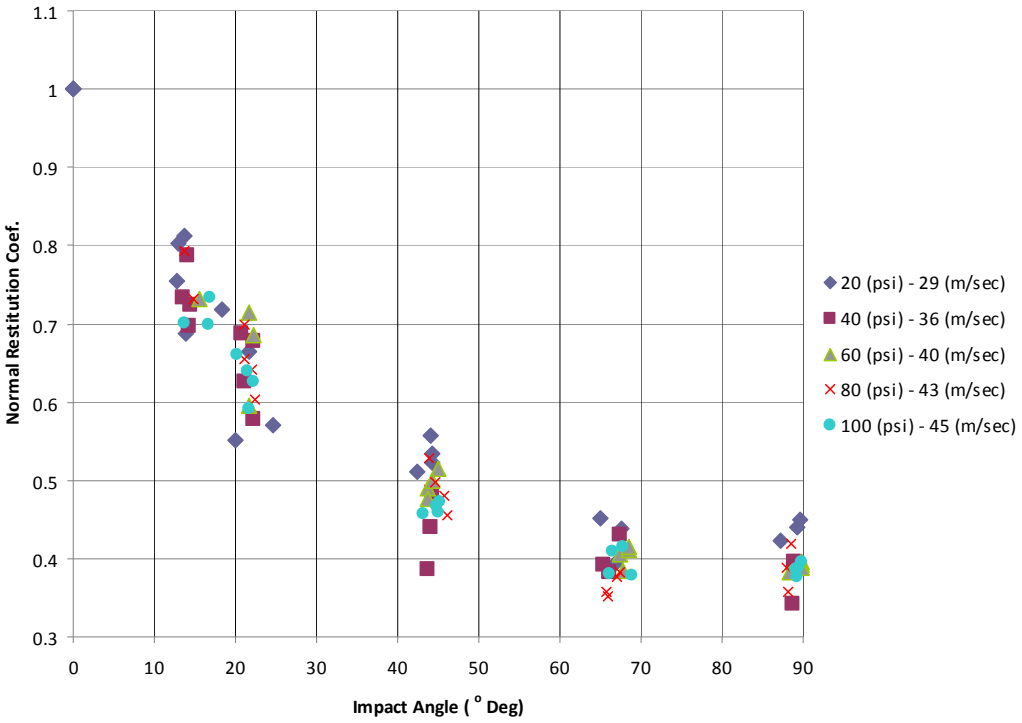

Figure 7-1 Capstone Design-Normal Restitution Coefficient (Exp. Data)

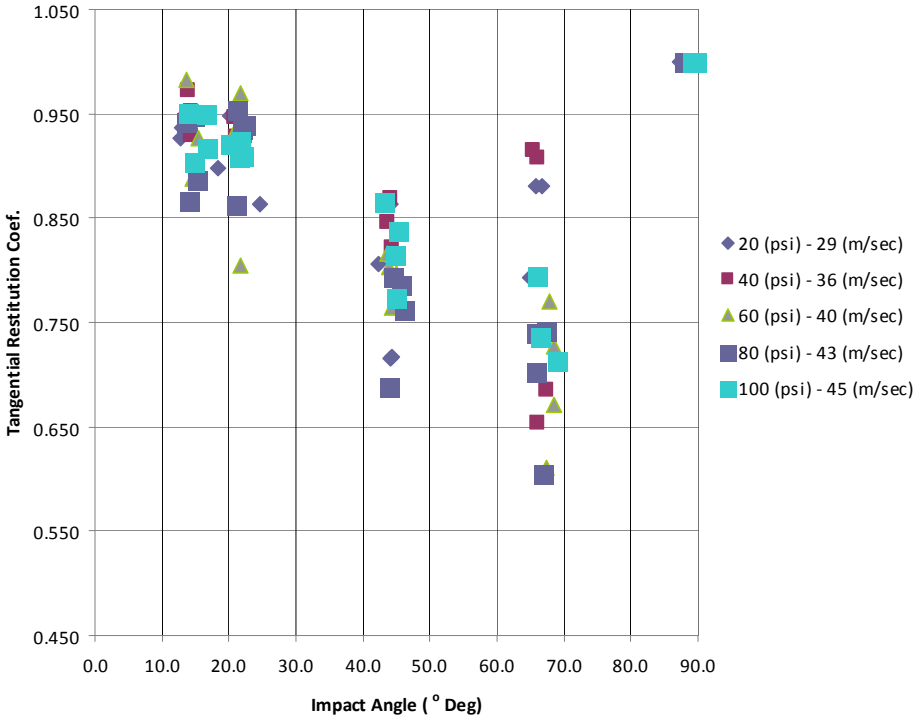

Figure 7-2 Capstone Design-Tangential Restitution Coefficient (Exp. Data)

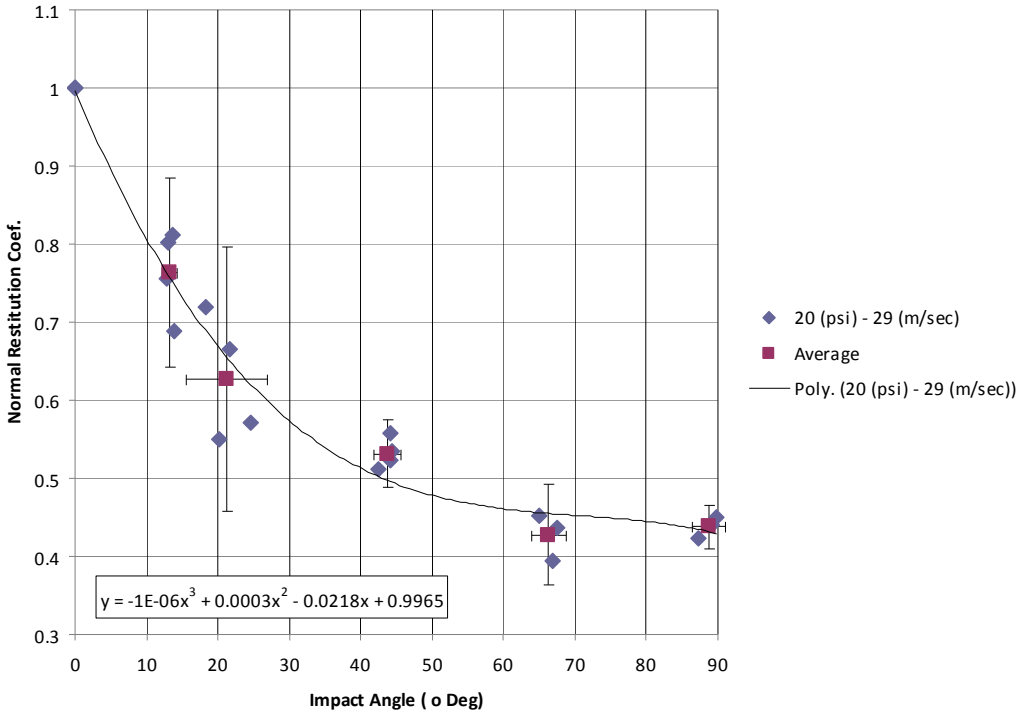

Figure 7-3 Capstone Design-Normal Restitution Coefficient (20 psi)

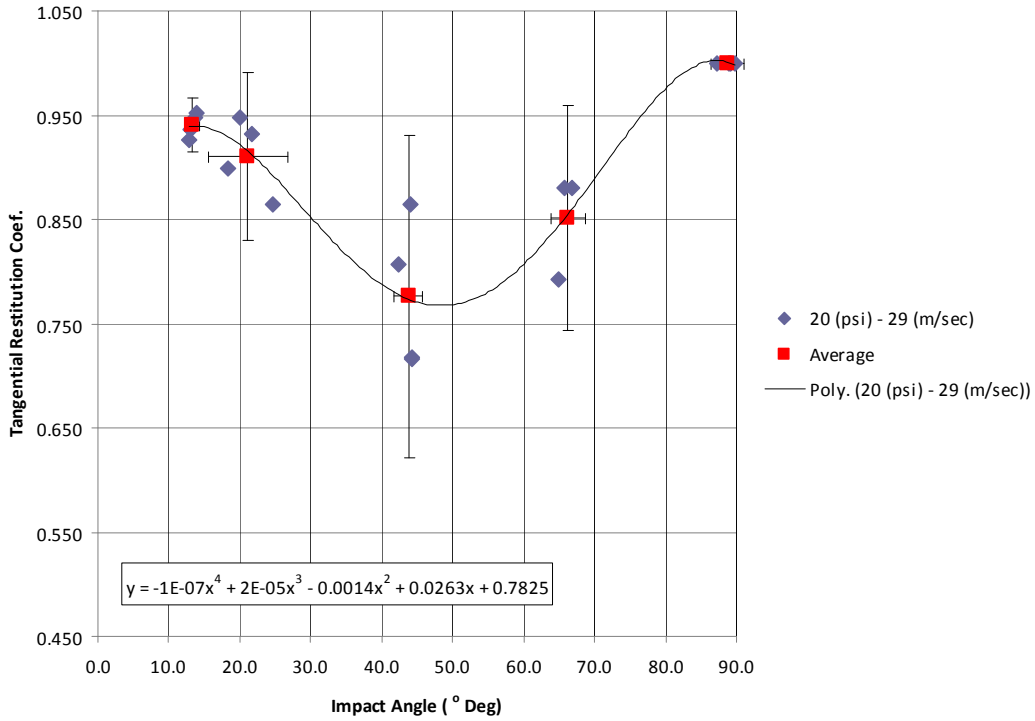

Figure 7-4 Capstone Design-Tangential Restitution Coefficient (20 psi)

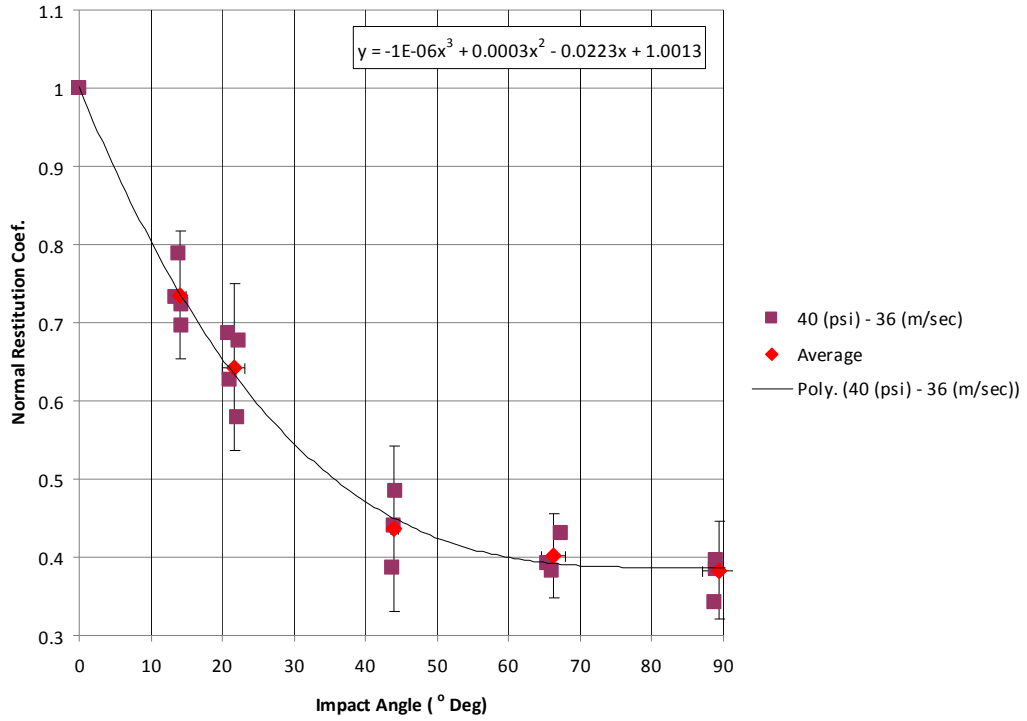

Figure 7-5 Capstone Design-Normal Restitution Coefficient (40 psi)

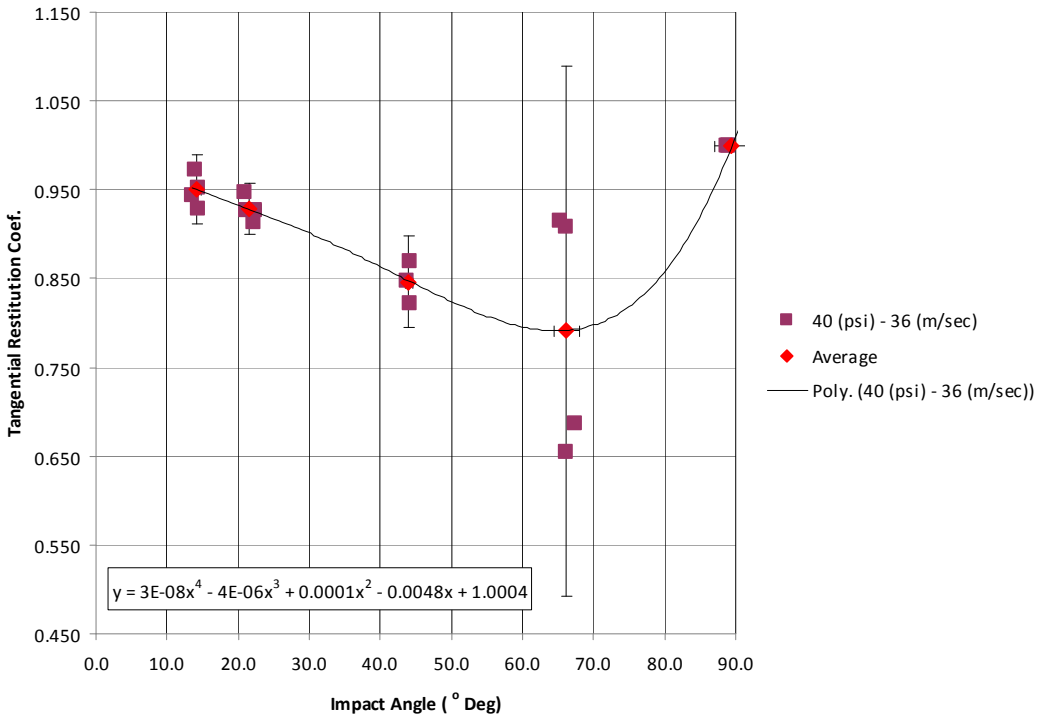

Figure 7-6 Capstone Design-Tangential Restitution Coefficient (40 psi)

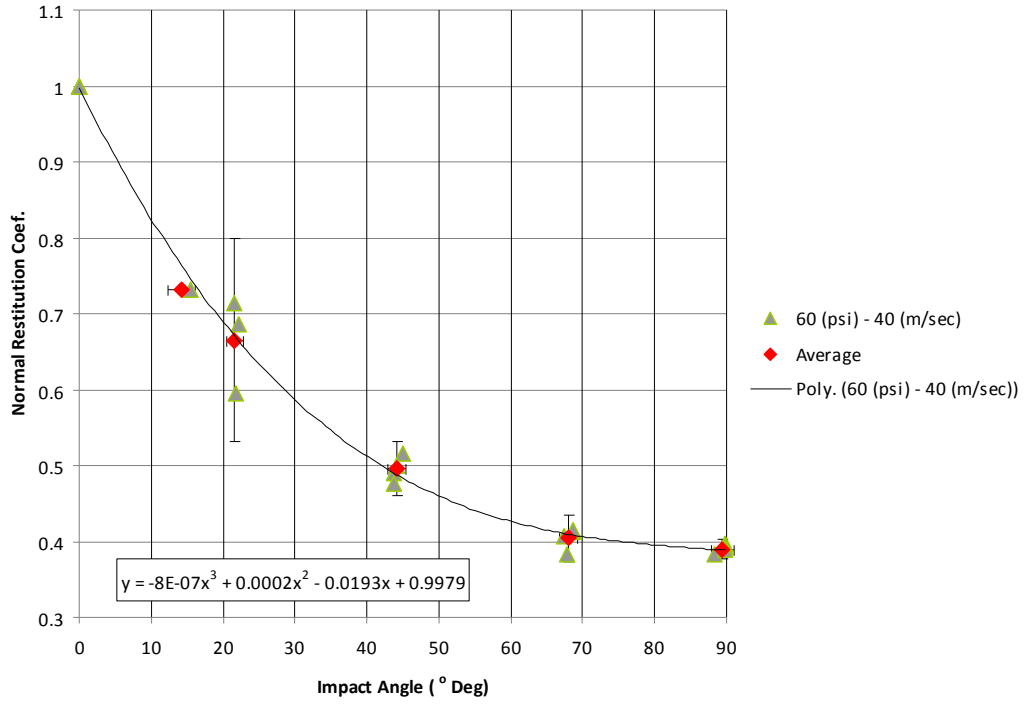

Figure 7-7 Capstone Design-Normal Restitution Coefficient (60 psi)

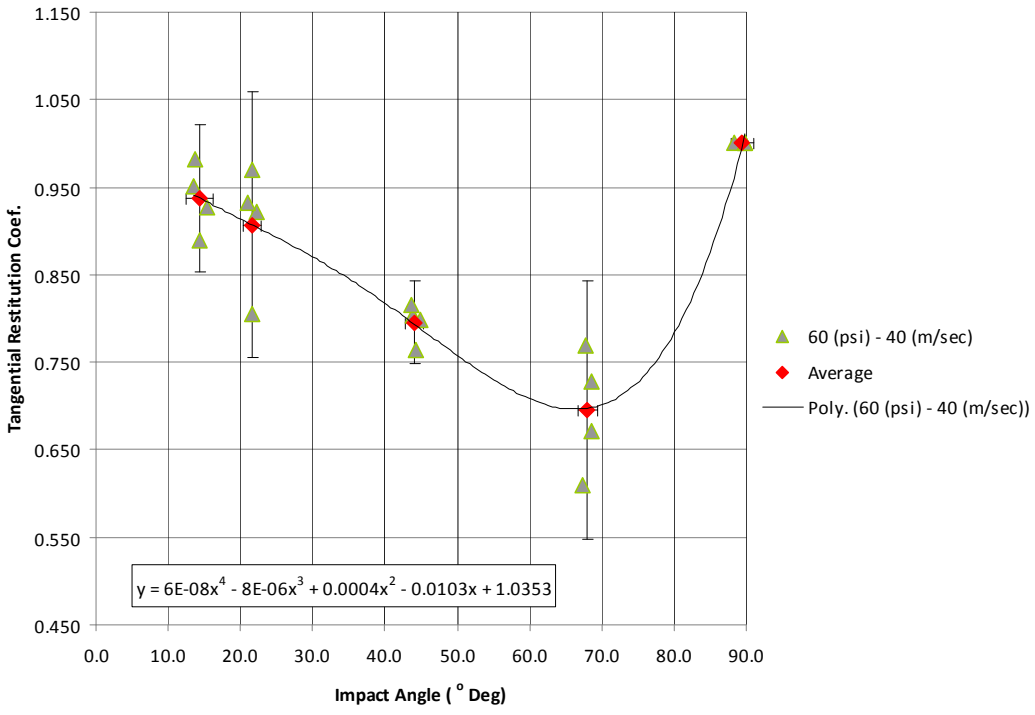

Figure 7-8 Capstone Design-Tangential Restitution Coefficient (60 psi)

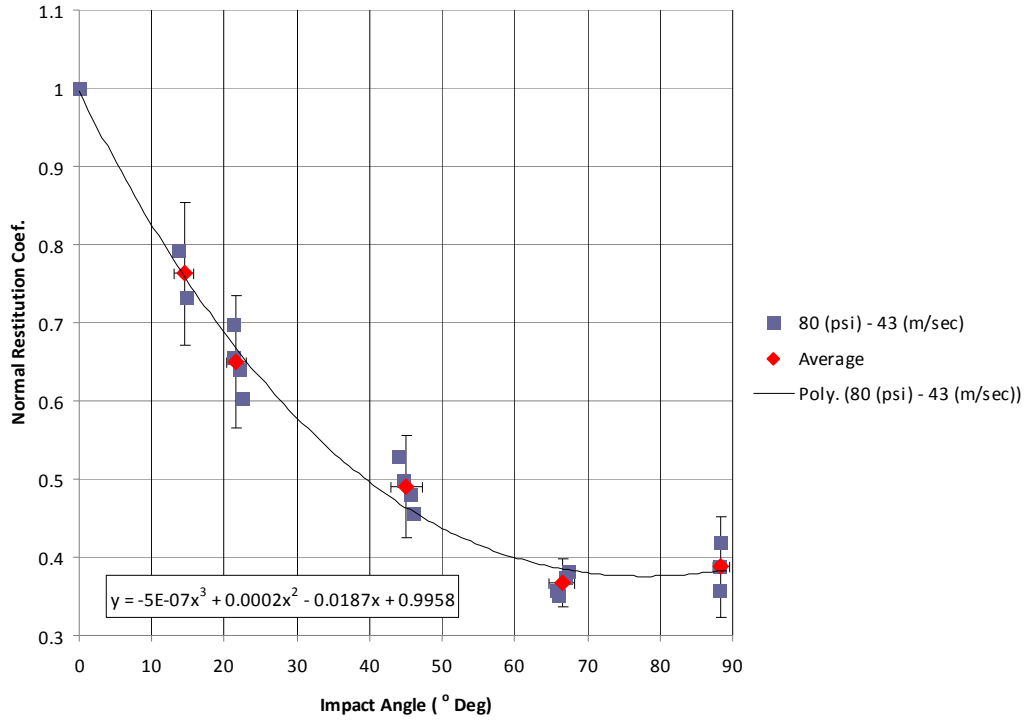

Figure 7-9 Capstone Design-Normal Restitution Coefficient (80 psi)

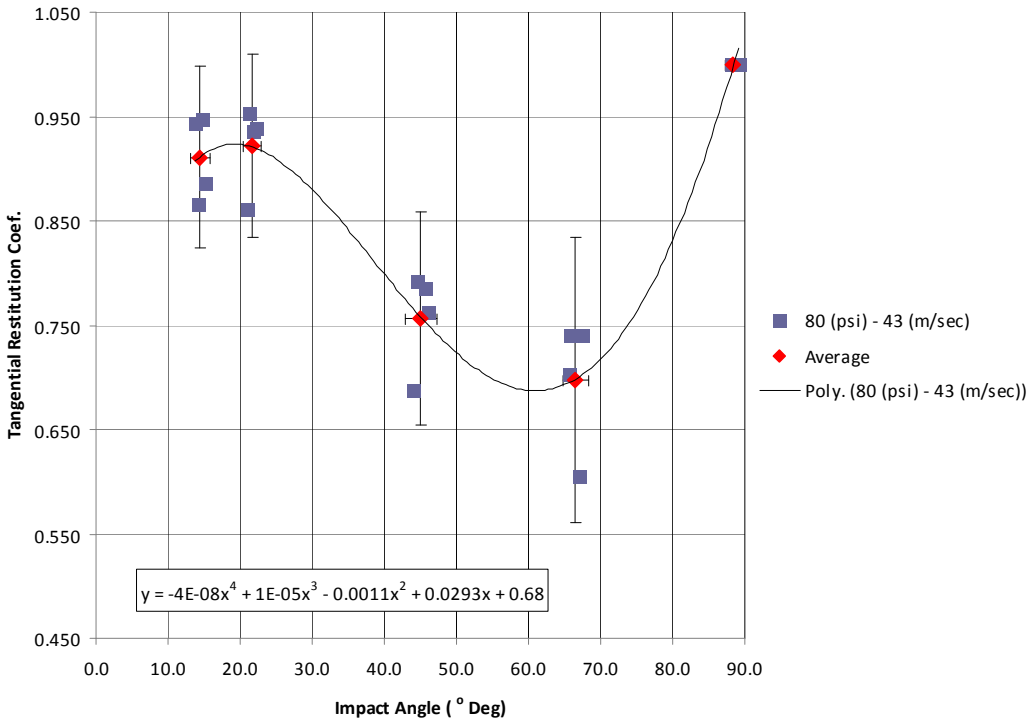

Figure 7-10 Capstone Design-Tangential Restitution Coefficient (80 psi)

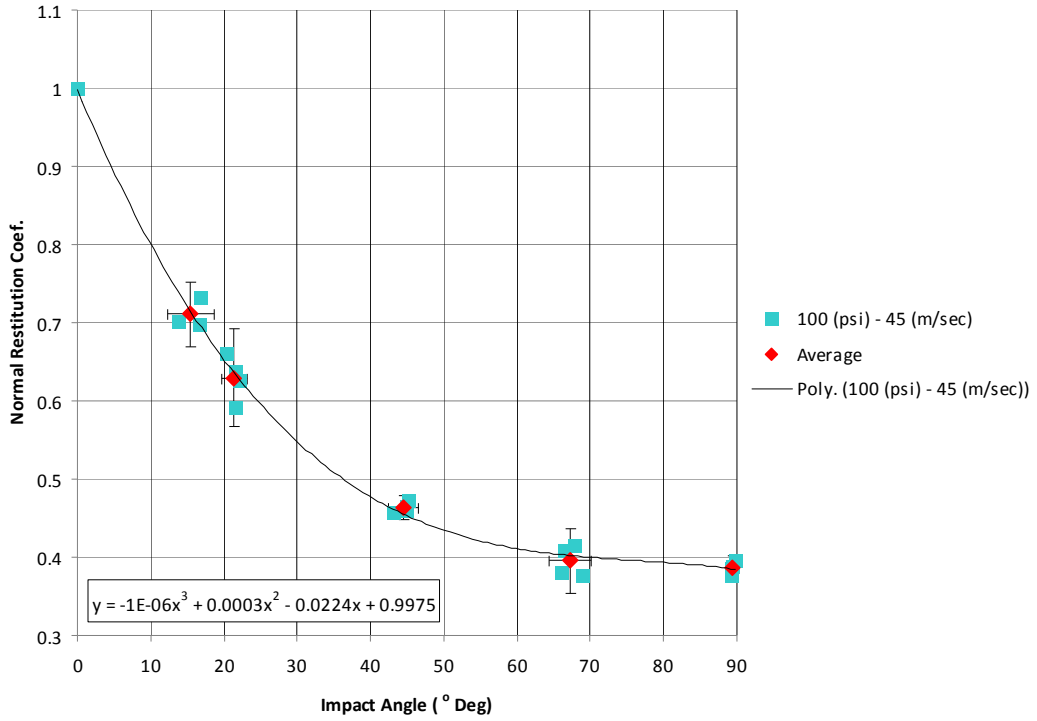

Figure 7-11 Capstone Design-Normal Restitution Coefficient (100 psi)

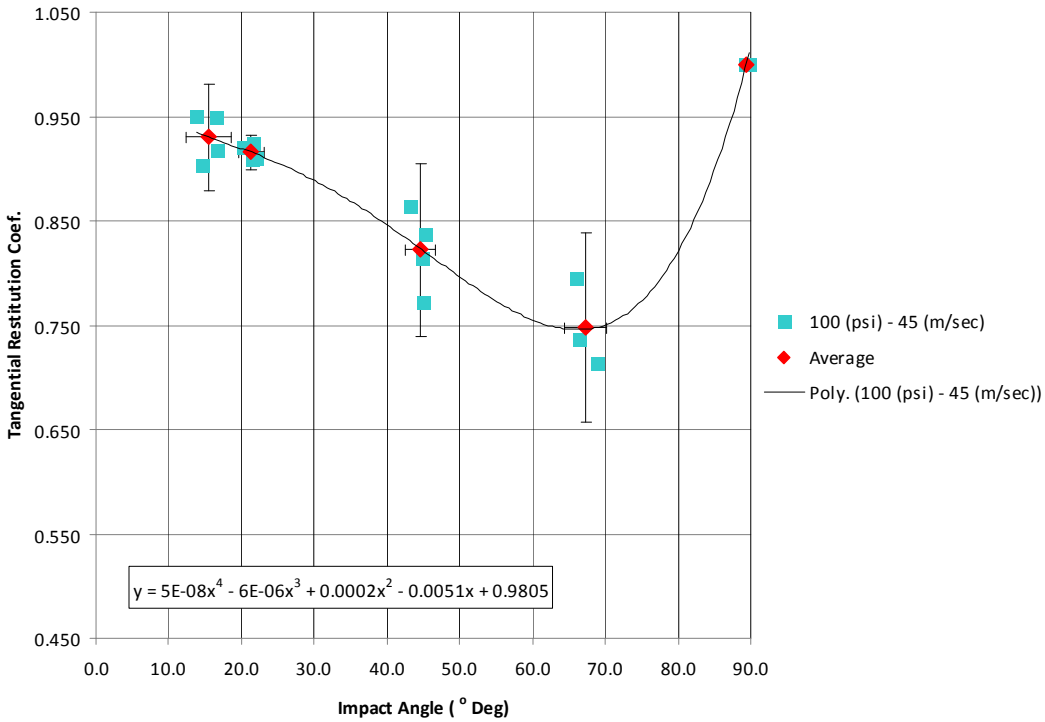

Figure 7-12 Capstone Design-Tangential Restitution Coefficient (100 psi)

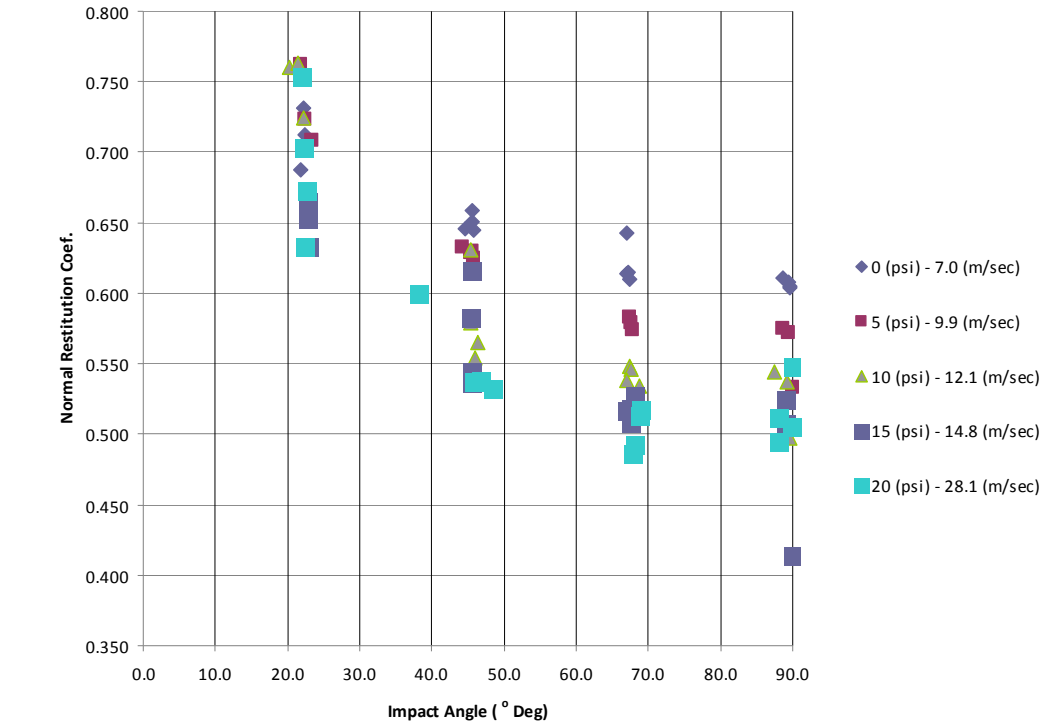

Figure 7-13 Viscous Driven Setup-Normal Restitution Coefficient (Exp. Data)

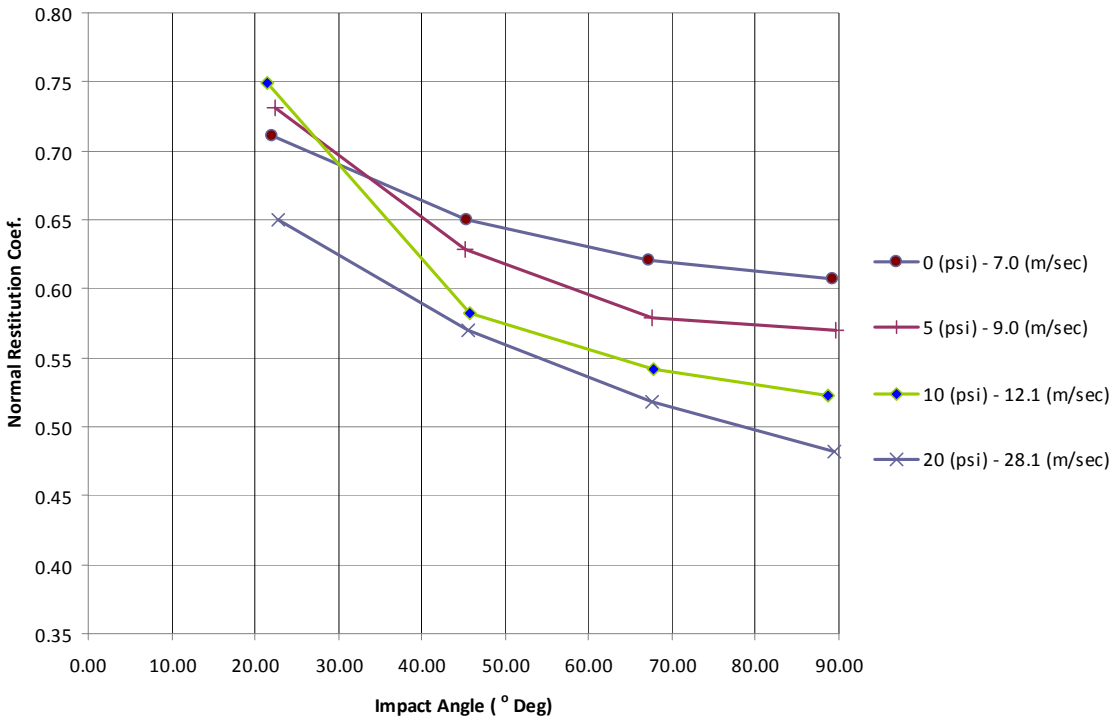

Figure 7-14 Viscous Driven Setup-Normal Restitution Coefficient-Velocity Comparison

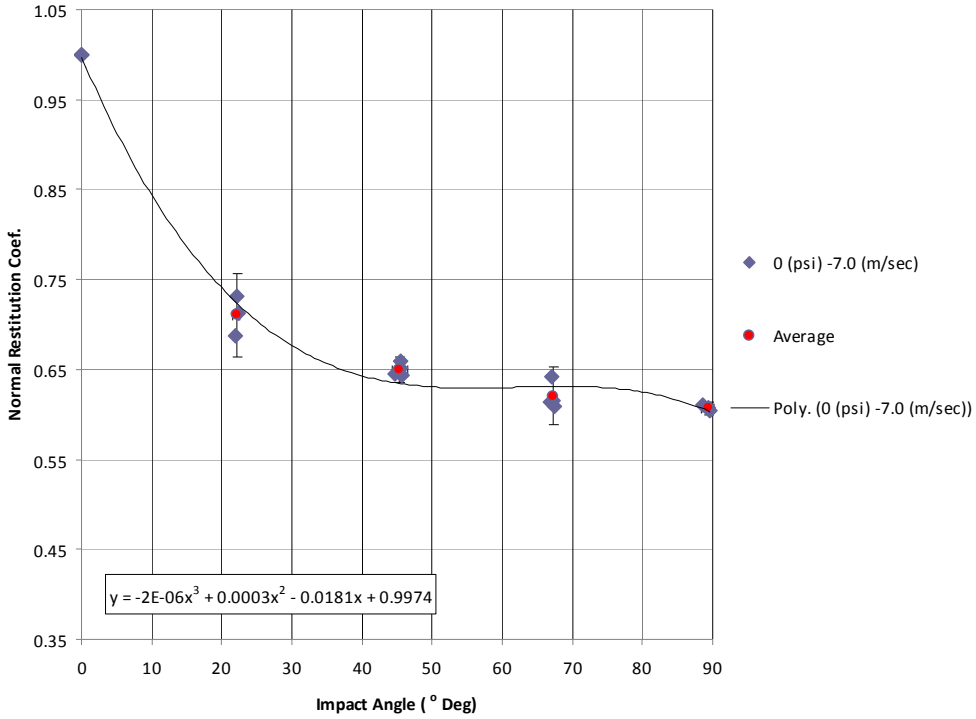

Figure 7-15 Viscous Driven Setup-Normal Restitution Coefficient (0 psi)

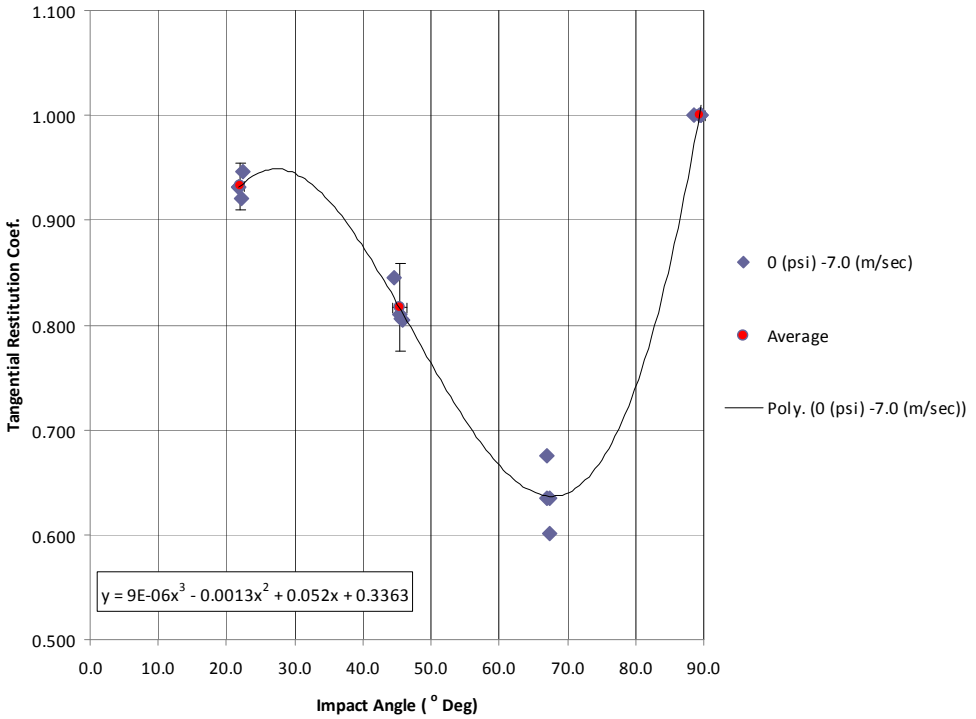

Figure 7-16 Viscous Driven Setup-Tangential Restitution Coefficient (0 psi)

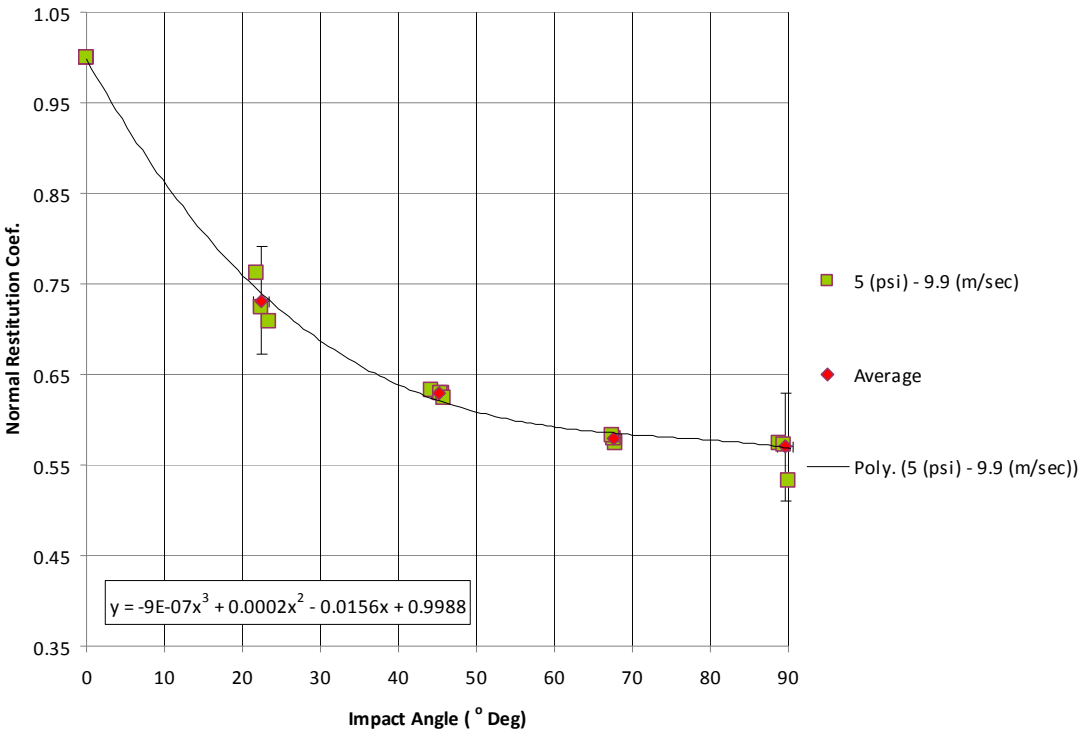

Figure 7-17 Viscous Driven Setup-Normal Restitution Coefficient (5 psi)

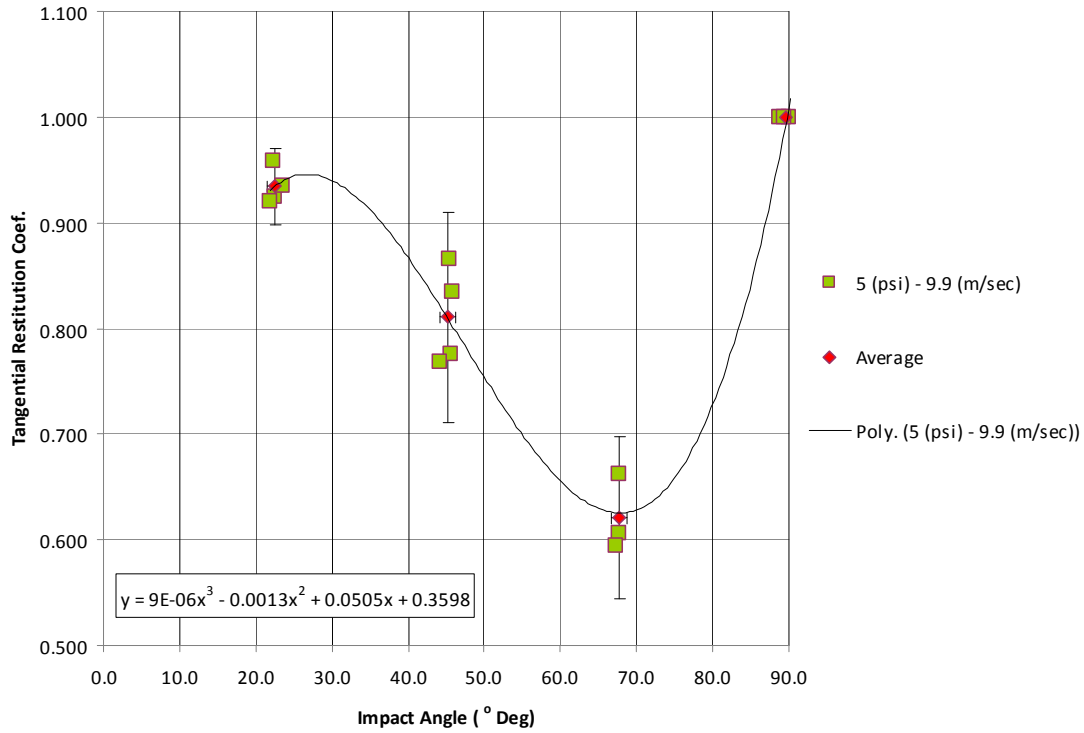

Figure 7-18 Viscous Driven Setup-Tangential Restitution Coefficient (5 psi)

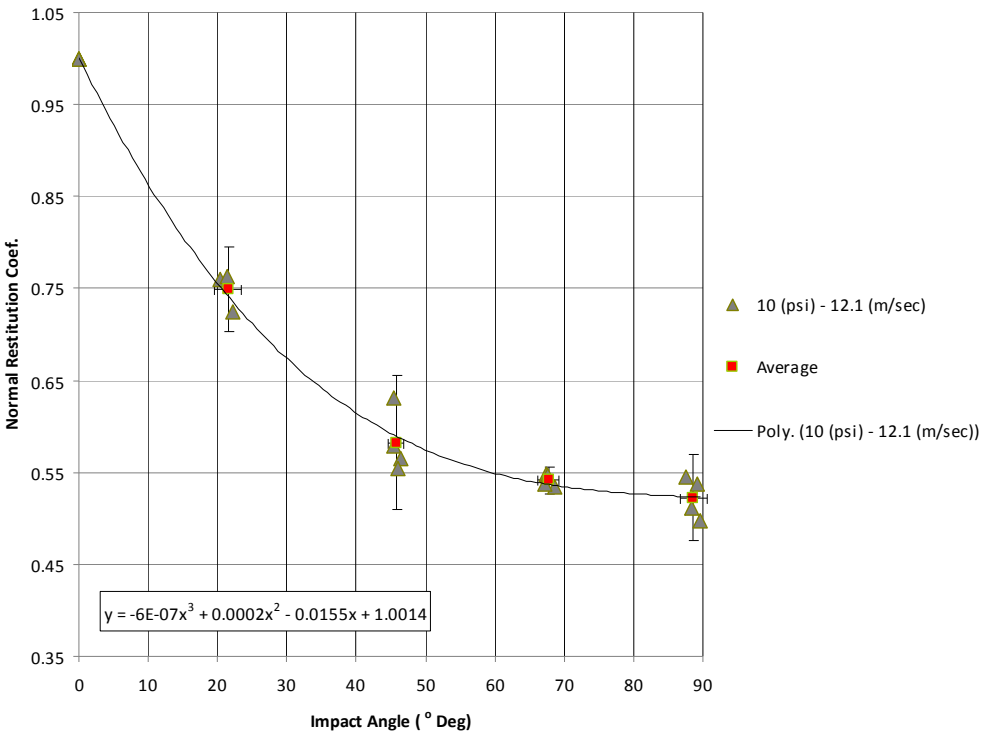

Figure 7-19 Viscous Driven Setup-Normal Restitution Coefficient (10 psi)

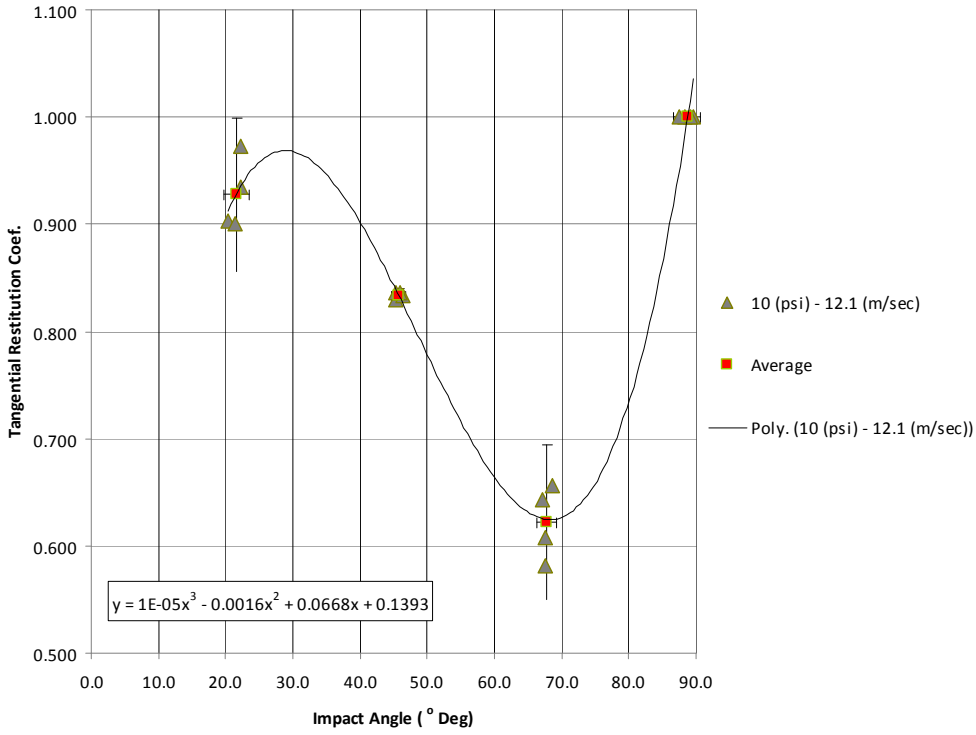

Figure 7-20 Viscous Driven Setup-Tangential Restitution Coefficient (10 psi)

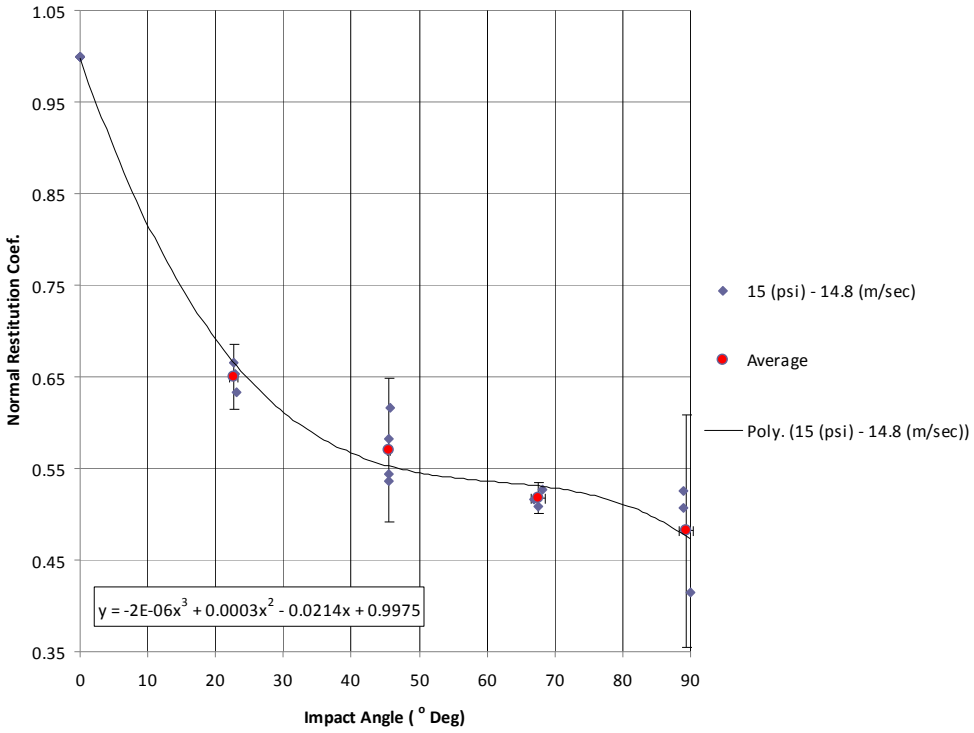

Figure 7-21 Viscous Driven Setup-Normal Restitution Coefficient (15 psi)

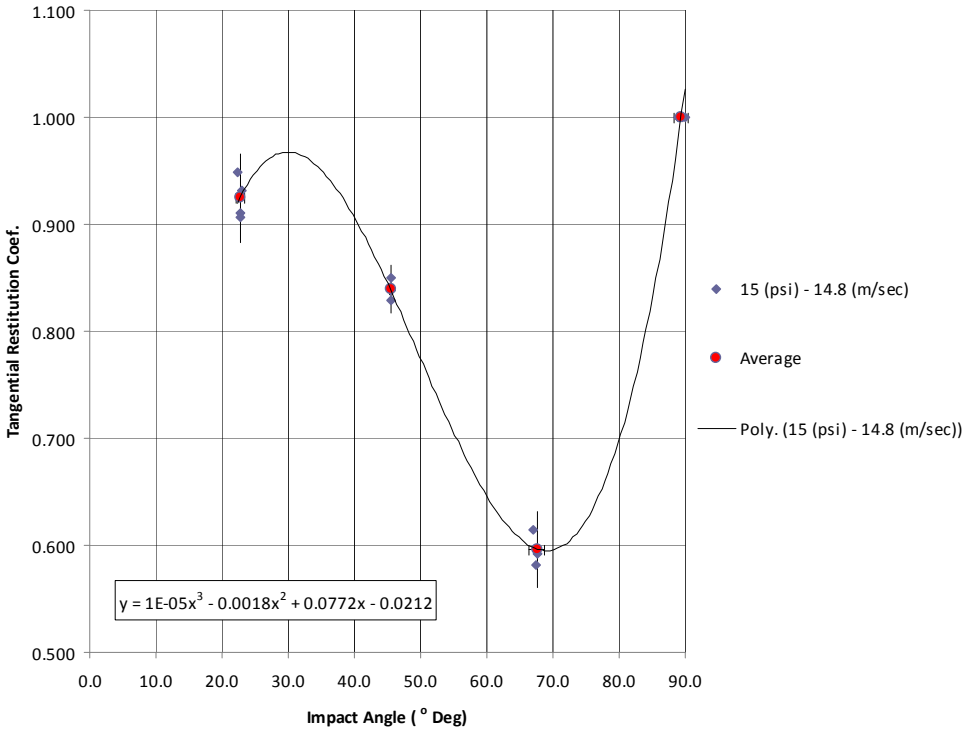

Figure 7-22 Viscous Driven Setup-Tangential Restitution Coefficient (15 psi)

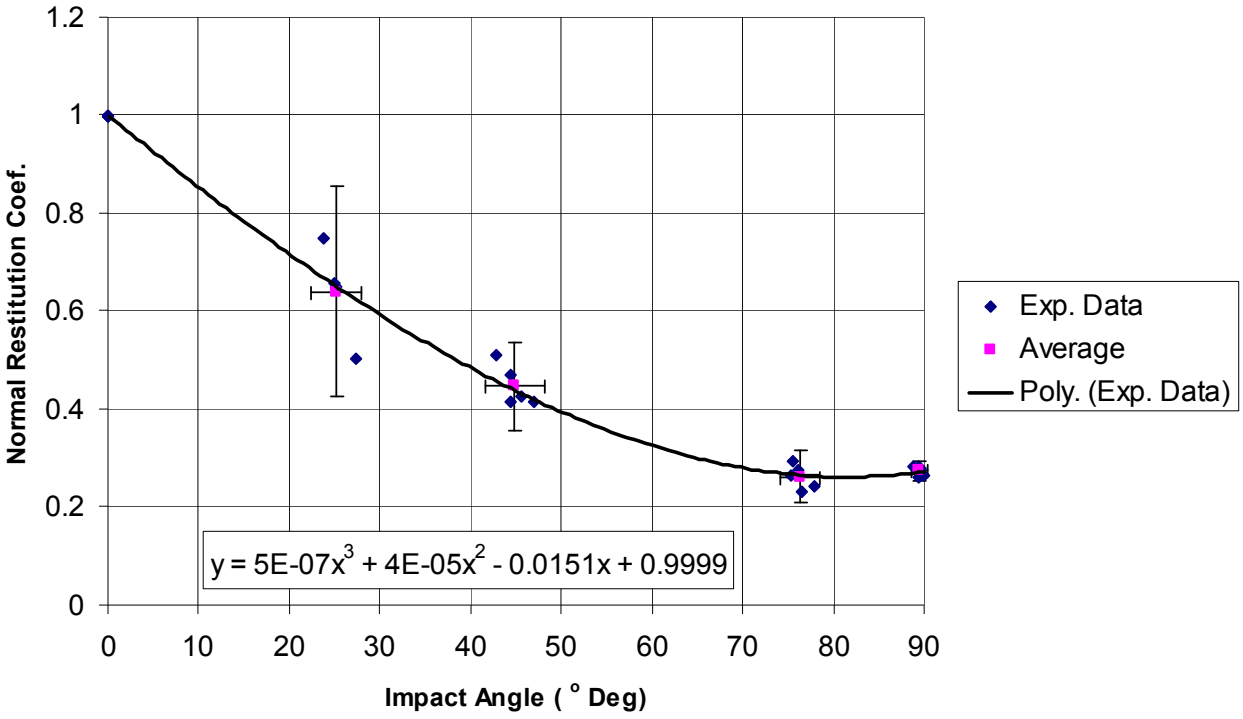

Figure 7-23 Indirect Compressed Air Shooting Setup-Normal Restitution Coefficient (Exp. Data)

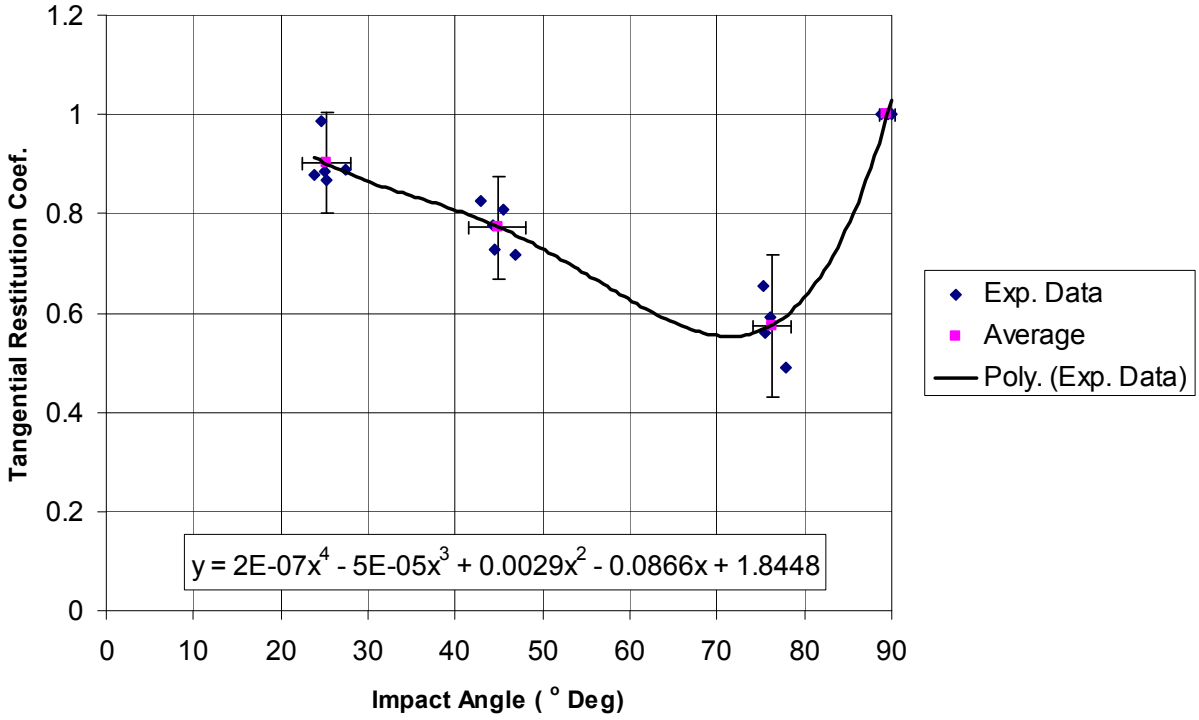

Figure 7-24 Indirect Compressed Air Shooting Setup-Tangential Restitution Coefficient (Exp. Data)

Object	Material	Density*	Poisson Ratio	Module of Elasticity	Yield Stress	Plastic Strain	Particle Size
Particle	Al_2O_3	3690	021	300	2100	---	
Wall	Glass	2200	0.25	70	1100	---	5mm

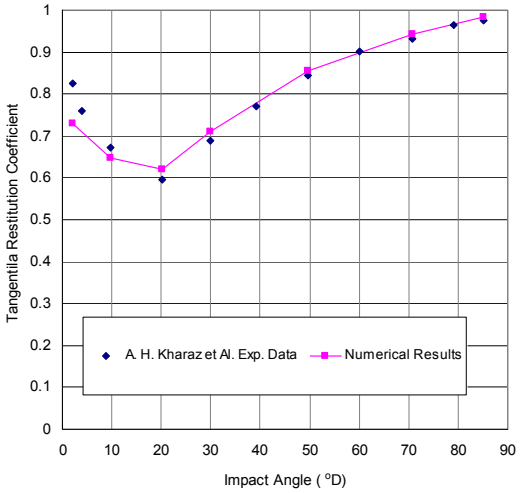

Figure 7-25 Data maching between numerical models and Kharaz et al. [33] Exp. Results (Impact Vel. 4m/sec and μ=0.09)

Object	Material	Density	Poisson Ratio	Module of Elasticity	Yield Stress	Plastic Strain	Particle Size
Particle	Steel 30	7850	0.3	201	141	.1064	
Wall	Hardened Steel	7850	0.3	205	440	0.0478	1.6mm

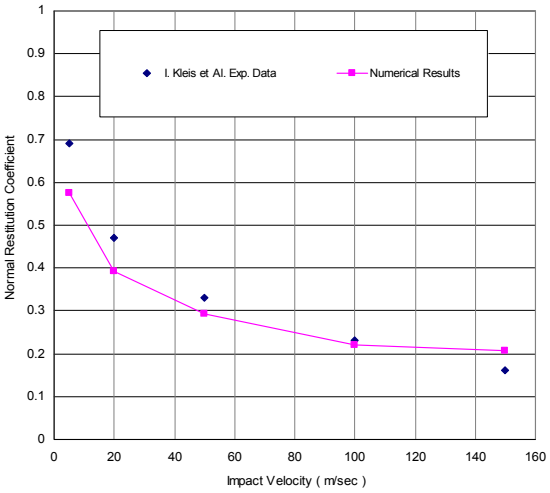

Figure 7-26 Data maching between numerical models and I.Kleis et al. [69] Exp. Results (μ=0.09)

* Densit (kg/m^3),Module of Elasticity (GPa), Yield Stress (MPa)

Object	Material	Density	Poisson Ratio	Module of Elasticity	Yield Stress	Plastic Strain	Particle Size
Particle	Glass	2200	0.17	72	1100	---	
Wall	Steel 45	7850	0.3	205	530	.00227	0.7mm

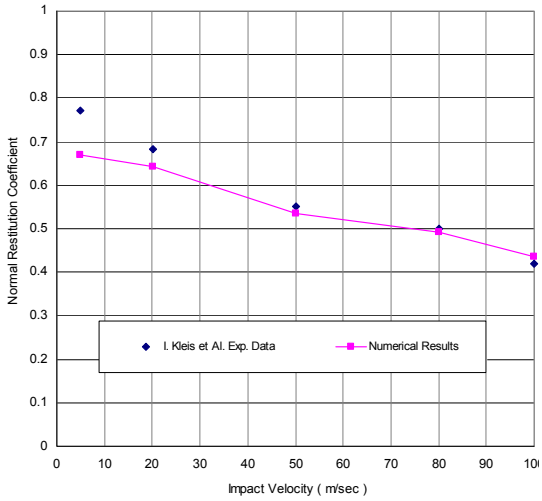

Figure 7-27 Data maching between numerical models and I.Kleis et al. [69] Exp. Results (μ=0.3)

Object	Material	Density	Poisson Ratio	Module of Elasticity	Yield Stress	Plastic Strain	Particle Size
Particle	Glass	2200	0.17	72	1100	---	
Wall	Steel	7810	0.3	210	205	.0723	500μm

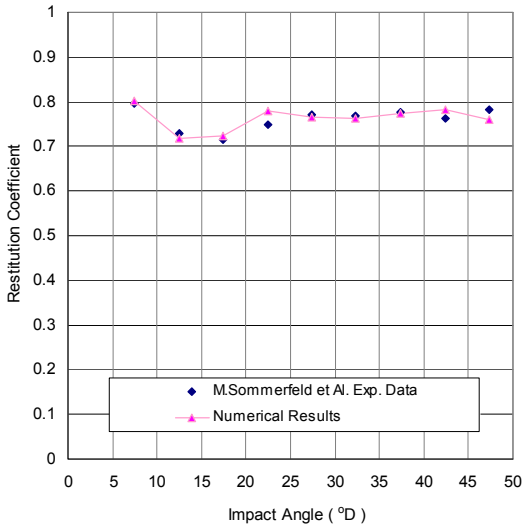

Figure 7-28 Data maching between numerical models and Sommerfeld et al. [31]Exp. Results (Impact Vel. 16m/sec)

Angle (°)	7	12	17	27	32	37	42	47
μ	0.8	0.7	0.5	0.3	0.25	0.2	0.15	0.1

Object	Material*	Density	Poisson Ratio	Module of Elasticity	Yield Stress	Plastic Strain	Particle Size
Particle	**Glass**	**2200**	**0.17**	**72**	**1100**	**---**	
Wall	**Steel**	**7810**	**0.3**	**210**	**205**	**.0723**	**100μm**

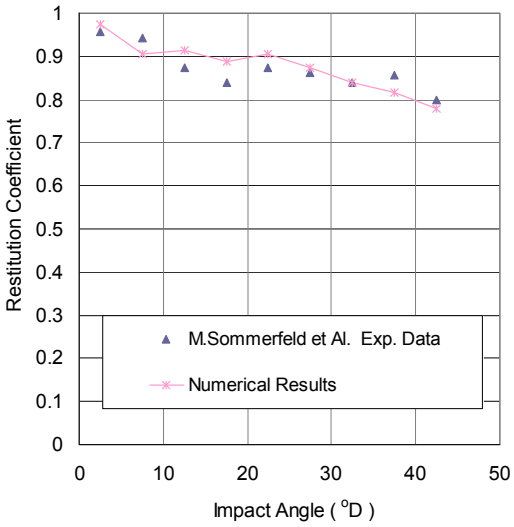

Figure 7-29 Data maching between numerical models and Sommerfeld et al. [31]Exp. Results (Impact Vel. 12m/sec)

Angle (°)	2	7	12	17	22	27	32	37	42
μ	0.375	0.375	0.2	0.18	0.1	0.1	0.1	0.09	0.09

Object	Material	Density	Poisson Ratio	Module of Elasticity	Yield Stress	Plastic Strain	Particle Size
Particle	**Steel**	**7850**	**0.3**	**210**	**1410**	**.106**	
Wall	**Steel**	**7850**	**0.3**	**205**	**345**	**.049**	**1.29mm**

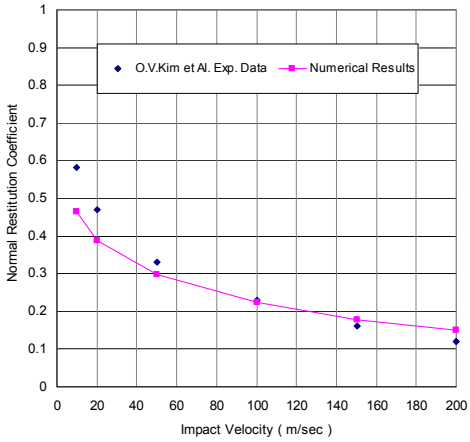

Figure 7-30 Data maching between numerical models and Kim et al. [44] Exp. Results (μ=0.3)

* Densit (kg/m^3),Module of Elasticity (GPa), Yield Stress (MPa)

Object	Material	Density*	Poisson Ratio	Module of Elasticity	Yield Stress	Plastic Strain	Particle Size
Particle	Al_2O_3	3690	021	300	2100	---	
Wall	Aluminum	2820	0.33	75	295	0.055	5mm

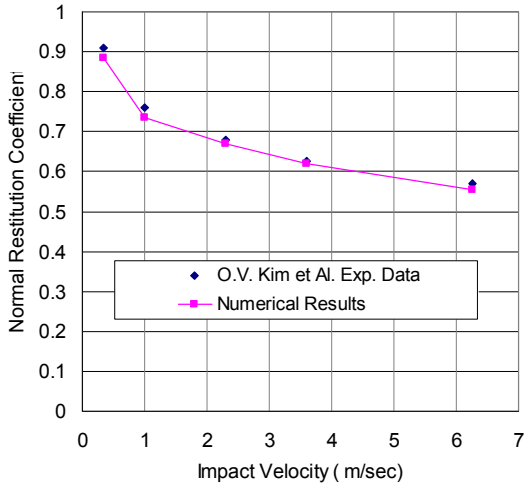

Figure 7-31 Data maching between numerical models and Kim et al. [44] Exp. Results (μ=0.09)

Object	Material	Density	Poisson Ratio	Module of Elasticity	Yield Stress	Plastic Strain	Particle Size
Particle	Steel	8000	0.3	193	310	.0787	
Wall	Aluminum	2700	0.33	68.9	185	0.0142	50μm

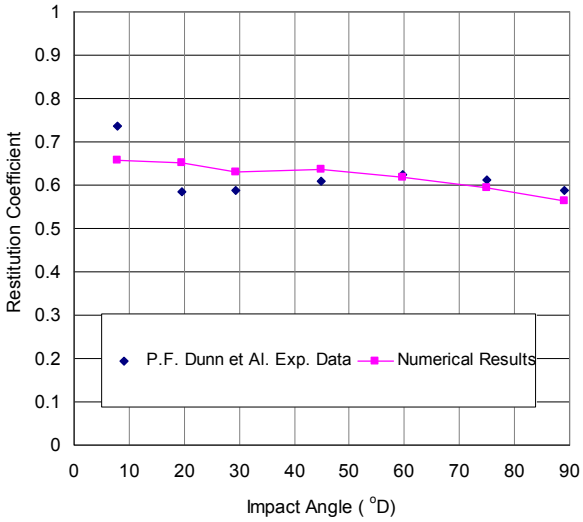

Figure 7-32 Data maching between numerical models and Dunn et al. [29]Exp. Results (Impact Vel. 1.7μ/sec)

Angle (°)	7	20	30	45	60	75	89
μ	1.5	1.5	0.5	.2	0.1	0.02	0.02

* Densit (kg/m^3),Module of Elasticity (GPa), Yield Stress (MPa)

Object	Material*	Density	Poisson Ratio	Module of Elasticity	Yield Stress	Plastic Strain	Particle Size
Particle	Glass	2200	17	72	1100	---	
Wall	Aluminum	2780	0.33	73	345	0.094	150μm

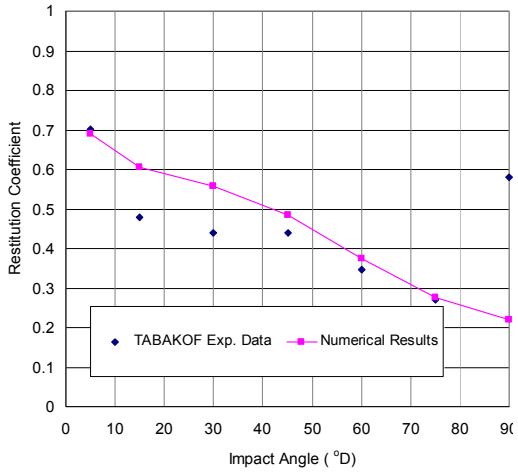

Figure 7-33 Data maching between numerical models and Tabakoff et al. [15]Exp. Results (Impact Vel. 91m/sec)

Angle (°)	5	15	30	45	60	75	90
μ	1.5	0.	0.6	0.5	0.2	0.09	0.09

Object	Material	Density	Poisson Ratio	Module of Elasticity	Yield Stress	Plastic Strain	Particle Size
Particle	Glass	2200	17	72	1100	---	
Wall	Aluminum	2780	0.33	73	345	0.094	15μm

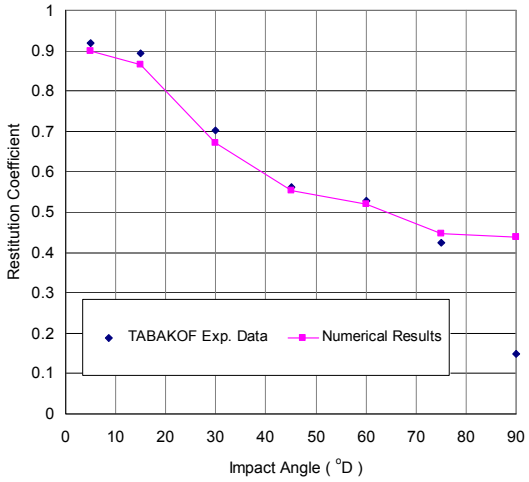

Figure 7-34 Data maching between numerical models and Tabakof et al[3]Exp. Results (Impact Vel. 98m/sec)

Angle (°)	5	15	30	45	60	75	90
μ	0.25	0.25	0.25	0.3	0.1	0.1	0.02

* Densit (kg/m^3),Module of Elasticity (GPa), Yield Stress (MPa)

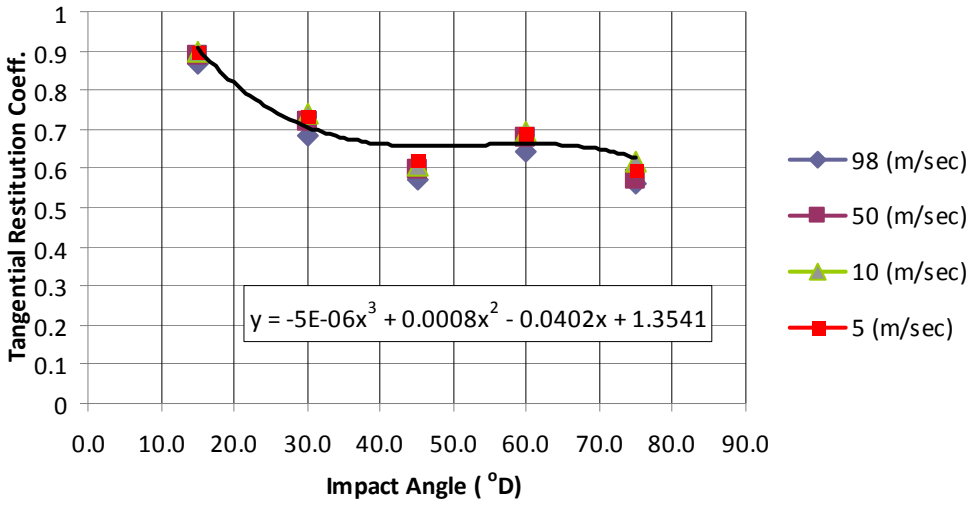

Figure 7-35 Tangential Restitution Coefficient (Numerical Results) – 015□m Sand Particle (Aluminum Target Plate)

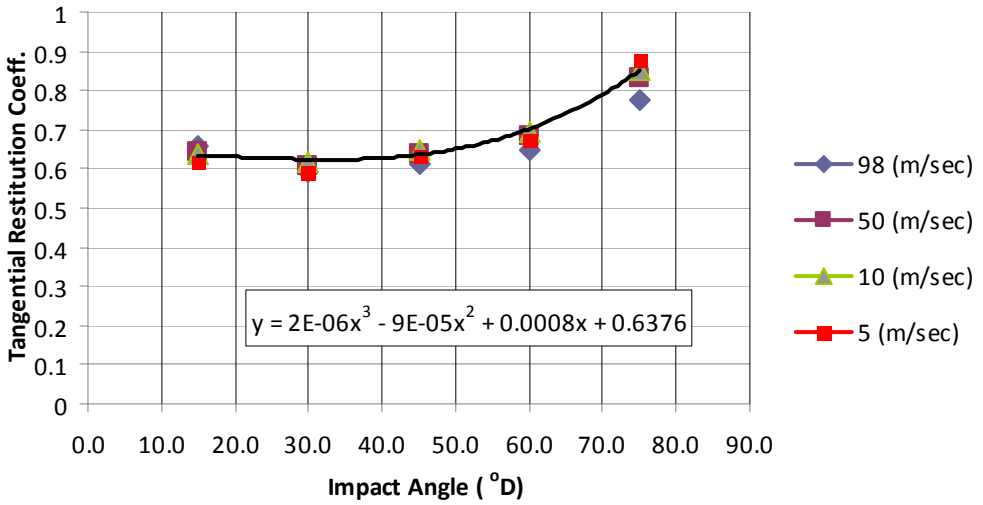

Figure 7-36 Tangential Restitution Coefficient (Numerical Results) – 050□m Sand Particle (Aluminum Target Plate)

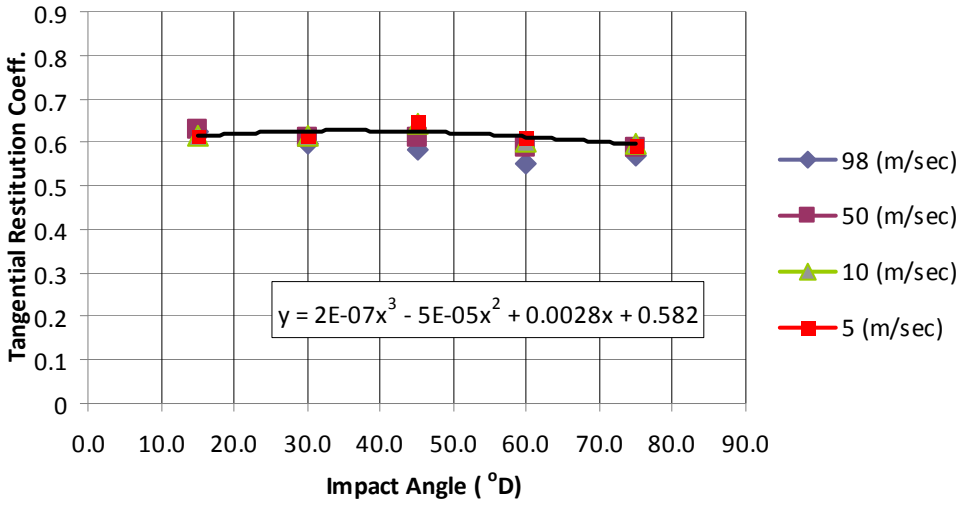

Figure 7-37 Tangential Restitution Coefficient (Numerical Results) – 150□m Sand Particle (Aluminum Target Plate)

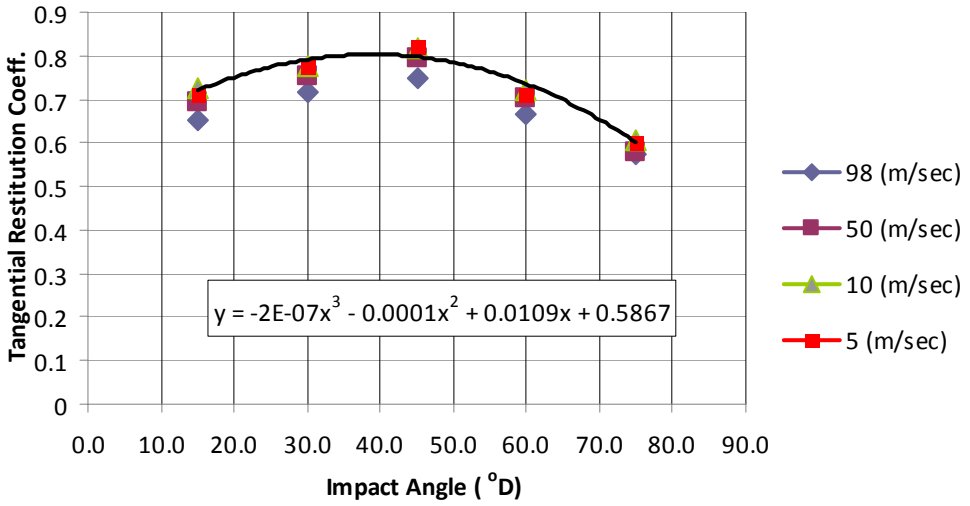

Figure 7-38 Tangential Restitution Coefficient (Numerical Results) – 500□m Sand Particle (Aluminum Target Plate)

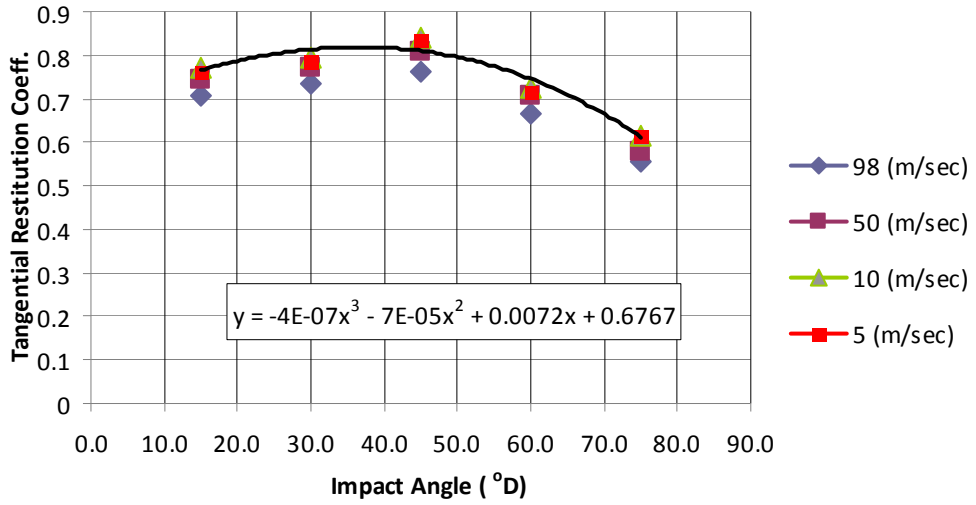

Figure 7-39 Tangential Restitution Coefficient (Numerical Results) – 700□m Sand Particle (Aluminum Target Plate)

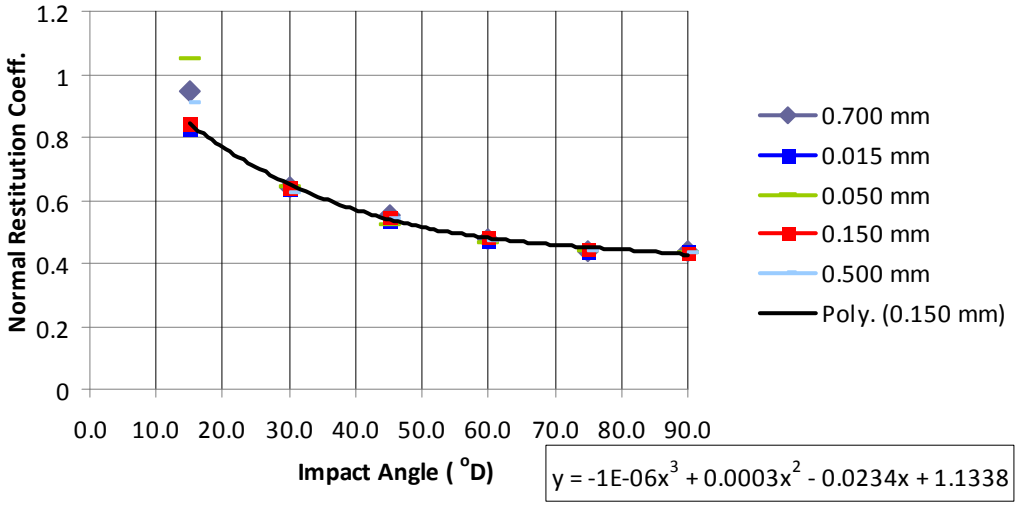

Figure 7-40 Normal Restitution Coefficient (Numerical Results) – 100m/sec Impact Vel. (Aluminum Target Plate)

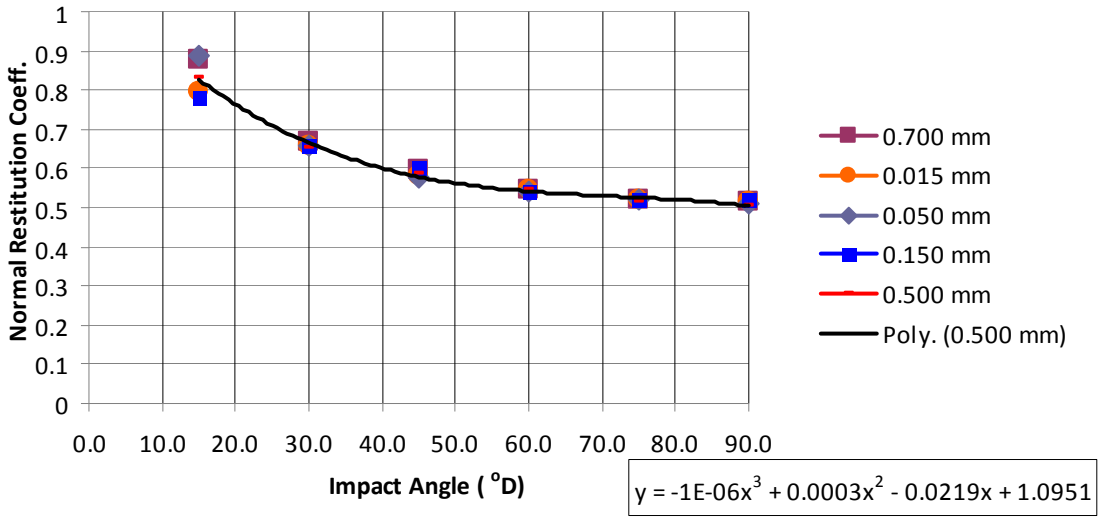

Figure 7-41 Normal Restitution Coefficient (Numerical Results) – 050m/sec Impact Vel. (Aluminum Target Plate)

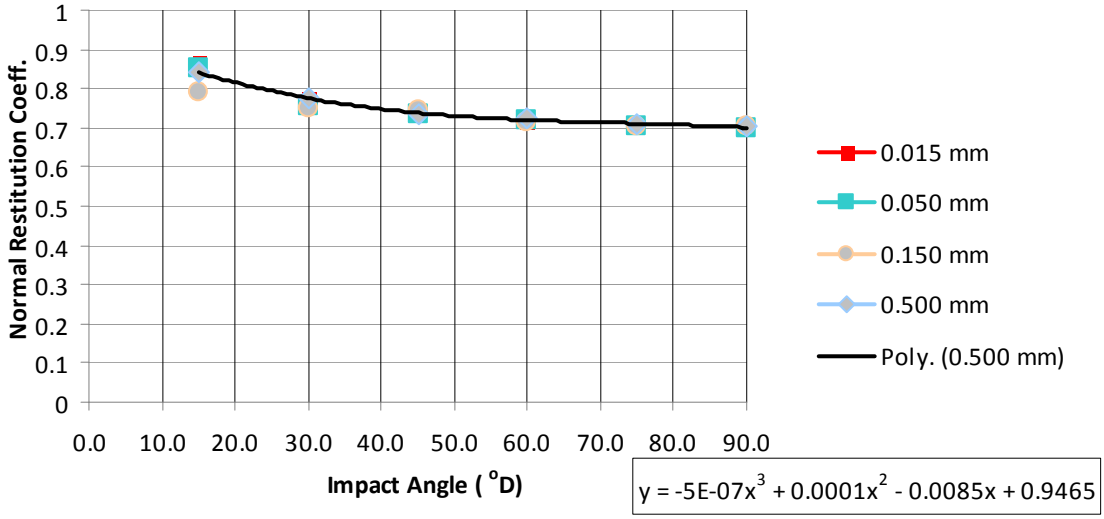

Figure 7-42 Normal Restitution Coefficient (Numerical Results) – 010m/sec Impact Vel. (Aluminum Target Plate)

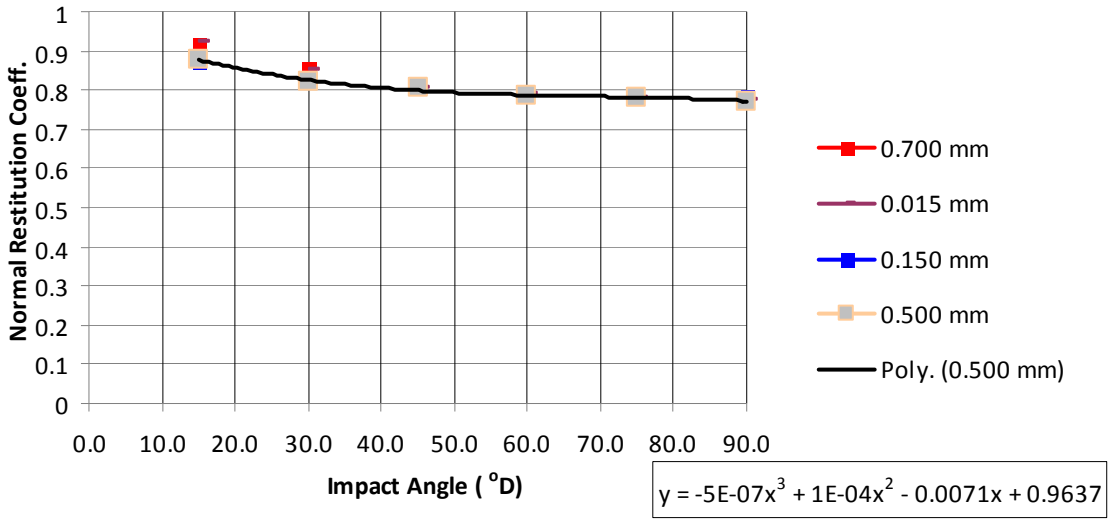

Figure 7-43 Normal Restitution Coefficient (Numerical Results) – 005m/sec Impact Vel. (Aluminum Target Plate)

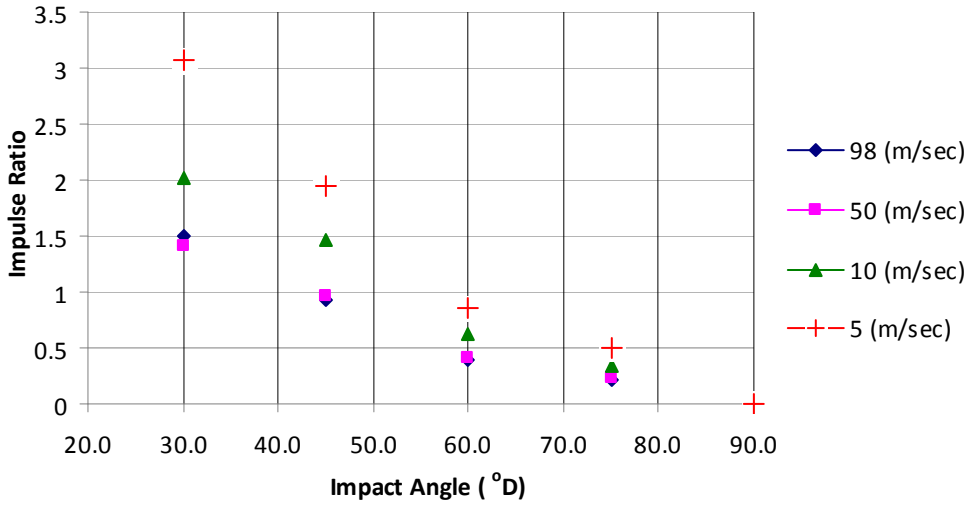

Figure 7-44 Impulse Ratio (Numerical Results) – 015□m Sand Particle (Aluminum Target Plate)

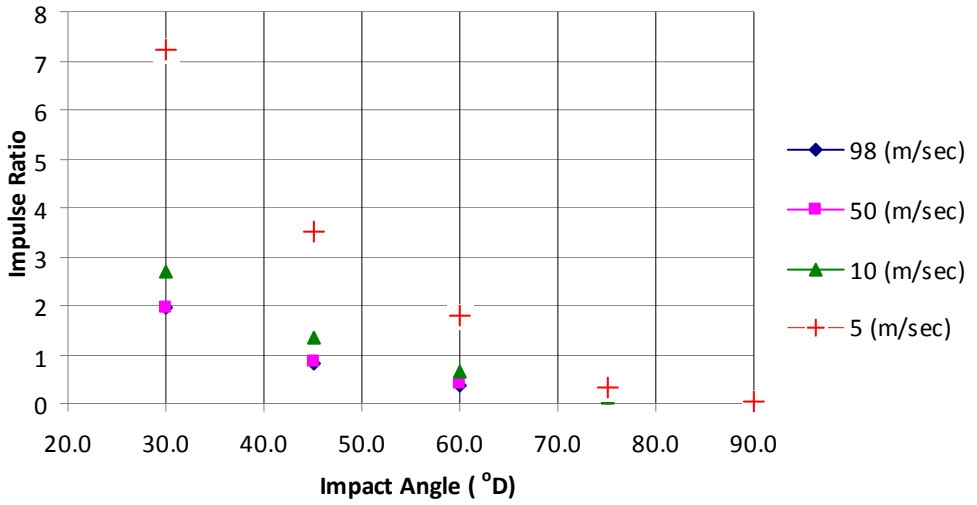

Figure 7-45 Impulse Ratio (Numerical Results) – 050□m Sand Particle (Aluminum Target Plate)

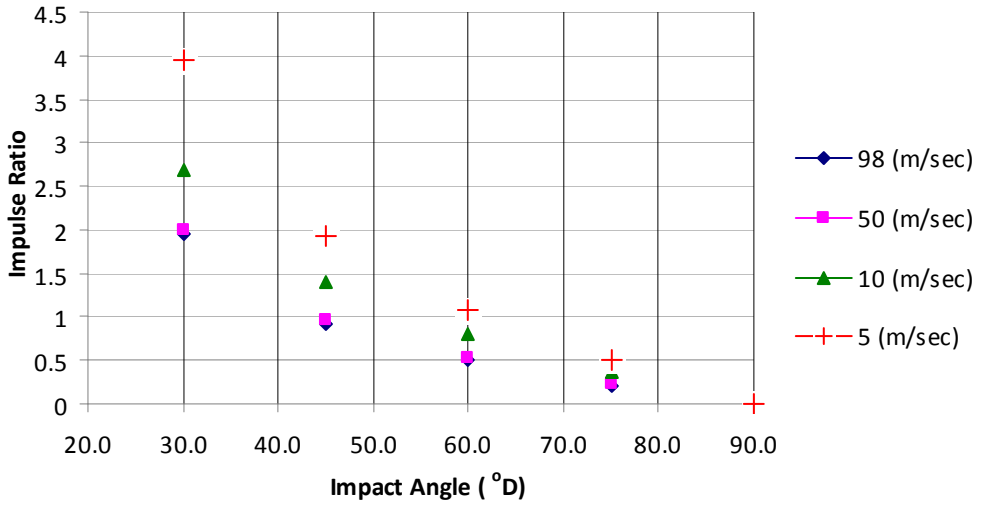

Figure 7-46 Impulse Ratio (Numerical Results) – 1655□m Sand Particle (Aluminum Target Plate)

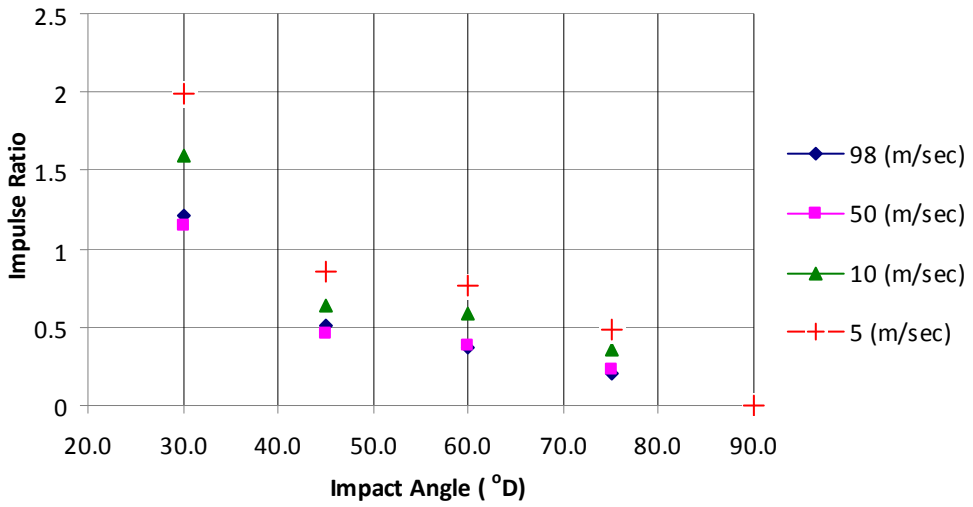

Figure 7-47 Impulse Ratio (Numerical Results) – 500□m Sand Particle (Aluminum Target Plate)

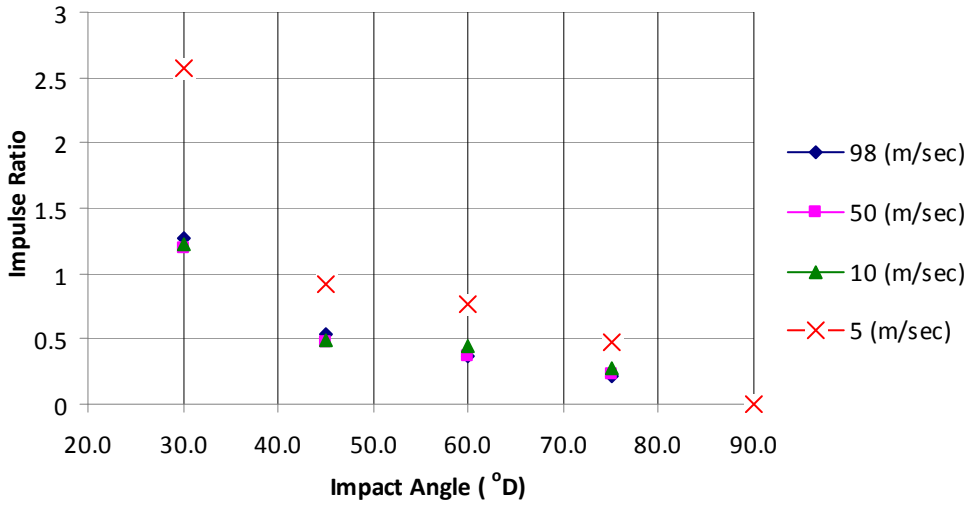

Figure 7-48 Impulse Ratio (Numerical Results) – 700□m Sand Particle (Aluminum Target Plate)

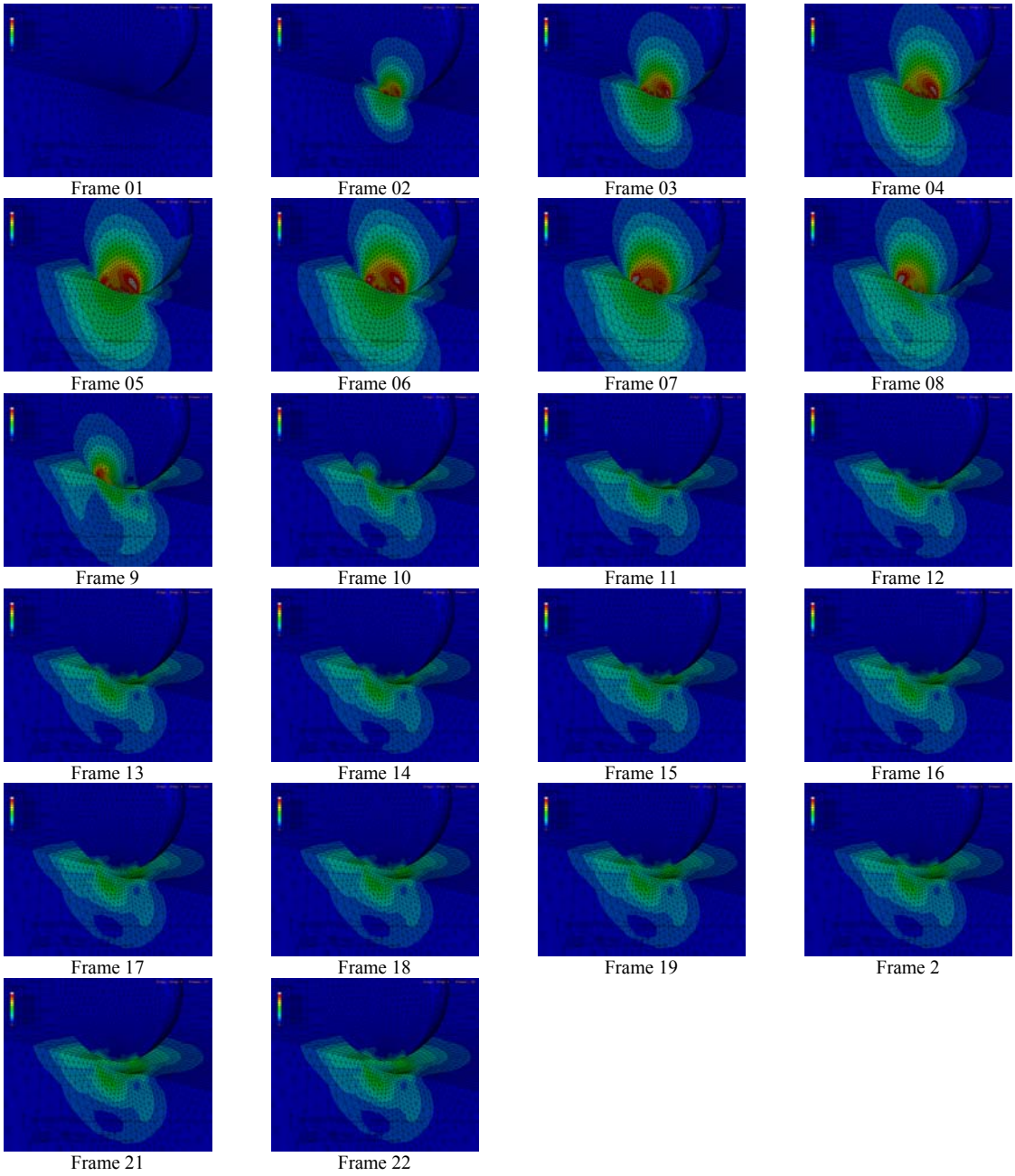

Figure 7-49 Sample Stress Distribution and Deformation Histories of Wall-Particle Impact

REFERENCES

1. Warren, J., et al., *Best Practices for the Mitigation and Control of Foreign Object Damage-Induced High Cycle Fatigue in Gas Turbine Engine Compression System Airfoils*, in *RTO TECHNICAL REPORT*, R.A.V.T.P.A.T. Group-094, Editor. 2005.
2. Tabakoff, W. and A. Hamed, *Hostile Atmospheric Environment Effects on Jet Engines.* INTERNATIONAL JOURNAL OF TURBO AND JET ENGINES, 1988. **5**: p. 1-11.
3. Hamed, A., W. Tabakoff, and R. Wenglarz, *Erosion and Deposition in Turbomachinery.* JOURNAL OF PROPULSION AND POWER, 2006. **22**(2): p. 350-360.
4. Zoccoli, M.J., *Advanced Scavenge Systems for an Integrated Engine Inlet Particle Separator*, in *USAAMRDL-TR-77-26*. 1977, Avco Lycoming Division: Stratford, Connecticut.
5. Grant, G., R. Ball, and W. Tabakoff, *An Experimental Study of the Erosion Rebound Characteristics of Hight Speed Particles Impacting a Stationary Specimen*, in *Report No. 73-36*. 1973, University of Cincinnati.
6. Ball, R. and W. Tabakoff, *An Experimental Investigation of the Particle Dynamics of Quartz Sand Impacting 6A1-4V Titanium and 410 Stainless Steel in an Erosive Environment*, in *Report No. 74-73*. 1974, University of Cincinnati.
7. Grant, G. and W. Tabakoff, *Erosion Prediction in Turbomachinery Due to Environmental Solid Particles*, in *AIAA 12th AEROSPACE SCIENCE MEETING*. 1974: Washington, D.C.
8. Tabakoff, W. and A. Hamed, *Aerodynamic Effects on Erosion in Turbomachinery*, in *Joint Gas Turbine Congress*. 1977: Tokyo, Japan. p. 574-581.
9. Kotwal, R. and W. Tabakoff, *A New approach for Erosion Prediction Due to Fly Ash*, in *ASME Gas Turbine Conference*. 1980.
10. Wakeman, T. and W. Tabakoff, *Measured Particle Robound Characteristics Useful for Erosion Prediction*, in *ASME Gas Turbine Conference*. 1982.

11. Tabakoff, W. and M.F. Malak, *Laser Measurements of Fly Ash Rebound Parameters for Use in Trajectory Calculations.* JOURNAL OF TURBOMACHINERY, 1987. **109**: p. 535-540.
12. Tabakoff, W., *Meaurement of Particles Rebound Characteristics on Materials Used in Gas Turbines.* JOURNAL OF PROPULSION, 1991. **7**(5): p. 805-813.
13. Tabakoff, W., et al., *Study of Particle Rebound Characteristics and Material Erosion at High Teprature*, in *ORNL/Sub84-89628/04*. 1992, University of Cincinnati.
14. Hamed, A. and W. Tabakoff, *Experimental and Numerical Simulations of the Effects f Ingested Particles in Gas Turbine Engines*, in *PROPULSION AND ENERGETICS PANEL (PEP) SYMPOSIUM*. 1994: Rotterdam, Netherlands. p. 11 (1-13).
15. Tabakoff, W., A. Hamed, and D.M. Murugan, *Effect of Target Materials on the Particle Restitution Characteristics for Turbomachinery Application.* JOURNAL OF PROPULSION AND POWER, 1996. **12**(2): p. 260-266.
16. Duffy, R.J. and B.F. Shattuck, *Integral Engine Inlet Particle Separator, Volume I - Technology Program*, in *USAAMRDL-TR-75-31A*, I, Editor. 1975, General Electric Company, Aircraft Engine Group: Cincinnati, Ohio.
17. Duffy, R.J. and B.F. Shattuck, *Integral Engine Inlet Particle Separator, Volume II-Desing Guid*, in *USAAMRDL-TR-75-31B*. 1975, General Electric Company, Aircraft Engine Group: Cincinnati, Ohio.
18. Hamed, A., *Particle Dynamics of Inlet Flow Fields with Swirling Vanes*, in *AIAA 19th AEROSPACE SCENCES MEETINGS*. 1981.
19. Tabakoff, W. and A. Hamed, *Installed Enginie Performance In Dust-Laden Atmosphere*, in *AIAA/AHSASEE Aircraft Design Systems and Operations Meetings*. 1984: San Diego, California.
20. Vittal, B.R., *A Design System for Erosion Tolerant Helicopter Engines.* Journal of the American Helicopter Society, 1988. **33**(1): p. 47-54.
21. Saeed, F. and A.Z. Al-Garni, *Analysis Method for Inertial Particle Separator.* JOURNAL OF AIRCRAFT, 2007. **44**(4): p. 1150-1158.
22. Taslim, M.E., et al. *A Numerical Study of Sand Separation Applicable to Engine Inlet Particle Separator Systems*. in *ANNUAL FORUM PROCEEDINGS- AMERICAN HELICOPTER SOCIETY*. 2004.

23. Taslim, M.E. and S.D. Spring, *A Numerical Study of Sand Separation Applicable to Engine Inlet Particle Separator Systems.* AMERICAN HELICOPTER SOCICETY, 2009.
24. Legendre, D., et al., *A note on the modelling of the bouncing of spherical drops or solid spheres on a wall in viscous fluid.* CHEMICAL ENGINEERING SCIENCE, 2006. **61**: p. 3543-3549.
25. Tabor, D., *The Hardness of Metals*. 1st ed. 1951: Clarendon Press, Oxford.
26. Matumoto, S. and S. Saito, *Monte Carlo Simulation of Horizontal Pneumatic Conveying Based on the Rough Wall Model.* CHEMICAL ENGINEERING OF JAPAN, 1970. **3**(2): p. 223-230.
27. Matumoto, S. and S. Saito, *On the Mechanism of Suspenson of Particles in Horizontal Pneumatic Conveying: Mont Carlo Simulation Based on the Irregular Bouncing Model.* CHEMICAL ENGINEERING OF JAPAN, 1970. **3**(1): p. 83-92.
28. Brach, R.M. and P.F. Dunn, *Macrodynamics of Microparticles.* AEROSOL SCIENCE AND TECHNOLOGY, 1995. **23**: p. 51-71.
29. Dunn, P.F., R.M. Brach, and M.J. Caylor, *Experiment on the Low-Velocity Impact of Microspheres with Planar Surfaces.* AEROSOL SCIENCE AND TECHNOLOGY, 1995. **23**: p. 80-95.
30. Dunn, P.F., R.M. Brach, and G.G. Janson, *Surface-Contact Mechanics During Oblique Impact of Microspheres with Planar Surfaces.* AEROSOL SCIENCE AND TECHNOLOGY, 1996. **25**(4): p. 445-465.
31. Sommerfeld, M., *Modelling of Particle-Wall Collisions in Confined Gas-Particle Flows.* INTERNATIONAL JOURNAL OF MULTIPHASE FLOW, 1992. **18**(6): p. 905-926.
32. Sommerfeld, M. and N. Huber, *Experimental Analysis and Modelling of Particle-wall Collision.* INTERNATIONAL JOURNAL OF MULTIPHASE FLOW, 1999. **25**: p. 1457-1489.
33. Kharaz, A.H., D.A. Gorham, and A.D. Salman, *Accurate Measurement of Particle Impact Parameters.* MEASURMENT SCIENCE and TECHNOLOGY, 1999. **10**: p. 31-35.
34. Kharaz, A.H., D.A. Gorham, and A.D. Salman, *An Experimental Study of the Elastic Rebound of Sphere.* POWDER TECHNOLOGY, 2001. **120**: p. 281-291.

35. Hutchings, I.M., R.E. Winter, and J.E. Field. *Solid particle erosion of metals - removal of surface material by spherical projectiles*. in *Royal Society of London Series A, Mathematical Physical and Engineering Sciences*. 1976.
36. Hutchings, I.M. *Some Comments on the Thoretical Treatment of Erosive Particle Impact*. in *5th INTERNATIONAL CONFERENCE ON EROSION BY SOLID AND LIQUID IMPACT*. 1979. Newnham College, Cambridge, England.
37. Rickerby, D.G. and N.H. Macmillan, *On the oblique impact of a rigid sphere against a rigid-plastic solid.* International Journal of Mechanical Sciences, 1980. **22**(8): p. 491-494.
38. Hutchings, I.M., H.H. Macmillan, and D.G. Rickerby, *Further Studies of the Oblique Impact of a Hard Sphere Against a Ductile Solid.* International Journal of Mechanical Sciences, 1981. **23**(11): p. 639-646.
39. Sriram, T.S. and T.H. Kosel. *Computer Modeling of the Rebound Characteristics of Spherical Erodent Particle*. in *7th INTERNATIONAL CONFERENCE ON EROSION B LIQUID AND SOLID IMPACT*. 1987. Robnson College, Cambridge, UK.
40. Timothy, S.P. and I.M. Hutchings, *The Impact of a Soft Metal Sphere on a Hard Metal Target I. Deformation of the Sphere.* PHILOSOPHICAL MAGAZINE A, 1986. **54**(1): p. 93-102.
41. Timothy, S.P. and I.M. Hutchings, *The Impact of a Soft Metal Sphere on a Hard metal Target II. Deformation of the Target.* PHILOSOPHICAL MAGAZINE A, 1986. **54**(1): p. 103-113.
42. Tsai, C.J., D.Y.H. Pui, and B.Y.H. Liu, *Capture and Rebound of Small Particles Upon Impact with Solid Surfaces.* AEROSOL SCIENCE AND TECHNOLOGY, 1990. **12**: p. 497-507.
43. Li, X., P.F. Dunn, and R.M. Brach, *Experimental and Numerical Studies of Microsphere Oblique Impact with Planar Surfaces.* AEROSOL SCIENCE, 2000. **31**(5): p. 583-594.
44. Kim, O.V. and P.F. Dunn, *A microsphere-Surface Impact Model for Implementation in Computational Fluid Dynamics.* AEROSOL SCIENCE, 2007. **38**: p. 532-549.
45. Al-Hassani, S.T.S., K. Kormi, and D.C. Webb, *Numercial Simulation of Multiple Shot Impact*, in *7th International Conference on Shot Peening*. 1999: Warsaw, POLAND. p. 217-227.

46. WU, C.Y., C. Thornton, and L.Y.Li, *Coefficient of Restitutioin for Elastoplastic Oblique Impacts.* ADVANCED POWDER TECHNOLOGY, 2003. **14**(4): p. 435-448.
47. Partridge, W.S., H.B. Vanfleet, and C.R. Whited, *Crater Formation in Metallic Targets.* Journal of Applied Physics, 1958. **29**(9): p. 1332-1336.
48. Hussein, M.F. and W. Tabakoff, *Dynamic Behavior of Solid Particles Suspended by Polluted Flow in a Turbine Stage.* JOURNAL OF AIRCRAFT, 1973. **10**(7): p. 434-440.
49. Foerster, S.F., et al., *Measurments of the collision Properties of small spheres.* PHYSICS OF FLUIDS, 1994. **6**(3): p. 1108-1115.
50. Lorenz, A., C. Tuozzolo, and M.Y. Louge, *Measurements of Impact Properties of Small, Nearly Spherical Particles.* EXPERIMENTAL MECHANICS, 1997. **37**(3): p. 292-298.
51. Nobre, J.P., A.M. Dias, and R. Gras, *A study on elasto-plastic impact friction.* WEAR, 1999. **230**: p. 133-145.
52. JOSEPH, G.G., et al., *Particle-wall Collisions in a Viscous Fluid.* JOURNAL OF FLUID MECHANICS, 2001. **433**: p. 329-346.
53. Gondret, P., M. Lance, and L. Petit, *Bouncing motion of spherical particles in fluids.* PHYSICS OF FLUIDS, 2002. **14**(2): p. 643-652.
54. Oka, Y.I., et al., *Control and Evaluation of Particle Impact Conditions in a Sand Erosion Test Facility.* WEAR, 2001. **250**(1-12): p. 736-743.
55. Leconte, M., et al., *Inelastic ball-plane impact: An accurate way to measure the normal restitution coefficient.* APPLIED PHYSICS LETTERS, 2006. **89**(243518): p. 1-3.
56. Dahneke, B., *The capture of aerosol particles by surfaces.* Journal of Colloid and Interface Science, 1971. **37**(2): p. 342-353.
57. Dahneke, B., *Measurements of bouncing of small latex spheres.* Journal of Colloid and Interface Science, 1973. **45**(3): p. 584-590.
58. Dahneke, B., *Further measurements of the bouncing of small latex spheres.* Journal of Colloid and Interface Science, 1975. **51**(1): p. 58-65.
59. *SILICA, PHYSICAL BEHAVIOR, GEOCHEMISTY AND MATERIALS APPLICATIONS.* Reviews in Mineralogy, ed. P.J. Heaney, C.T. Prewitt, and G.V. Gibbs. Vol. 29. 1994.
60. Eastes, J.W., *Spectral and Physical Properties of Some Desert Soils: Implications for Remote Spectroscopic Terrain Analysis in Arid Regions.* APPLIED SPECTROSCOPY, 1992. **46**(4): p. 640-644.

61. Abolkhair, Y.M., *The Size Charcteristics of the Drifting Sand Grains in al-Hasa Oasis, Saudi Arabia.* GEOJOURNAL, 1985. **11**(2): p. 131-135.
62. Alshrhan, A.S. and A.A. El-Sammak, *Grain-Size Analysis and Charcterization of Sedimentary Environments of the United Arab Emirates Coastal Area.* COASTAL RESEARCH, 2004. **20**(2): p. 464-477.
63. Abdulla, S.A.A., h.m. Al-Rizzo, and M.M. Cyril, *Particle-Size Distribution of Iraqi Sand and Dust Storms and Their Influence on Microwave Communication Systems.* IEEE TRANSACTIONS ON ANTENNAS AND PROPAGATION, 1988. **36**(1).
64. Hertz, H., *Über die Berührung fester elastischer Körper.* JOURNAL OF REINE ANGEW. MATH. (CRELLE), 1881. **92**(155).
65. Hutchings, I.M. and R.E. Winter, *A simple small-bore laboratory gas-gun.* Journal of Physics E: Scientific Instruments, 1975(2): p. 84.
66. B.V. Derjaguin, V.M.M., N.S. Mikhovich and Yu.P. Toporov, *Influence of contact electrification on the collision of elastic particles with a rigid surface* Journal of Colloid and Interface Science, 1987. **118**(2): p. 553-563

67. Kolsky, J.M.L.a.H., *Some experiments on anelastic rebound* Journal of the Mechanics and Physics of Solids, 1964. **12**(1): p. 35-43.
68. Tabakoff, W. and C. Balan, *A Study of the Surface Deterioration due to Erosion*, in *ASME Gas Turbine Conference*. 1983.
69. Kleis, I. and I. Hussainova, *Investigation of Particle-Wall Impact Process.* WEAR, 1999. **233-235**: p. 168-173.